Scanning Probe Microscopy of Poly-atomic Molecules

by

Tianluo Pan

A thesis submitted to

The University of Birmingham

for the degree of

DOCTOR OF PHILOSOPHY

Nanoscale Physics Research Laboratory

School of Physics & Astronomy

The University of Birmingham

October 31, 2012

Abstract

This thesis presents studies on the adsorption of chlorobenzene using scanning tunnelling spectroscopy (STS), non-local desorption of chlorobenzene together with the atomic manipulation of the 4,4'-dichlorobiphenyl (PCB) molecule on the Si(111)-(7×7) surface using scanning tunneling microscopy (STM). The atomic manipulation of the bio-molecule pig gastric mucin (PGM) on different highly ordered pyrolytic graphite (HOPG) surfaces under different conditions has also been investigated.

The bonding geometry of the chlorobenzene adsorbate on the Si(111)-(7×7) surface has been investigated using STS. The involvement of the rest atom in the bonding geometry has been confirmed through the missing rest atom state at -0.8 V. Two adsorbate states located at -1.3 V and +1 to +2 V have been identified and it matches well with the bias threshold for the desorption of chlorobenzene from the Si(111)-(7×7) surface at negative bias. The effect of the surface step and the temperature on the non-local chlorobenzene desorption process has been investigated. It shows that in the non-local chlorobenzene desorption process, the electron travels into the bulk and then scatters back to the surface and the non-local desorption process is assisted by the phonon at low temperature.

Different reactions generated by STM of the PCB molecule on the Si(111)-(7×7) surface have been studied, including desorption, reconfiguration and "seesaw". Different reactions show different site- and energy- dependence. While molecular desorption is maximized by electron injection into the chemisorbed molecular ring at low voltage, injection into the physisorbed molecular ring above a threshold voltage (+2.5 V) favours the reconfiguration of the bonding. This indicates both intramolecular charge localization and intramolecular charge

transportation within the PCB molecules during the manipulation.

The mucin molecule has been studied by AFM and STM on both the bare HOPG surface and the gold cluster-decorated HOPG surface in both the liquid and the dehydrated states. An unraveling manipulation has been achieved by STM over a folded mucin polymer on the bare HOPG surface, where the mucin monomer maybe unfolded one piece at a time. Enhanced mucin-substrate binding has also been achieved in the liquid state on the size-selected Au_{55} cluster-decorated HOPG surface. This demonstrates the efficiency of the gold cluster decorated HOPG surface for binding the mucin molecule.

Acknowledgements

I would like to thank my supervisor Prof. Richard E Palmer for allowing me the privilege of my studying at the NPRL and presenting my work in this thesis. Without his support, I would not have been able to start, continue and finish my study in this project. His wisdom and guidance always encourages me to perform to a better level.

I would like to thank my trainer Dr. Peter A Sloan for his training, guidance and help. His support has been vital to my study, not just experimentally, but also theoretically and practically. His enthusiasm for physics has been a constant inspiration to me during my study.

I would like to thank Dr. Feng Yin for his advice and help not just in the AFM experiment, but also for his useful suggestions, discussions and support.

I would like to thank my partner Dr. Sumet Sakulsermsuk for his help in the STM experiment, and for his company in study and life. With him, my life during the study has been more joyful.

I would like to thank Dr. Quanmin Guo and Dr. Wolfgang Theis for their advice and my classmates James for his help in AFM, Mi Yeon for her help in chemical preparation, Jedsada for his help in SEM; and Ruth, Simon, Lin, Charlotte and Miriam for reading and correcting my thesis. I would also like to thank all the former and the present NPRL members for their company.

Finally, I would like think my parents for supporting me in my PhD study and my beloved motherland.

Contents

Chapter 1 Introduction

The ability of the scanning tunnelling microscope (STM) to probe [1] and subsequently manipulate atoms on the surface, the atomic manipulation became possible after the early 1990s [2] and has attracted much interest [3-7]. Early experiments were mainly conducted at low temperature, here we are interested in the atomic manipulation at room temperature condition and the mechanism within it.

The first aim of this project was to further understand the STM induced desorption process (molecular manipulation) of chlorobenzene on the Si(111)-7×7 surface at room temperature by using the scanning tunnelling spectroscopy (STS) technique and to investigate the potential effect of the step and the temperature to non-local chlorobenzene desorption.

The second aim was to probe the STM induced site and energy dependent reaction processes of polychlorinated biphenyl (PCB) on the same surface under the same condition using both the STM and STS techniques.

The final aim was to prepare a condition where the possible SPM induced S-S bond breaking can be investigated in a bio-molecule to further the research from the simple organic molecule in the UHV condition to the more complicated bio-molecule in the ambient condition. Here we present AFM and STM investigations of the bio molecule mucin on both the bare highly ordered pyrolytic graphite (HOPG) surface and the gold cluster decorated HOPG surface and show some striking mechanical manipulation properties.

This thesis is constructed as follows: Chapter 2 introduces the STM techniques and the theory related to the imaging process in STM together with AFM. We then discuss STS theory and

basic principles of the method used in this thesis followed by brief reviews of STM the atomic manipulation. Chapter 3 contains the experimental detail of the STM instrument, the UHV system, the data analysis method for the STS and non-local desorption and finally the benchtop SPM instrument and the experimental method for the bio-molecule. Chapter 4 presents STS of the chlorobenzene molecule on the Si(111)-7×7 surface. It also presents the effect of the step and the temperature on the non-local chlorobenzene desorption process. Chapter 5 presents the atomic manipulation of the PCB molecule. Site and energy dependent manipulation for different reactions have been achieved and are explained through data from the STS investigation of this molecule. Chapter 6 comprises results of the bio-molecule manipulation. The mucin molecule was investigated using both AFM and STM on the bare HOPG surface and the gold cluster-decorated HOPG surface. Unfolding of a folded mucin polymer has been achieved and the gold cluster-decorated HOPG surface is shown to be of use in enhancing mucin binding; this subject is ideal for the future investigation.

Chapter 2 Scanning probe microscopy and atomic manipulation

In this chapter, the principle of STM and AFM as well as the theory of STM and STS is introduced. The three main mechanisms of the atomic manipulation have been described, including the manipulation induced by the mechanical interaction, the electric field and the inelastic electron tunnelling. Then different types of atomic manipulation have been categorized and introduced respectively, including lateral manipulation, vertical manipulation, desorption, transformation, dissociation, association, combined manipulations and other applications.

2.1 Scanning probe microscopy (SPM)

2.1.1 Scanning tunnelling microscopy (STM)

2.1.1.1 Principle of STM

The scanning tunnelling microscope (STM) was invented in the early 1980s [8]. It is widely used, due to its ability to produce three-dimensional surface images and local electronic-structure spectroscopy. According to quantum mechanics theory, electrons can pass (tunnel) a barrier even if the energy of electrons is lower than the height of the barrier. This is prohibited in classical mechanics. This quantum tunnelling is the fundamental principal behind the STM. When two metals brought close together and biased, electrons inside them should be able to

tunnel from one side to another.

In the STM, these two objects are the tip and the sample (Fig. 2.1). The resulting tunnelling current is exponentially dependent on the gap. By measuring the tunnelling current with respect to the tip displacement position over the surface, one can form the topography of this surface. Since the sensitivity of the tunnelling current to the gap is high (~0.01 Å) and the spatial resolution of this topography is ~1 Å, the STM has the resolution to "see" atoms.

Tunnelling can only happen when the gap between the tip and the sample is ~1 nm. In order to achieve this, precision control of the gap is required. Piezoelectric crystals have a property whereby a change in voltage across the crystal results in a small change in its length. In the schematic Fig. 2.1, the piezoelectric is split into three sections, one to control the tip height z and two to control the x and y rasters. Two Chinese characters written at atomic scale is shown in Fig. 2.2.

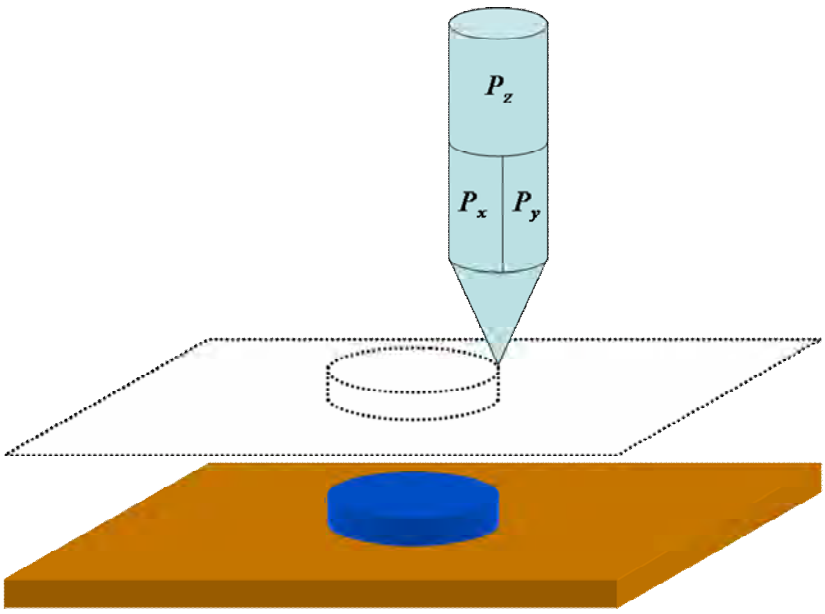

Figure 2.1 A schematic picture shows the principle of STM. P_x, P_y and P_z represent piezodrives, respectively. P_x and P_y enable the scan tube raster over the 2D surface, while the P_z enables the scan tube approach or retract from the surface in order to maintain the preset tunneling current.

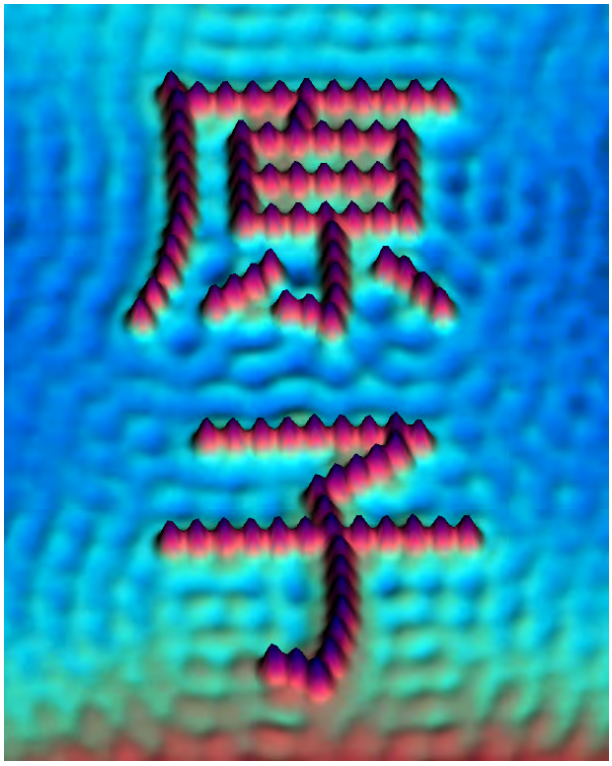

Figure 2.2 An STM image of a word “atom” written in Chinese character by Fe atoms on the Cu(111) surface. (From ref. [9])

Generally, there are two STM imaging modes, the constant current mode and the constant height mode. In constant current mode, the tunnelling current is maintained constant by the feedback loop (described in detail in section 3.1.1) during the scanning, while the bias voltage is fixed and the piezotube is changing in z direction with respect to the surface topography. All STM images presented in this thesis were acquired in the constant current mode, unless otherwise mentioned. In constant height mode, the piezotube is fixed in z direction with the feedback loop off during the scanning, while the bias voltage is fixed and the tunnelling current is changing with respect to the surface topography.

2.1.1.2 Theory of STM

As already illustrated in many textbooks [10], solving the Schrödinger's equation inside a one dimension rectangular barrier results in the wave function

$$\psi = e^{-\kappa d} \tag{2.1}$$

where κ is,

$$\kappa = \sqrt{\frac{2m(\phi - E)}{\hbar^2}} \tag{2.2}$$

In this solution, d is the distance into the rectangular barrier from where electrons come. ϕ is the height of this rectangular barrier. E is the energy of the electron. This is similar as the circumstance between the tip and the sample in the STM, where electrons tunnel from one side to another through the vacuum. In the STM, E transforms to eV which indicates the energy of an electron gained by the bias voltage, with respect to the Fermi level of the other side. ϕ transforms to the vacuum barrier. d is replaced by z which represents the gap between the tip and the sample. Then also based on quantum mechanics, the probability of finding an electron on the other side of the barrier of width z is the square of the absolute value of the wave function $\psi(z)$ which is proportional to the tunnelling current,

$$I \propto e^{-2\kappa z} \tag{2.3}$$

Most material has a work function around 4-5 eV, so κ is ~1 $Å^{-1}$ [10]. This means that a change in the gap by 1 Å results in a change in the tunnelling current by a factor of ten. It is the high sensitivity of the tunnelling current to the gap that enables the STM to work.

Given by the Bardeen's perturbation theory [11], the tunnelling current is

$$I = \frac{2\pi e}{\hbar} \sum_{\mu,\nu} [f(E_\mu) - f(E_\nu)] \left| M_{\mu\nu} \right|^2 \delta(E_\nu + eV - E_\mu) \tag{2.4}$$

This formula is given under the assumption of a weak tip-sample coupling. Inside the formula, *f(E)*, V and $M_{\mu\nu}$ are the Fermi function, the applied voltage and the tunnelling matrix element between two states. E_μ and E_ν stand for the energy of states in each electrode, respectively. This formula is complicated and difficult to directly interpret. It can be simplified through various assumptions. For example, using the zero temperature value for the Fermi distribution function, thus it becomes a step function, using an ideal "point source of current" to model the tip and assuming that the wave function of the tip does not affect much to the resulting tunnelling current. Even after all these have been done, it is still not easy to calculate it quantitatively.

Hence, Selloni *et al.* [12] suggested a qualitative interpretation based on Tersoff and Hamann's result [13]. This expression neglects the spatial dependence of the tunnelling current, yielding the expression

$$I(V) \propto \int_{E_F}^{E_F+V} \rho(E) T(E,V) dE \tag{2.5}$$

Here $\rho(E)$ and $T(E,V)$ stand for the local density of states at or near the surface and the barrier transmission coefficient, respectively. From this expression, one thing can be known that is the tunnelling current corresponds to the local density of states of the sample and the transmission coefficient. Furthermore, only the states between the $E_F \pm eV$ and E_F would participate the tunneling [1], as shown in Fig. 2.3.

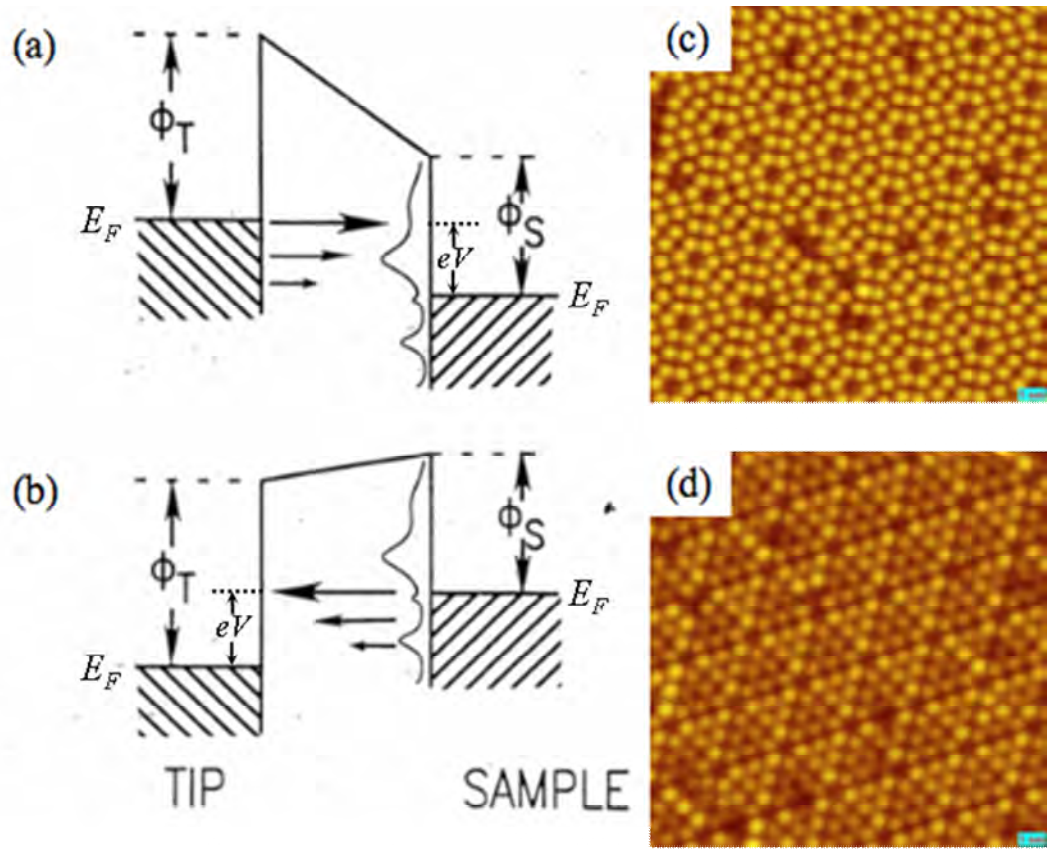

Figure 2.3 Diagrams show the energy level of the tip and the sample at different polarity: (a) positive bias, (b) negative bias; STM images taken at positive bias (c) and negative bias (d) of the Si(111)-7×7 surface. E_F, eV *and* ϕ stand for the Fermi level, the applied bias energy and the work function, respectively. The bias is with respect to the tip which is grounded. ((a)-(b) from ref. [14])

2.1.2 Atomic force microscopy (AFM)

Not long after the invention of the STM, the atomic force microscope (AFM) was invented in 1986 [15]. The principle of AFM is similar as that of the STM, both of them make use of the piezoelectric tube to change the small detection signal into the movement of the detector and by recording this movement to acquire the information of the surface. The difference between the AFM and the STM is that instead of monitoring the changing tunnelling current generated between the tip and the target, the changing force generated between them is monitored.

The main source of the force in the AFM is the Van der Waals force. According to the theory, when two objects brought close together, i.e., the tip and the sample, this force first acts like an attractive force, which the dispersion effect will become stronger and dominate. Afterwards, as the distance gets closer, the repulsive force becomes dominating due to the Pauli exclusion principle. The resultant force during the process is shown in Fig. 2.4. Many other forces may also play a role, including the capillary force, the electrostatic force and the magnetic force, etc. The net force generated by these forces, felt by the tip is strongly dependent on the distance between the tip and the sample.

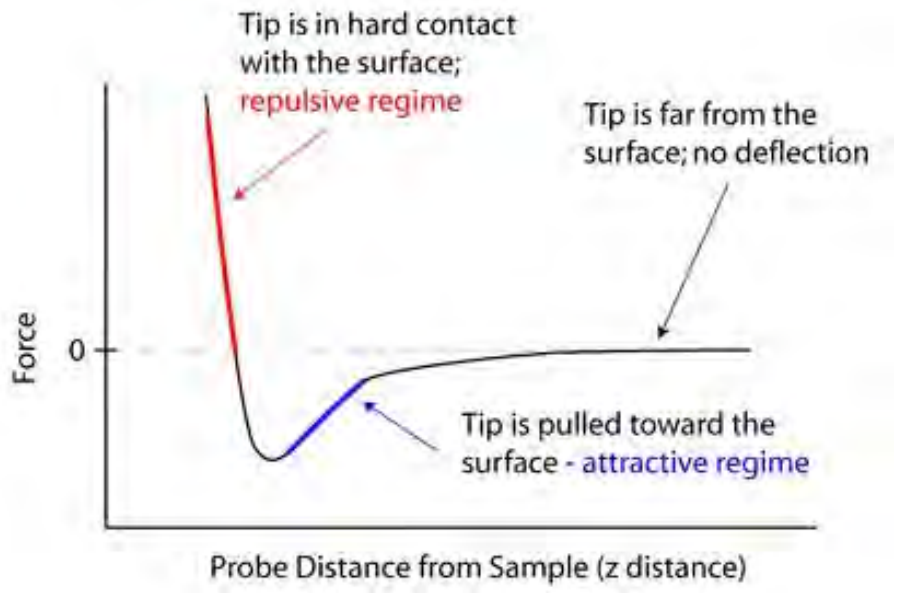

Figure 2.4 The resultant force generated between the tip and the sample versus the tip distance from the sample. (Image from [16])

By measuring the changing force with respect to the tip displacement position over a 2D surface, one can form the topography of the surface. This is similar as the STM, but the measurement is changed from the electrical signals to the force which is represented by the deflection of the cantilever of the AFM tip. Normally, the deflection is monitored by the

displacement of a laser beam reflected on the back side of the cantilever. This displacement is then changed into the electrical signals from the laser detector. Thus there is an advantage of the AFM over the STM that the tip and the sample do not need to be conductive. Therefore the AFM can be applied to a wider field.

There are three working modes for AFM. The first mode is the contact mode, where the tip is always "touching" the surface. The deflection of the tip is maintained during the measurement. The second is the tapping mode, where the tip is oscillating and "touching" the surface continually. The amplitude of the tip's oscillation is maintained during the measurement. The last one is the non contact mode, where the tip is oscillating but not "touching" the surface. Since the force inflicted on the tip by the surface changes the oscillation frequency of the tip as the gap between the tip and the surface changes, by maintaining the oscillation frequency of the tip during the measurement, the surface morphology can be acquired.

2.2 Scanning tunnelling spectroscopy (STS)

As well as the topography of the surface, the STM can access more information of the surface by the way of scanning tunnelling spectroscopy. From Eq. (2.5), only electrons from the states between the Fermi level E_F to the level $E_F \pm eV$ can join the tunnelling process, thus changing the bias voltage and recording the corresponding change in tunnelling current can give us some information of the local density of states of the surface over the probed voltage range.

However, both I versus V curve and dI/dV versus V curve cannot give a reasonable approximation of $\rho_s(E)$, because $T(E, V)$ is both tip sample separation dependent and voltage

dependent. In order to overcome this problem, Stroscio, Feenstra, and coworkers [17, 18] suggested a solution which is dividing the differential conductance by the static conductance. After applied such normalization, Eq. (2.5) will change into an expression like

$$\frac{\frac{dI}{dV}}{\frac{I}{V}} = \frac{\rho_s(eV)T(eV)}{\frac{\int_0^{eV}\rho_s(E)T(E)dE}{eV}} + \ldots \tag{2.6}$$

Feenstra argued that due to the appearance of the transmission probability in both the numerator and the denominator, their separation and voltage dependences should be canceled [19]. Finally, if only the first term of the expression is considered (the second term can be neglected for it does not affect too much the spectrum), this normalized differential conductance reflects a normalized surface density of states. The example of this method is given in Fig. 2.5, where it is applied to *I*-*V* curves acquired at different sample-tip separation on Si(111)-(2×1), the normalized spectrum matches well with the local density of states.

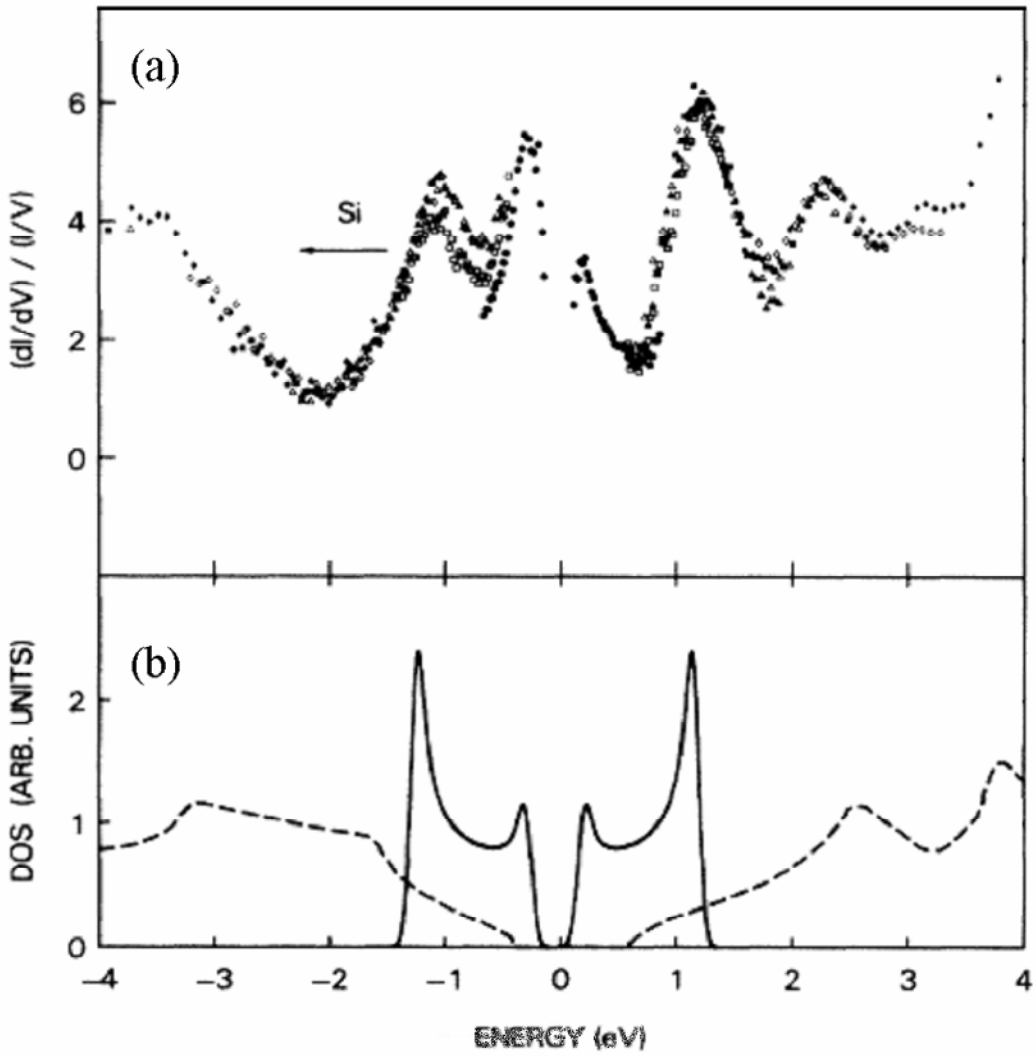

Figure 2.5 The normalized STS spectra of Si(111)-(2×1) surface compared with the DOS form theory: (a) The normalized STS spectrum. (b) The solid line and the dashed line show the calculated density of state of the surface and the bulk, respectively. (Images and caption modified from ref. [10])

Nevertheless, saying that (d*I*/d*V*)/(*I*/*V*) is the real density of states of the surface is not correct. One of the reasons is the normalized spectrum will diverge in the band gap region where the current and the differential conductance both go to zero. Therefore another procedure, fitting the entire *I*-*V* curve to a smooth function should be applied. In this thesis, Feenstra's (d*I*/d*V*)/(*I*/*V*) normalization method is applied to generate STS curves which is illustrated in section 3.3.1.

2.3 Literature review of atomic manipulation

After the invention of the STM by Binnig and Rohrer in 1980s, people for the first time attained the ability to "see" the surface with atomic resolution [8]. Later, as the research moves on, people noticed that the STM cannot only probe but also manipulate the matter at the atomic scale. Three main factors have been found to be the cause of this, the mechanical interaction between the tip and the target object, the electric field generated by the tip and the tunnelling current passed through the tip. Research progress in this field is reviewed below.

2.3.1 Mechanism for atomic manipulation

After the first intentioned atomic manipulation was demonstrated by the Eigler *et al.* [2], arranging Xe atoms on the Ni surface at low temperature to write the IBM logo, varieties of different manipulations and different applications have been developed. The principle of these manipulations can be classified into three main types as described below.

Manipulation induced by mechanical interaction

The atomic manipulation can be induced by the mechanical interaction between the very end atom of the tip and the target atom, when they are brought into proximity. The experiment conducted by Eigler *et al.* [2] on the Ni(110) surface at 4 K arranging Xe atoms into a desired

pattern gives an example of this procedure. The whole experiment is done in steps shown in Fig. 2.6. First the surface was scanned by STM to locate the target atom, and then the STM tip was positioned over a target Xe atom. Afterwards the set tunnelling current was adjusted to a higher value, where the tip was brought closer to the target atom, with the STM working in the constant current mode. The STM tip was then moved to a new desired position at a relatively slow speed; the Xe atom would move as the STM tip moved due to the strong interaction (attractive force) between the tip and the atom, and the relatively weak interaction between the atom and the surface. Once the STM tip reached the new position, the set current was changed back and the STM tip was retracted from the atom. As the gap between the tip and the atom was increased, the Xe atom stayed in the new position without following the movement of the STM tip afterwards. One Xe atom was moved at a time until the IBM logo was complete, as shown in Fig. 2.7. The certain height threshold, together with the independence of the sign and the magnitude of the bias voltage found in this experiment, indicates that this procedure is due to the mechanical interaction between the STM tip and the atom.

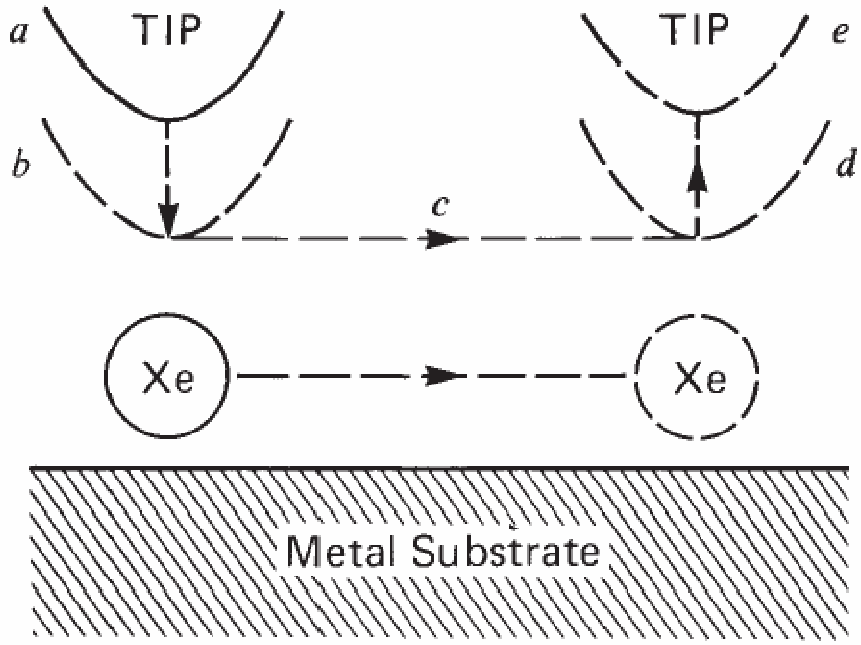

Figure 2.6 Image demonstrates steps (a)-(e) used for the arrangement of Xe atoms. (Image from [2])

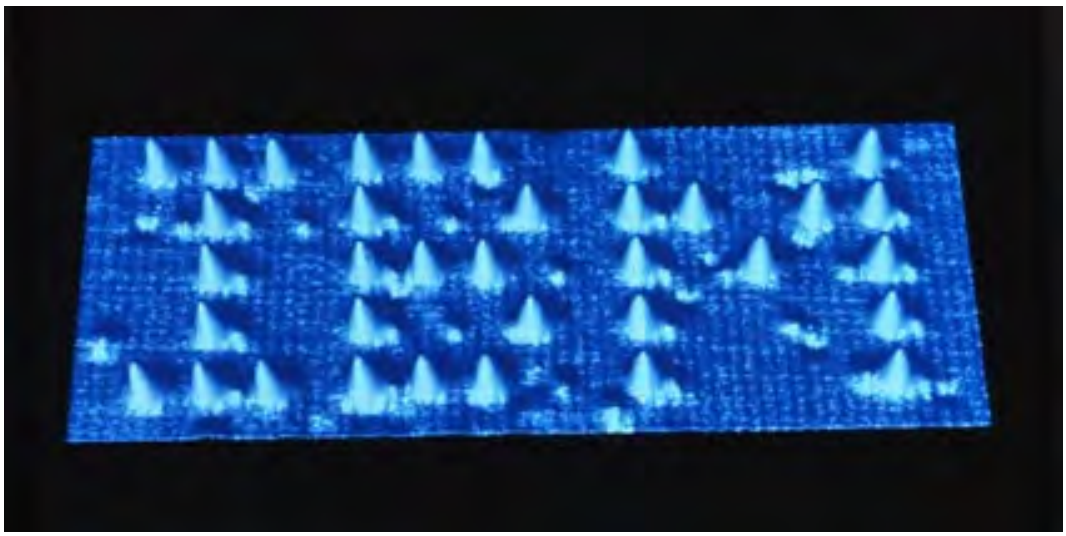

Figure 2.7 The IBM logo created by 35 Xe atoms on the Ni(110) surface. (Image from [20])

Manipulation induced by electric field

The atomic manipulation can also be induced by the electric field generated by the applied bias voltage between the STM tip and the surface. The experiment conducted by Whitman *et al.* [21] on both the GaAs(110) surface and the InSb(110) surface at room temperature for the

field induced diffusion of deposited Cs atoms gives an example of this procedure. It was found that by applying a pulse above a certain voltage threshold for a certain time, Cs atoms were attracted and diffused to the position beneath the STM tip. STM images in Fig. 2.8, taken before and after a pulse of +1.0 V for 0.35 s being applied in the centre of the image, clearly show the field induced diffusion of the Cs atoms connecting to longer chains or forming new chains. The principle of this procedure, as described in this paper, concerns the dipole moment ***p*** of an adsorbate in an electric field ***E***

$$\mathbf{p} \cong \boldsymbol{\mu} + \alpha \mathbf{E} \tag{2.7}$$

where $\boldsymbol{\mu}$ is the static dipole moment of the adsorbate and α is the polarizability of the adsorbate. Then the modified amount of potential energy of this adsorbate is

$$U_E(\mathbf{r}) \cong -\boldsymbol{\mu} \cdot \mathbf{E} - \frac{1}{2}\alpha \mathbf{E} \cdot \mathbf{E} \tag{2.8}$$

Due to the presence of this additional potential generated by the electric field, the adsorbate experiences a force, in the radial direction

$$\frac{dU_E}{dr} \cong -(\mu + \alpha E)\frac{dE}{dr} \tag{2.9}$$

Since the extension of the electric field presented beneath the STM tip is nonuniform, this force is also nonuniform, causing the assembly of the Cs atom (in this case this force is attractive). Furthermore, it was also noticed that at certain bias voltage which is above the threshold of diffusing the Cs atom, longer time would result in more coverage of Cs atoms. However, there was a limit for the coverage, if higher density was required, higher bias voltage needed to be applied. This indicates that this atomic manipulation is driven by the electric field instead of the tunnelling electron or the mechanical interaction.

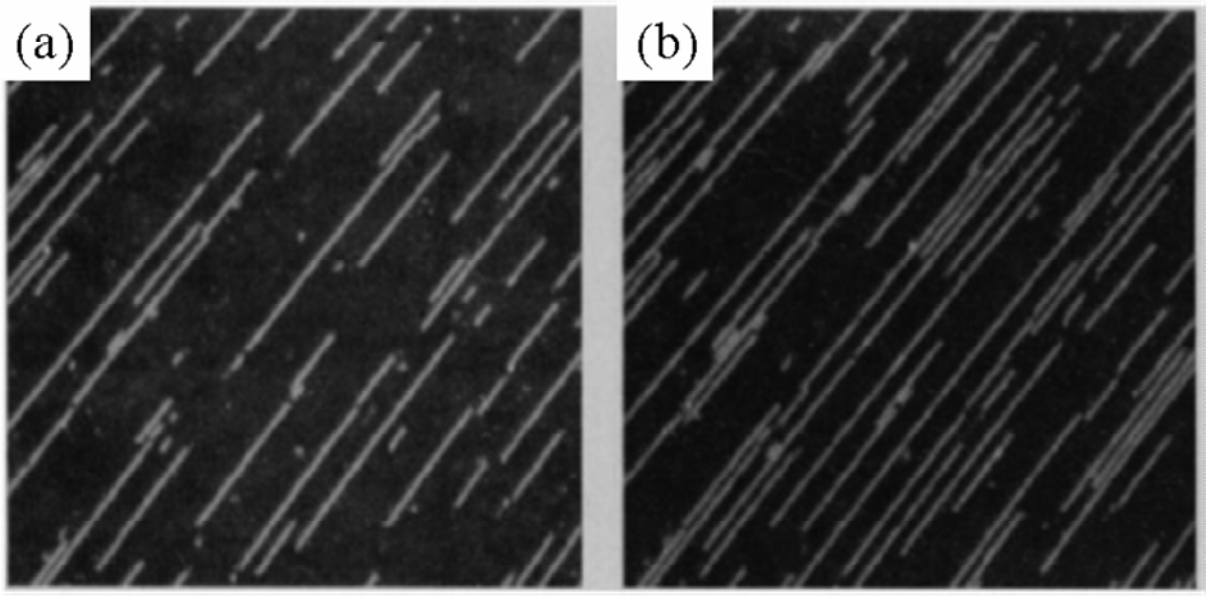

Figure 2.8 STM images (140 nm × 140 nm) show the Cs atom on the p-GaAs(110) surface before (A) and after (B) a pulse (+1 V for 0.35 s) applied in the position of the centre of the image. (Images and caption modified from [21])

Manipulation induced by inelastic tunnelling

Another way of performing atomic manipulation is through inelastic tunnelling of the injected electron. The experiment conducted by Stipe *et al.* [22] on the Pt(111) surface at 50 K for the O_2 molecule dissociation process demonstrates such a procedure. After the deposition of O_2 molecules, the surface was annealed at higher temperature to eliminate unstable physisorbed O_2 molecules. It was found that after applying a pulse over the "pear" shape O_2 molecule, two new products were generated on the surface where the dissociation process was believed to happen. This process is shown in Fig. 2.9.

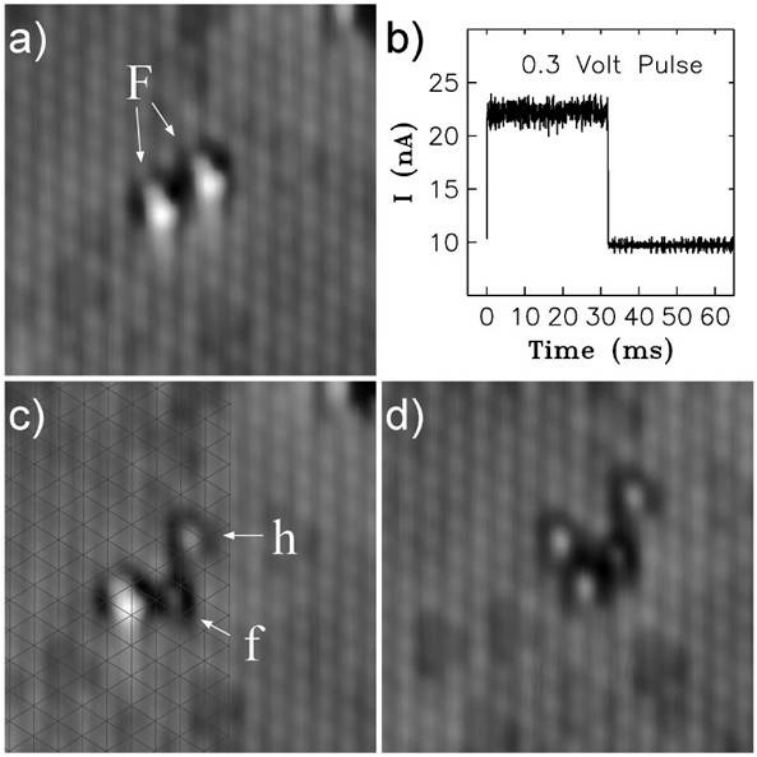

Figure 2.9 (a) An STM image of two pear shaped O_2 molecules on fcc sites of the Pt(111) surface. (b) Recorded current during the pulse (0.3 V) on the molecule on the right in (a), while the dissociation process happened. (c) An STM image of (a) after the pulse, where two new generated oxygen atoms are indicated by arrows. (d) An STM image of (c) after the pulse applied on the molecule on the left. (Images and caption modified from [22])

Different bias voltage pulse experiments over many O_2 molecules were tested, and it was found that the probability of the dissociation event has a power law dependence on the current. This fits quite well with a model previously proposed to explain the desorption induced by the electronic transitions (DIET) process induced by the laser [23, 24]. According to this model, the probability of the event is proportional to the power of the current,

$$R_d \propto I^N \tag{2.10}$$

where the R_d is the dissociation rate, N is the number of electrons needed in this process and I is the current. Fig. 2.10 explains the mechanism proposed by the author of this experiment. The barrier is 0.35 to 0.38 eV, thus for an electron with enough energy, single electron dissociation would happen, however, if a single electron did not have enough energy, multiple

electrons were required for dissociation. Furthermore, to explain the dynamics induced by inelastic tunnelling electrons, both coherent [25, 26] and incoherent [27] inelastic resonance excitation theory have been proposed.

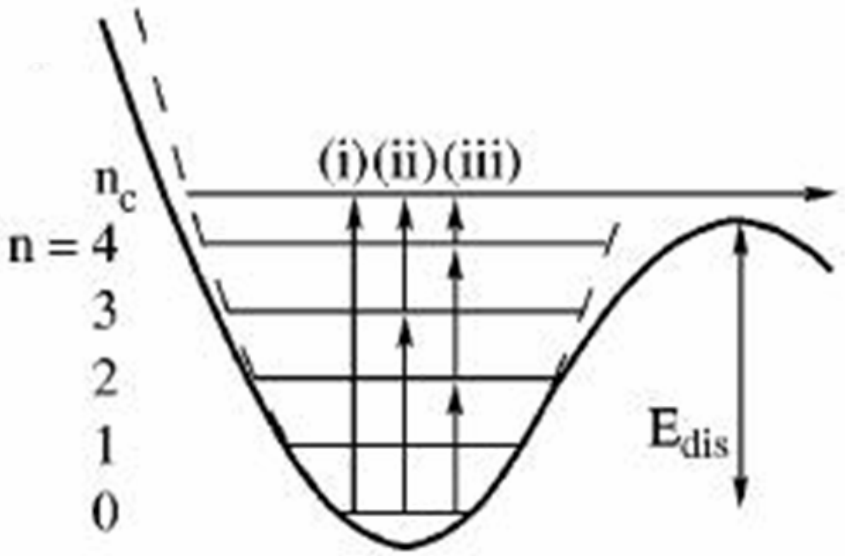

Figure 2.10 Schematic picture showing the model for bond breaking of O_2 on Pt(111) by inelastic electron tunnelling process. Potential energy well is modelled by a truncated harmonic oscillator (dashed line). n stands for the modelled energy level, n_c is the energy level needed for bond breaking. Three types of transitions under different applied bias voltages ((i) 0.4 V, (ii) 0.3 V, and (iii) 0.2 V) leading to the dissociation process are labelled respectively. (Image and caption modified from [22])

2.3.2 Applications for atomic manipulation

As main mechanisms for atomic manipulation has been described above, different applications of atomic manipulation will be introduced in this section. After the atomic manipulation was realised, different reactions of different molecules on different surfaces have been achieved. Generally, these reactions can be catalogued into following fields: lateral

manipulation, vertical manipulation, desorption, structure transformation, dissociation, fusion and multiple manipulations.

Lateral manipulation

In the very early stage of research in this field, it was found atoms or molecules could be moved laterally on the surface. Bartels *et al.* [28] demonstrated such process with various atoms and molecules deposited on the Cu(211) surface at 30 K. They showed that different molecules could be manipulated laterally under different modes mechanically. After the STM tip was lowered on top of the desired atom or molecule, the STM tip was then moved away parallel to the surface. The tip height versus the lateral distance graph shown in Fig. 2.11 was recorded with the tip working in constant current mode. It clearly shows the Cu atom "pulled" away by the STM tip, indicating the attractive force between the tip and the atom. In contrast, the CO molecule was "pushed" away by the STM tip, indicating the repulsive force between the tip and the atom. For the case of the Pb atom, another different mode of moving was apparent when the STM was positioned even closer, whereby the Pb atom was "sliding" on the surface. It should be noted that during this type of lateral manipulation, the surface might play a role. When the Pb dimer was pulled near the surface step-edge, double hopping was changed into single hopping. Similar phenomenon could be noticed in the experiment performed by Hla *et al.* [29] when the Ag atom was moved by the STM tip on the Ag(111) surface at 6 K, different manipulation signals were recorded when the tip was moving the Ag atom along different surface directions, indicating the effect from the surface corrugation.

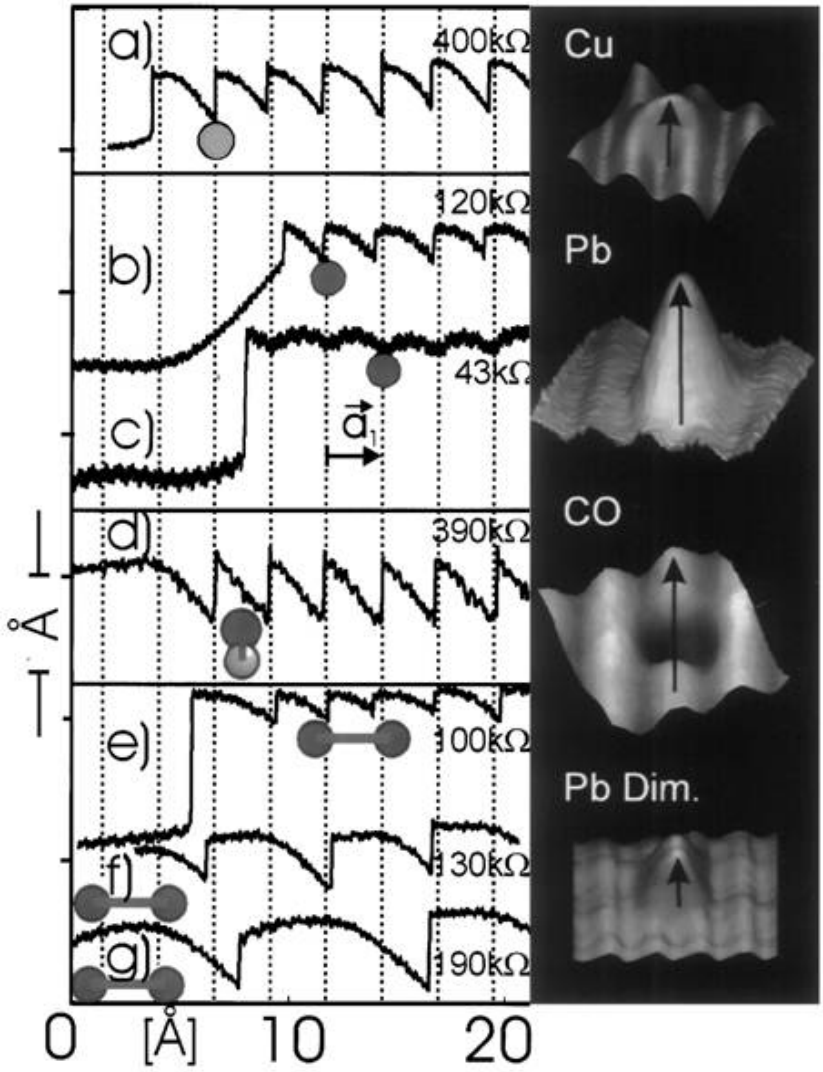

Figure 2.11 Tip height curves during the manipulation process together with STM images of adparticles. The left part shows tip height curves during the manipulation process of a Cu atom (a), a Pb atom (b, c), a CO molecule (d), and a Pb dimer (e)-(g) along $[1\bar{1}1]$ direction. The tip was moved from left to right. The right part shows STM images of different adparticles. (Images and caption modified from [28])

For bigger molecules, new modes of the lateral manipulation can also be observed. In the case of the C_{60} molecule deposited on the Si(100) surface at room temperature, Keeling *et al.* [30] noticed a periodicity signal in the height of the STM when they manipulated the C_{60} molecule along the surface in the constant current mode, as shown in Fig. 2.12.

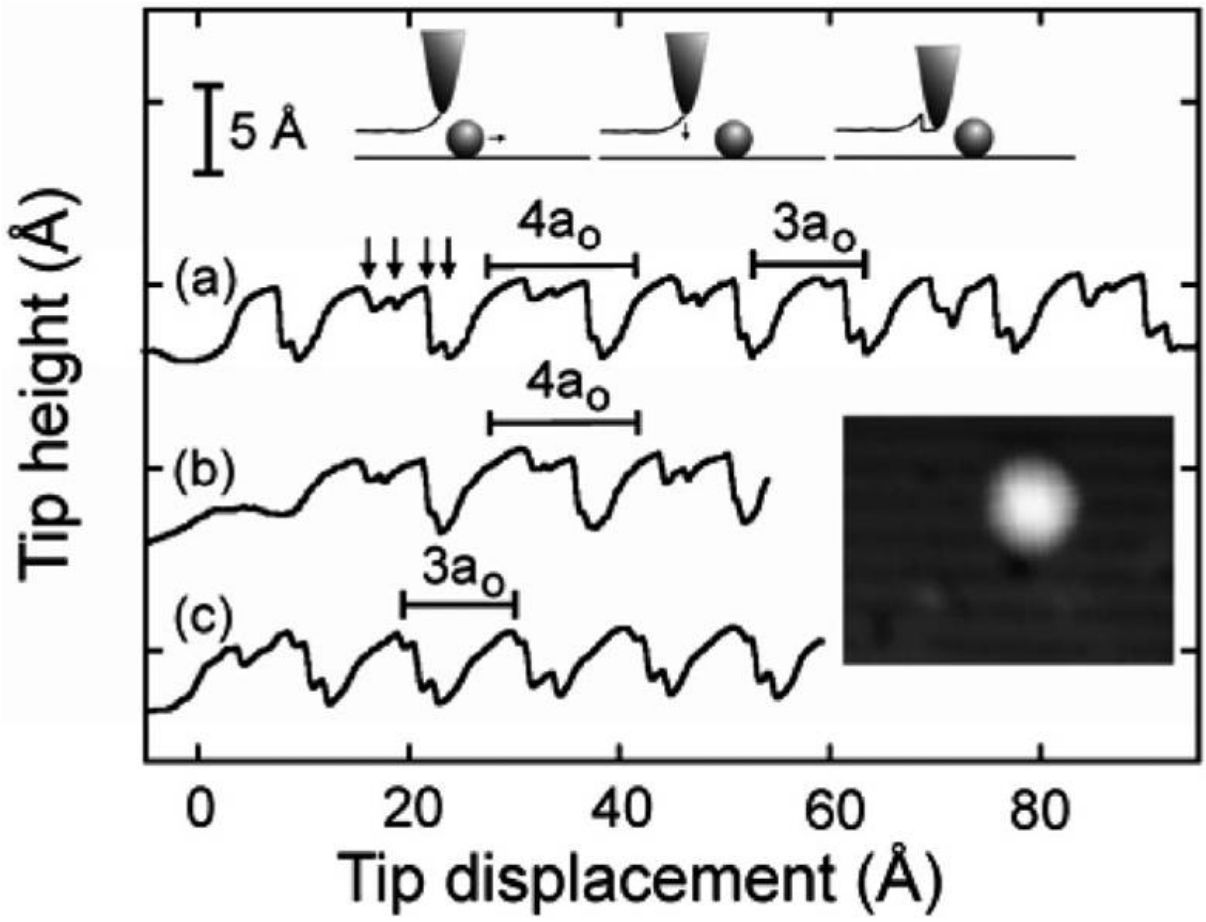

Figure 2.12 Tip movements during the repulsive manipulation process. (a) A Tip movement curve shows a period of $4a_0$ together with a short section of $3a_0$. (b) A Tip movement curve shows a period of $4a_0$. (c) A Tip movement curve shows periods of $3a_0$. (Image and caption modified from [30])

From simulation they found that if the C_{60} molecule moved laterally in such way that C-Si bonds broke and formed sequentially during the movement, as shown in the Fig. 2.13, a periodicity equalled to 4 lattice constants was apparent. This matches quite well with the signals they recorded during the experiment, indicating the C_{60} molecule was rolling along the surface during the mechanical manipulation. Similar motion driven by mechanical interaction was reported for other molecules as well, e.g., the wheel-dimer molecule ($C_{44}H_{24}$) rolling on the Cu(110) surface at room temperature [31].

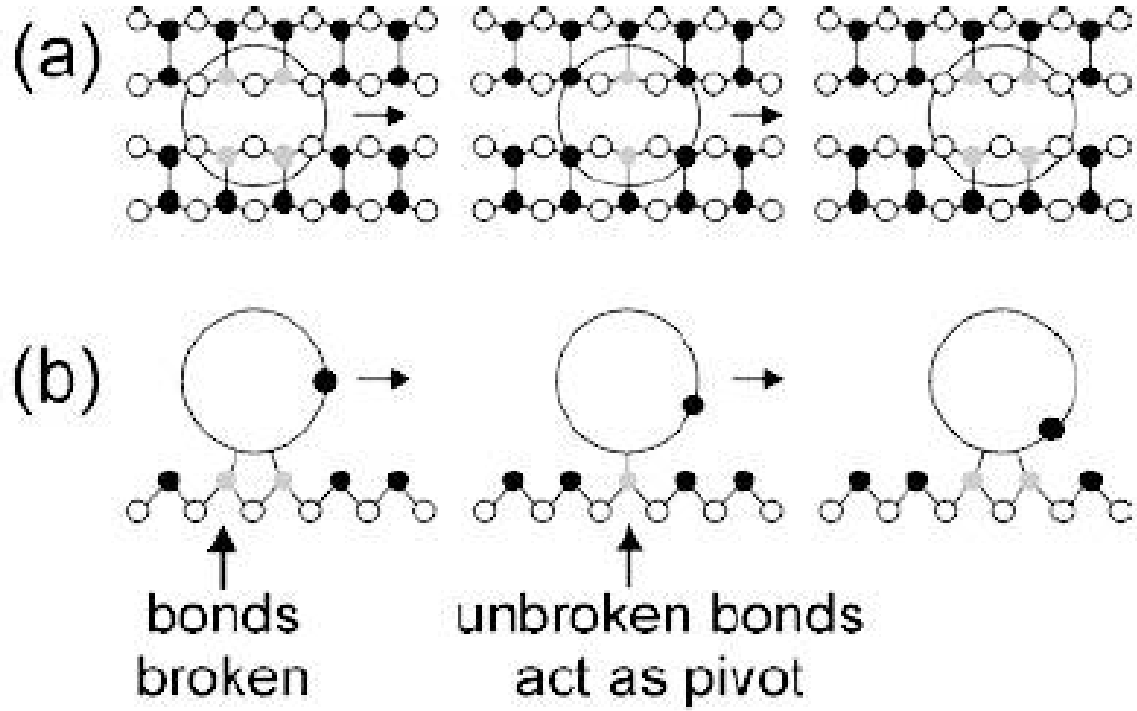

Figure 2.13 Schematic diagrams showing the proposed rolling mechanism for the manipulation process of C_{60}. Top view (a) and side view (b) of this process. Filled circles represent top layer Si atoms and empty circles represent second layer Si atoms, while grey circles represent Si atoms bonded with C_{60}. (Images and caption modified from [30])

Even bigger molecule, such as lander molecule 1,4-bis(4-(2,4-diaminotriazine)phenyl)-2,3,5,6-tetrakis(4-*tert*-butylphenyl) benzene (DAT, $C_{64}H_{68}N_{10}$) was studied on both Cu(110) and Au(111) surfaces at 110 K [32]. The DAT lander molecule was imaged as a big object having six bright spots as shown in Fig. 2.14. Generally by reducing the distance between the tip and the molecule, after the tip scanning over the lander molecule, different movements could be induced, including rotation and lateral translation. When the tip was scanned over the molecule in a direction which was not parallel to the middle line of the molecule, rotation could be induced to only three possible positions which were guided by the substrate. On the other hand, when the tip was scanned along the molecule, translation movement could be induced. The most interesting aspect was that when such manipulation was applied to the

molecule near the step edge, it could be pushed up from the lower terrace to the higher terrace.

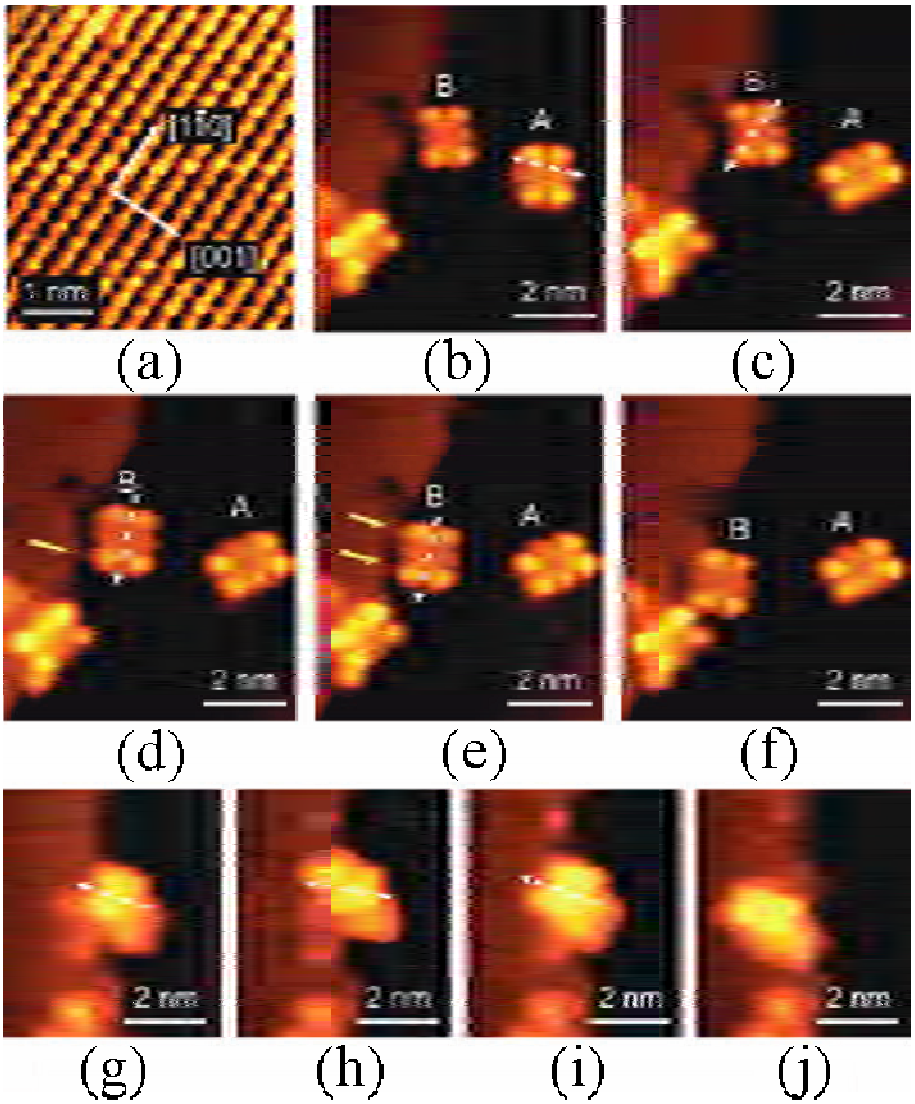

Figure 2.14 STM images shows DAT Lander molecules on the Cu(110) together with the manipulation process of the DAT Lander molecule. (a) Cu(110) surface. (b)-(f) Manipulation processes of the individual DAT Lander molecule on the Cu(110). Two manipulated molecules are labelled as A and B. (g)-(j) A DAT Lander molecule moved across a Cu(110) step edge from the low terrace to the high terrace. White arrows indicate tip manipulation directions. (Images and caption modified from [32])

Diffusion caused by inelastic tunnelling was also observed on surfaces by Katano *et al.* [33]. Formate molecules adsorbed on the Ni(110) at low temperature were found to diffuse on the surface by the electron injection. The formate on the Ni(110) was imaged as a single bright

dot with two depression regions nearby, as shown in Fig. 2.15 (a). There were two binding sites: the short-bridge site and the long-bridge site for the formate adsorption. Only the formate on the long-bridge sites was found to be metastable and result in diffusion upon electron injection. By comparing the diffusion yield as a function of the applied pulse voltage between the formate ($HCOO^-$) and its isotope counterpart ($DCOO^-$), two thresholds 140 mV and 360 mV for $HCOO^-$ and 110 mV and 270 mV for $DCOO^-$ were clearly seen, as shown in Fig. 2.15 (b). Furthermore, in the previous measurement, the C-H (C-D) bending mode and the C-H (C-D) stretching mode were found to be located at 134 (104) mV and 355 (271) mV, respectively. These agreements indicate that the excitation of the C-H bending mode and the C-H stretching mode by inelastic tunnelling electrons causes the increase in the diffusion yield.

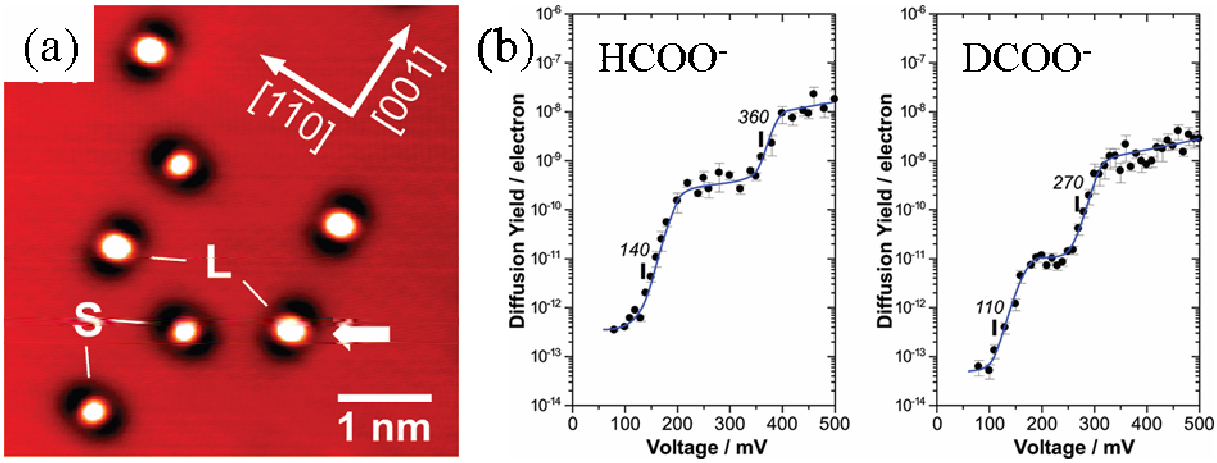

Figure 2.15 (a) STM image of formate ($HCOO^-$) molecules adsorbed on the Ni(110) surface. Formate molecules adsorbed at short bridge sites are indicated by S and formate molecules adsorbed at long bridge sites are indicated by L. (b) Action spectra of the diffusion of $HCOO^-$ and $DCOO^-$ molecules adsorbed at long-bridge site as a function of the applied pulses. (Images and caption modified from [33])

Rotation motion at a fixed location could be induced by the inelastic tunnelling. In the experiment performed by Stipe *et al.* [34], acetylene molecules were rotated in a fixed

position on the Cu(100) surface at 8 K. Acetylene molecule was imaged like a "dumbbell" in the system as shown in Fig. 2.16 (a). By positioning the tip over the molecule and recording the resulting current under the constant height mode, two bistable states could be found corresponding to the high and low signal positions in Fig. 2.16 (b). The rotation motion was driven by exciting the C-H stretch mode using the tunnelling electron. Furthermore, the rotation speed has also been investigated by comparing the acetylene molecule and the C_2D_2. Different excitation modes with different energy and different rotation speed were found for these two types of molecules. Rotation was also observed for formic acid molecules on Ni(110) at low temperature by tunnelling electrons [35]. Rotation out of the original position was reported, e.g., the biphenyl molecules on the Si(100) surface at 5 K by inelastic electron tunnelling [36-39].

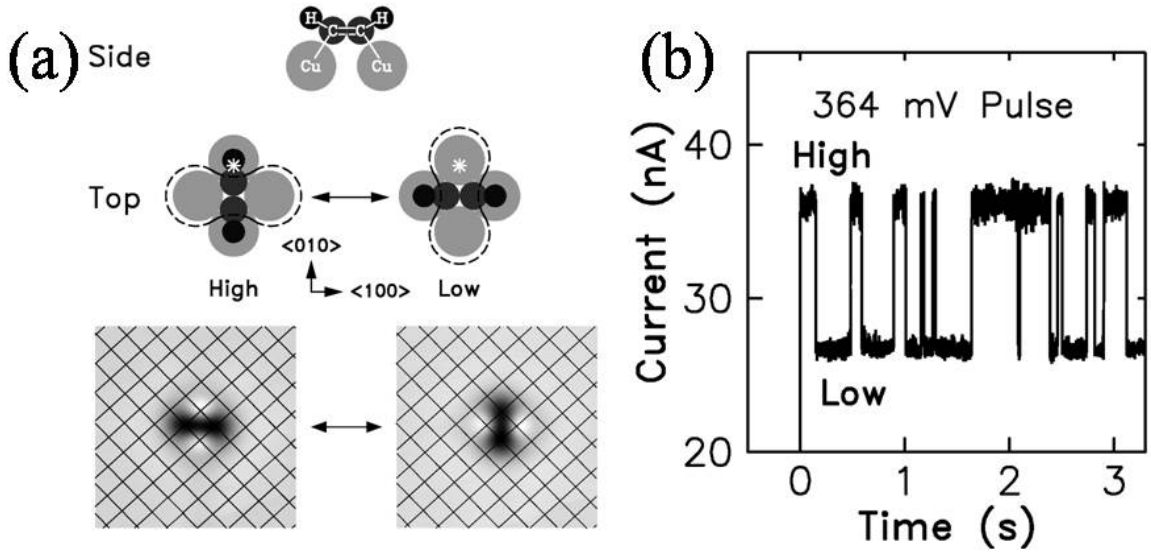

Figure 2.16 (a) Schematic diagrams of the acetylene on the Cu(100) surface from both top and side views. The area circled by the dashed line represents the place which is dimmer in STM images. (b) Recorded current during the rotation manipulation process under the 364 mV pulse over a acetylene molecule which was in the high current position in the beginning. (Images and caption modified from [34])

Non-local reaction

Non-local reaction could also be performed by the STM. As reported by Sloan *et al.* [40], non-local desorption of chlorobenzene molecules deposited on the Si(111)-(7×7) surface was observed at room temperature. After a pulse applied at +2.7 V for a certain time in the centre of the STM image, the surrounding chlorobenzene molecules could be "cleared" from the surface within a radius of up to 50 nm. By plotting the desorption yield $k_e f(r)$ as a function of the radial distance from the injection point,

$$k_e f(r) = -e2\pi r \ln\left[N(r)/N_0(r)\right]/stIL \tag{2.11}$$

a clear exponential decay was found. Afterwards, by positioning the tip carefully at different sites along the diagonal direction of the Si(111)-(7×7) unit cell, comprehensive non-local desorption experiments with respect to different injection sites within the unit cell were performed, as shown in Fig. 2.17(a). The data clearly showed that there was a injection site dependence of non-local chlorobenzene desorption. Since one threshold of the chlorobenzene desorption is +2.1 V in previous experiments [41, 42], integrated local DOS from +2.0 V to the injection voltage +2.7 V was measured along the diagonal direction of the Si(111)-(7x7) unit cell. Through the good agreement of the integrated local DOS data with non-local desorption data with respect to different injection sites as shown in Fig. 2.17, it was clear that the electron which induced the chlorobenzene desorption was transported through the surface states. What is more this surface state was found to be higher over corner hole sites, which led to a hypothesis that this surface state might lie below the first layer and the electron travels beneath the surface.

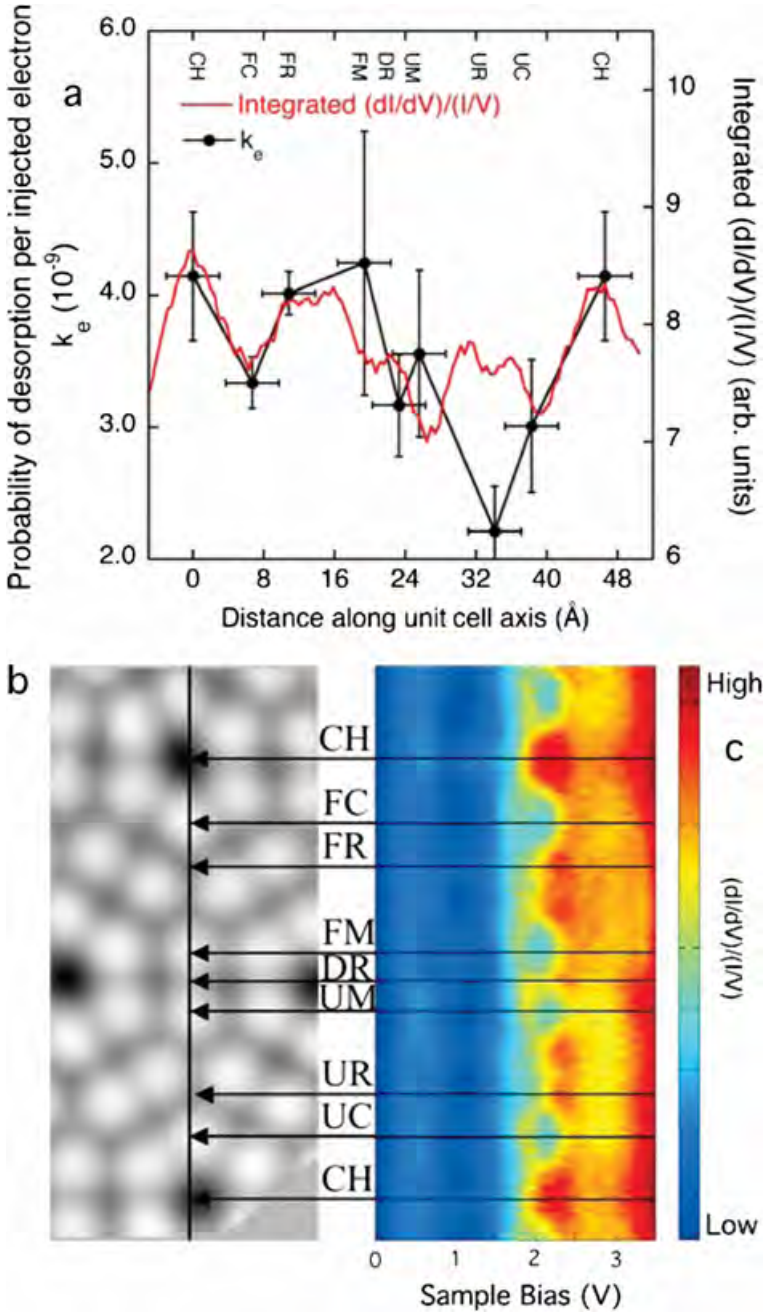

Figure 2.17 (a) Non-local desorption probability per electron of chlorobenzene molecules k_e under +2.7 V pulse (black line) at different sites on the surface. CH, FC, FR, FM, DR, UM, UR and UC stand for corner-hole, faulted corner adatom, faulted rest atom, faulted middle adatom, dimer row, unfaulted middle adatom, unfaulted rest atom and unfaulted corner adatom sites, respectively. The integrated STS data over +2.0 to +2.7 V of the clean surface is shown in the red line. (b) An STM image shows corresponding sites on the surface. (c) The STS data over different sites as indicated in (b). (Images and caption modified from [40])

The above case mainly focuses on the electron induced non-local reaction. However in fact, not only electrons could induce non-local reactions; but also holes could induce non-local

reactions. As reported by Bellec *et al.* [43], non-local activation of the hopping of a exposed hydrogen atom on the hydrogenated Si(100)-(2x1) surface was triggered by the STM at 5 K. A bistable dangling bond and hydrogen atom pair was first created by applying a pulse on top of one hydrogen atom. Afterwards by positioning the tip over either the dangling bond site or the hydrogen atom site with a negative pulse, this pair could be switched. More interestingly, this action could be triggered from several hydrogen dimers away on the surface by injecting holes at -2.5 V. Moreover, this non-local effect acted differently when the distance between the injection site and the bistable dangling bond and hydrogen atom pair site was changed, as shown in Fig. 2.18. When the distance was long enough, i.e., more than two dimmer rows, the hopping yield on the dangling bond site was higher than that on the hydrogen atom site across the dimmer rows. Along the dimmer rows, this was reversed. However, this process changed when the injection site was closer than two dimer rows. The hopping yield on the dangling bond site was higher than that of the hydrogen atom site across the dimer row direction, and it was the contrary along the dimer row direction. By plotting the local DOS of the Si-Si bond surface state in the region from -2.3 eV to -3.0 eV, it was found surface states were higher on the hydrogen atom site along the dimer row direction and on the dangling bond site across the dimer direction, whereas it showed no differences for longer distance. Thus different behaviours of the non-local injection induced hopping result from the anisotropic distribution of the LDOS near the dangling bond and hydrogen atom pair site and the isotropic delocalized surface state in the long range.

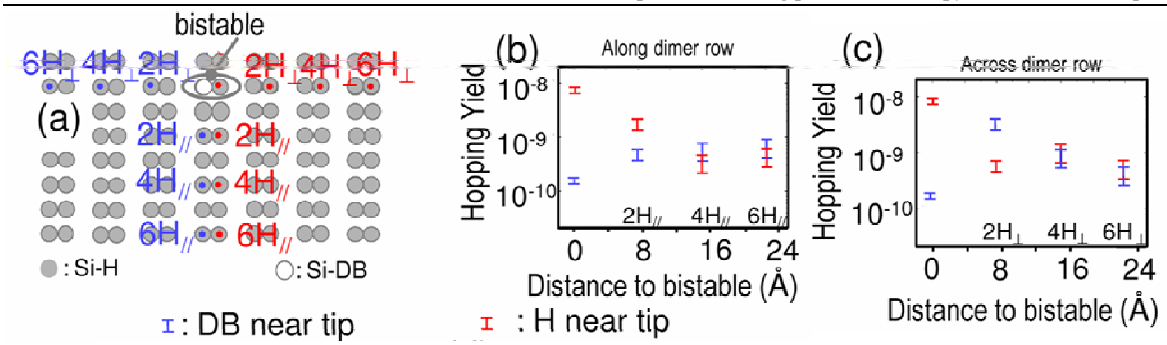

Figure 2.18 (a) A schematic diagram of the top view of the silicon dimers on the Si(100):H surface. 12 hole injection sites are indicated by blue and red dots. The blue dot stands for the injection over the H side, while the red dot stands for the injection over the DB side. The grey circle represent the H atom and the white circle represents the DB. (b)-(c) The hopping yields under hole injection (2.5 V) at different sites as indicated in (a). The red bar represents the case when the injection was near the H atom, while the blue bar represents the case when the injection was near the DB. (Images and caption modified from [43])

Various non-local reactions were also performed. The S-S bond dissociation of CH_3SSCH_3 molecules deposited on the Au(111) surface showed the non-local effect could be as far as 100 nm from the injection point [44]. Similar reactions were generated for the same molecular chain when the electron was injected in one end of the chain, resulting in changing of the whole chain [45]. Further examples include the close-packed C_{60} layer on the Si(111)-7×7 surface being turned into a ring of C_{60} polymers upon both the electron and the hole injection [46], or the Cl diffusion on the Si(111)-7×7 surface [47].

Vertical manipulation

Not just lateral manipulation could be performed by the STM, manipulation in the vertical direction could also be realized. In the experiment performed by Bartel *et al.* [48], the CO molecule could be "picked" up by the STM tip. The experiment was carried out on the Cu(111) surface at 15 K. They found that by positioning the tip over the CO molecule and gradually decreasing the voltage together with tip height, with the feedback off, the CO molecule could

hop to the STM tip when positive bias voltage was applied, and could hop back to the surface when negative bias voltage was applied. This "pick" up and "drop" process was demonstrated in Fig. 2.19. Later investigation [49] showed that this process was done through the excitation of the CO $2\pi^*$ state by tunnelling electrons and it was also found that by attaching a CO molecule to the tip, the contrast of the STM image could be improved. Atoms in the surface could also be vertically manipulated as well as molecules on the surface. The experiment done by Dujardin *et al.* [50], showed that individual germanium atoms could be extracted from the Ge(111) surface mechanically when the gap between the tip and the surface was zero.

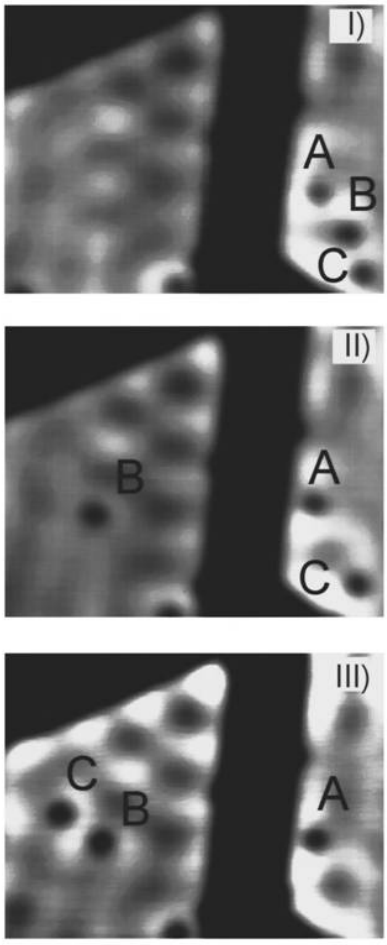

Figure 2.19 STM images shows the manipulation process of CO molecules on the Cu(111) surface. From I) to III), CO molecules were picked up and dropped from the right side to the left side sequentially. CO molecules are indicated by A, B and C. (Images and caption modified from [48])

Desorption

A variety of atoms and molecules investigated by the STM could be desorbed from the surface. The key molecule chlorobenzene investigated in this study was found to be readily desorbed, either thermally or by the STM. In the experiment performed by Sloan *et al.* [40] for the chlorobenzene molecule on the Si(111)-7×7 surface at room temperature, the chlorobenzene molecule was desorbed by either the electron or the hole injected from the STM tip as shown in Fig. 2.20. Two thresholds +2.5 V and -1.5 V were found for the desorption process. The desorption of the chlorobenzene should be from the excitation of the π state of the molecule, a one electron excitation process [41]. Other desorption process could also be observed, e.g., NO molecules desorption from the Si(111)-7×7 surface due to the electric field appeared beneath the STM tip [51].

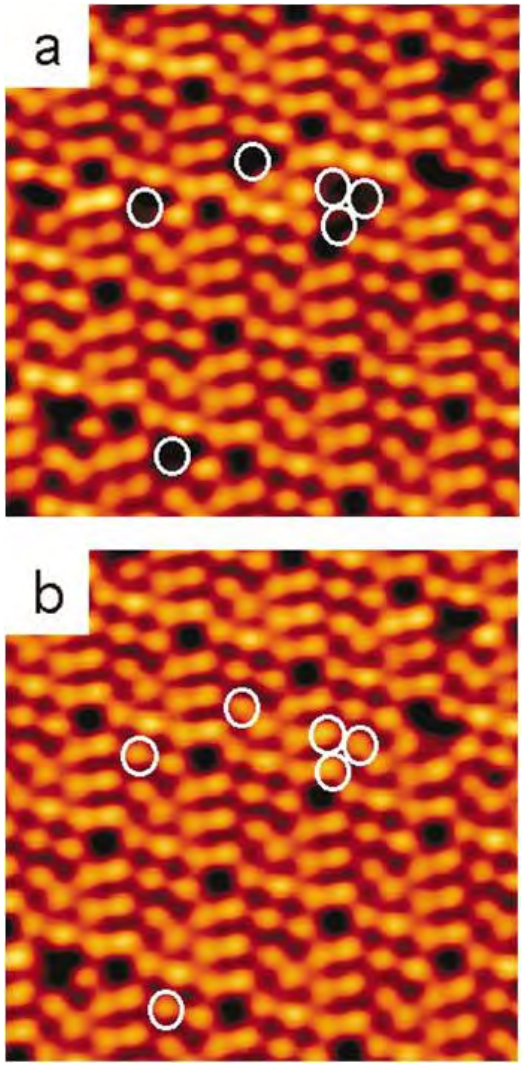

Figure 2.20 STM images of chlorobenzene molecules on the Si(111)-7×7 surface before (a) and after (b) scanning at a desorption voltage. White circles indicate the position where chlorobenzene molecules desorbed. (Images and caption modified from [40])

Transformation

Not just the position of atoms and molecules could be manipulated by STM, but also the structure itself could be changed. Leoni *et al.* [52] was able to change the structure of the bis-dibenzoylmethanato-copper ($Cu(dbm)_2$) molecule deposited by STM on NaCl islands grown on the Cu(111) substrate at 5 K. By applying a pulse at +2 V, the original square and planar $Cu(dbm)_2$ complex was transferred into a tetrahedral shape complex; this transformation was reversible when applying a pulse at -2 V, as shown in Fig. 2.21. This process was driven by

the tunneling electron. Furthermore, the electrostatic force measured by the AFM between the tip and the molecule under different states confirmed that the tetrahedral shape complex was negatively charged. In addition, the NaCl surface was essential for such reversible switching, since similar phenomena cannot be observed for the same complex on the bare Cu(111) surface.

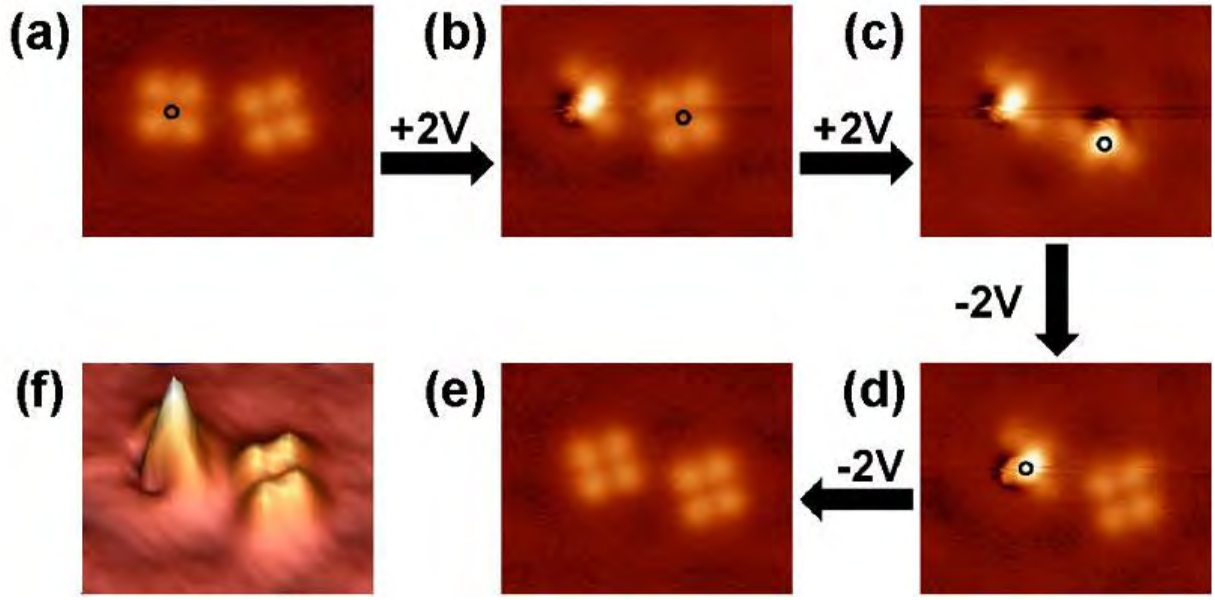

Figure 2.21 (a)–(e) STM images show the reversible switching of two $Cu(dbm)_2$ molecules. Black circles indicate the pulse positions. (f) A 3D image of (b). (Images and caption modified from [52])

Irreversible transformation of the 4-dimethylaminoazobenzene-4-sulfonic acid on the Au(111) surface at 5 K was done by Henzl *et al.* [53]. Reversible isomerization between a trans and a cis form of the azobenzene molecule and the alike on either the Ag(111) surface or the NaCl layer on the Ag(111) surface were also demonstrated at low temperature [54-59]. Other reversible or irreversible changes of the molecular structure were also reported [60].

Dissociation

Beside the dissociation of O_2 molecules described before, dissociation of certain bonds inside a more complicated molecule could be induced by the inelastic tunnelling. The experiment performed by Sloan *et al.* [61] for the chlorobenzene molecule on the Si(111)-7×7 surface at room temperature showed that for chlorobenzene molecules, not only desorption could be triggered, but also C-Cl bond dissociation could be triggered as well, as shown in Fig. 2.22. By positioning the tip over the chlorobenzene molecule and applying +3 V pulse, a new product, the Cl atom, could generated from the chlorobenzene besides the chlorobenzene desorption. By plotting the dissociation rate as a function of the tunnelling current, the number of electrons needed for the dissociation process was found to be ~1.8, which indicated that this process was a two electron process, different from that observed for the one electron desorption process. A later investigation [62] found that the thermal energy played an important role in this C-Cl bond dissociation process.

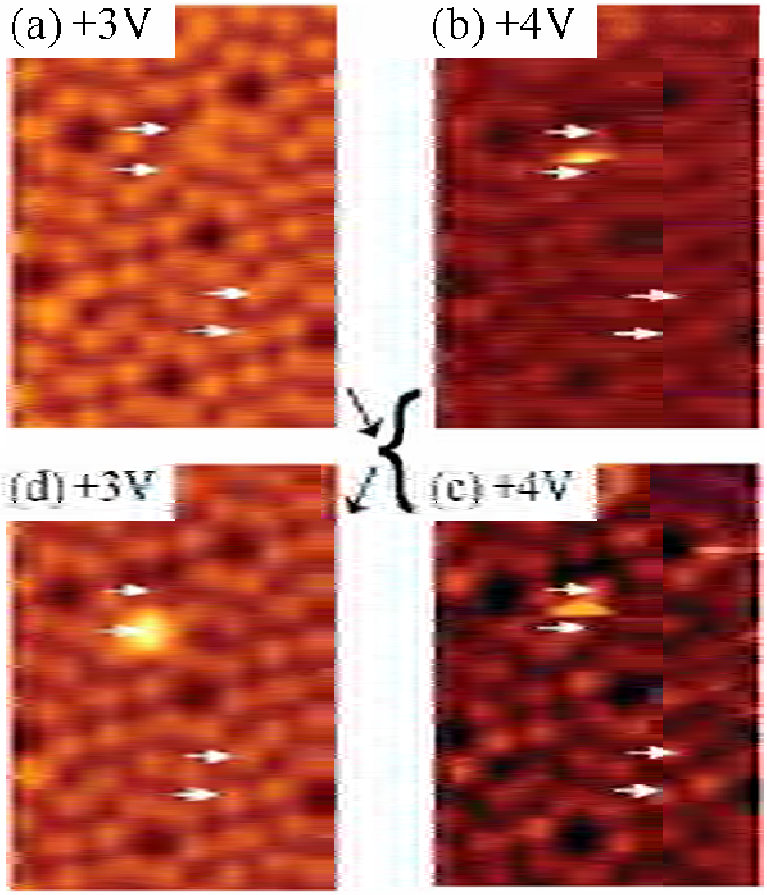

Figure 2.22 STM images taken during the C-Cl dissociation process from (a) to (d). White arrows on the top part of images indicate the original chlorobenzene binding site, while white arrows on the bottom part of images indicate the corresponding clean adatom site. (Images and caption modified from [61])

The dissociation process could not only be induced in one step by the STM for a given molecule, but also it could be induced progressively for the same molecule. In the experiment done by Baadji *et al.* [63], the Co-Salen molecule on the Cu(111) surface at 25 K was sequentially dehydrogenated by the STM. The Co-Salen molecule on the Cu(111) surface was imaged like an inverted heart with a protrusion in the middle where the hydrogen atom was located. After the pulse exceeding +1.5 V was applied to the molecule, the dehydrogenation process could happen, as shown in Fig. 2.23. By comparing STM images with simulated STM images, different dehydrogenated states of the Co-Salen molecule could be identified. As the dehydrogenation happened, the height of the protrusion decreased, as shown in Fig. 2.23 from

(1) to (2) and finally to (3).

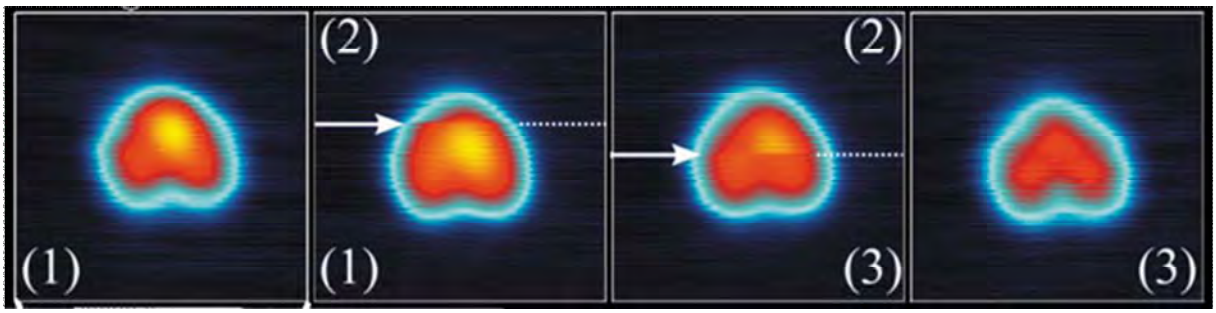

Figure 2.23 STM images show the sequential dehydrogenation manipulation process of a Co-Salen molecule. Intact, single-dehydrogenated and double-dehydrogenated states in the image are marked with (1), (2) and (3), respectively. (Images and caption modified from [63])

Other bond dissociation processes, such as C-H [64] and S-S [65] dissociation, were also reported, as well as mode specific dehydrogenation of propene molecules [66]. Dissociation of the $B_{10}H_{14}$ molecule on the Si(111)-7×7 surface [67] and dissociation of the D_2S on the Si(100) surface at low temperature [68] were also demonstrated.

Association

Since the dissociation process was possible, the association process was also achieved. As shown in Fig. 2.24, Hla *et al.* [69] performed an experiment of the iodobenzene molecule on Cu(111) at 20 K. The C-I bond inside the iodobenzene molecule was first dissociated and the phenyl molecule created, then by moving away the I atom and moving two phenyl molecules together, finally by inelastic tunnelling, a new biphenyl molecule was generated by association. This process also demonstrated that multiple types of motions could be induced for the same molecule. Other association processes were also performed, e.g., the gold atom formed bonds with the Pentacene molecule in different positions of the Pentacene molecule

by inelastic electron tunnelling on the NaCl bilayers on the Cu(100) surface [70], the Fe atom formed the bond with the CO molecule to generate the Fe(CO) molecule and sequentially formed the bond with another CO molecule to generate the $Fe(CO)_2$ molecule on the Ag(110) surface at 13 K [71].

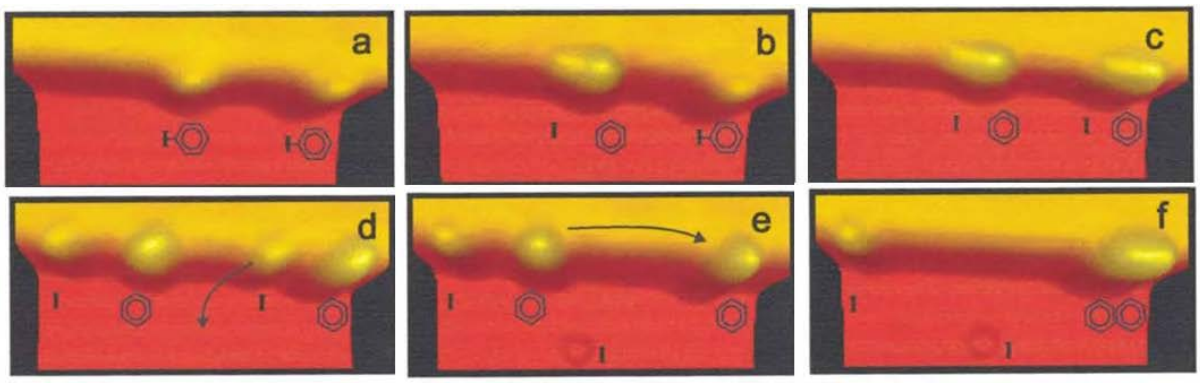

Figure 2.24 STM images showing the whole process of one biphenyl molecule created by two separate iodobenzene molecules from (a) to (f). (Images and caption modified from [69])

Combined manipulation

For the complicated molecules, besides several modes of lateral motions mentioned, the combined motion could be induced by STM. Four similar molecules, i.e., anthraquinone (AQ), pentaquinone (PQ), pentacenetetrone (PT) and dimethylpentacenetetrone (DPT) were investigated by Cheng *et al.* [72]. These molecules share same substrate linkers (carbonyl group) serving as legs, among which AQ is bipedal with only three rings, PQ is similar to AQ, but with extended aromatic backbone, PT is a quadrupedal and similar as PQ, and DPT is similar to PT, but with both ends having methyl groups. By plotting the diffusion rate against temperature, they identified a big difference between the bipedal species and quadrupedal species. Besides the effect from the "leg" numbers, the elongation and the methylation also made quite significant changes to the diffusion rate. Finally, through calculation, they

concluded that the diffusion motion of PT was a pacing mode, of which the two legs on each side moved together sequentially as indicated in Fig. 2.25.

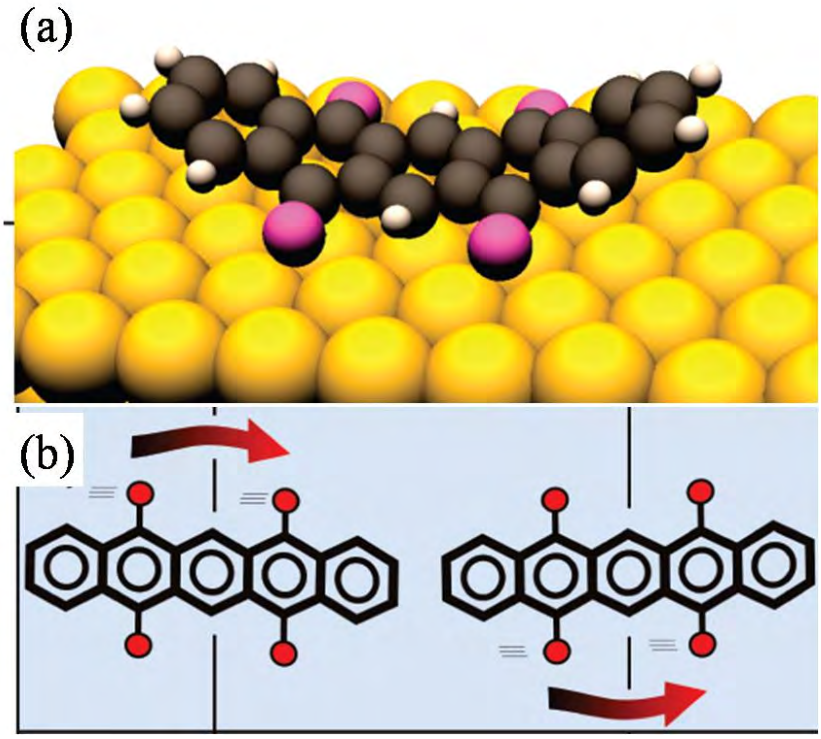

Figure 2.25 (a) A schematic diagram of the model of the PT molecule on the Cu(111) surface (b) A schematic diagram shows the pacing motion of the PT molecule. (Images and caption modified from [72])

Other applications

Since different motions could be induced by STM for different atoms and molecules, atoms and molecules could serve as basic building blocks on the surface for "bottom-up" construction. Different structures were made to study quantum properties, such as the Fe ring constructed by Crommie *et al.* [73], where the standing wave inside the ring could be clearly observed. A mirage atom in the centre of the ring was observed, even there was actually no atom inside, as shown in Fig. 2.26. Other fascinating structures were also constructed to study such effect [74].

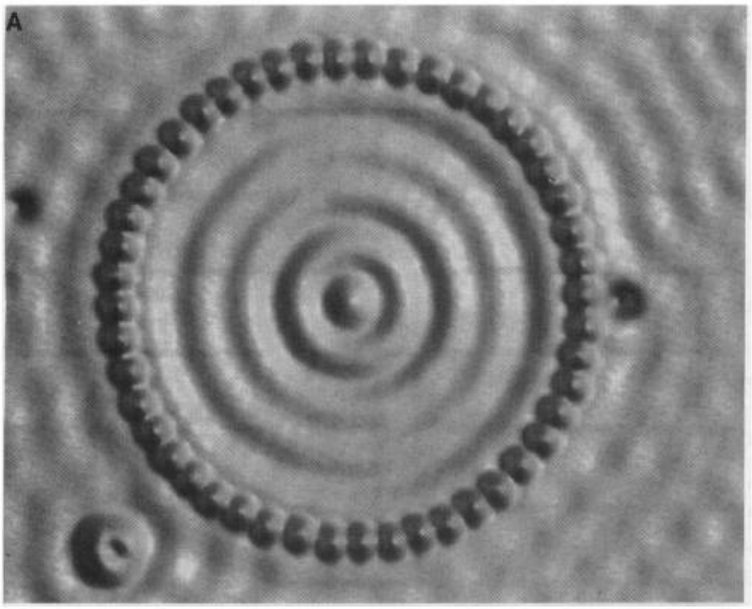

Figure 2.26 An STM image of 48 Fe atoms forming a ring on the Cu(111) surface. (Images and caption modified from [73])

Except for various manipulations performed by STM discussed above, other types of STM usage were realized, e.g., partial sequencing DNA by STM was done by Tanaka *et al.* [75]. By a special oblique pulse-injection method, single strand DNA (ssDNA) was deposited on the Cu (111) surface in a extended formation, aiding the subsequent sequencing. A characteristic peak (V_s = -1.6 V) over the guanine base was apparent in the STS. Thus by the STS imaging over the whole ssDNA, guanine bases were distinguished with small errors, as shown in Fig. 2.27.

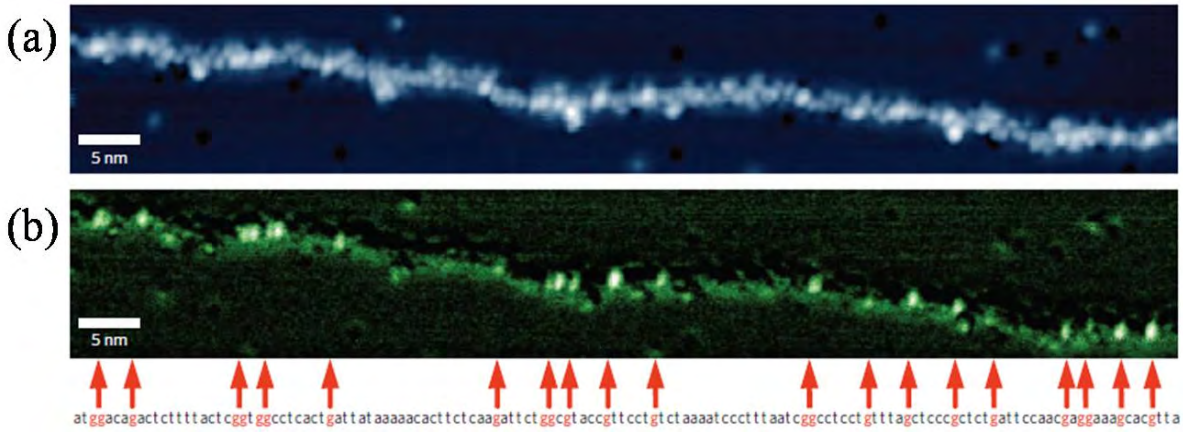

Figure 2.27 (a) An STM image of ssDNA. (b) A *dI/dV* map of (a), where red arrows indicate the position of guanine bases. (Images and caption modified from [75])

2.4 Summary

The principle for STM and AFM imaging followed by the principle of STS has been explained. Three main mechanisms of atomic manipulation have been described, including the manipulation induced by mechanical interaction, electric field and inelastic tunnelling. Applications of atomic manipulation have been categorized into several fields and selected examples have been introduced respectively.

Chapter 3 Experimental

In this chapter experimental equipments and methods are introduced. The Ultra-High Vacuum (UHV) STM system together with the experiment preparation procedure are described first. Then the benchtop SPM system with the experiment preparation procedure are described followed by the data analysis method.

3.1 UHV STM

3.1.1 STM

The UHV STM used for experiments is a UHV 400 Variable Temperature Ultra-High Vacuum Scanning Tunnelling Microscope built by RHK Technology. Normally, a STM is made up of following parts [76]:

1. The scanner and coarse approaching system. The scanner enables the tip to move in the X, Y and Z direction on the sample surface during the scanning. It is made of piezoelectric ceramics, that allow a voltage to be applied to induce the mechanical displacement (for example, the piezo drives P_x, P_y and P_z in Fig. 2.1). The coarse approaching system enables the tip to move towards the sample into the tunnelling range. There are several methods for coarse approach, such as screw, clamp-step and stick-slip. In our experiment, the STM head uses the stick-slip method and the control electronics type STM 400 and SPM 1000 from RHK Technology. Fig. 3.1 shows a photograph of our STM head sitting on the sample holder.

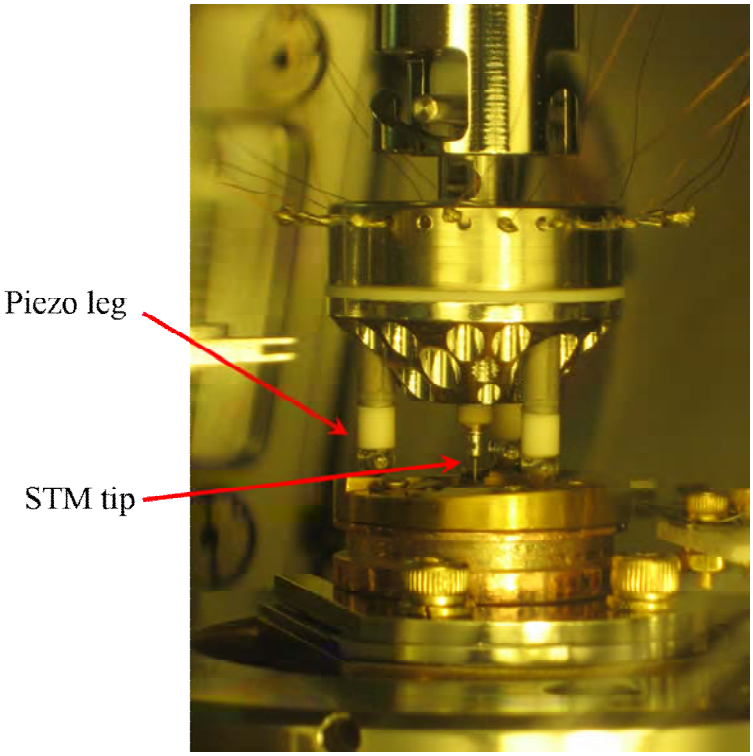

Figure 3.1 A picture of the STM head used in the experiment. Red arrows indicate the piezo leg and the STM scanning tube.

The STM as shown in Fig. 3.1, is made of four identical piezoelectric tubes. Three of them are placed 120 degrees apart with respect to each other and act as the "legs" of the scan head. These legs are used for the coarse approach, X and Y coarse motion as well as Z offset. The fourth tube located in the center of the scan head acts as the scanning tube.

2. The feedback system. The feedback system is designed to control the gap between the tip and the sample. In our system, this task is undertaken by the controlling electronics: type SPM 1000 from RHK Technology.

3. The computer system. The programme in the computer is used to control the movement of the tip, at the same time it receives data from the external electronics and subsequently converts the data into images shown on the screen. Program XPM 1000 provided by RHK Technology is used for above tasks.

4. The tip. More than one type of material can be used as the STM tip. For UHV conditions, rigid W wire is used. Due to an oxide layer forming on the surface of the W wire, it cannot be used directly and has to be processed before the experiment. In our experiment, an atomically sharp W tip was prepared as described in section 3.1.3.

5. The vibration isolation system. In order to get a clear image, unwanted changes of the gap between the tip and the sample should be reduced to less than ~0.01 Å [14]. However, floor vibrations and outside vibrations transmitted by air are much larger than that. As a result, vibration isolation system consisting of the high resonance-frequency component and the low resonance-frequency component should be used. In our case, for a better resolution of STM images, all experiments were performed in a laboratory located in the basement. Furthermore, an enclosed booth was in place for experiments in order to cut down the noise level from the open air. The sample holder rests on a sample stage that is supported by four springs. These springs with high resonance frequency act as a barrier against the transfer of the low frequency mechanical vibration to the sample. A 10-ton concrete block with low resonance-frequency, which is floating on 4 compressed air legs, holding the whole UHV system, further minimizes the high frequency vibration noise transferring to the STM.

Further measures were taken to decrease the noises of other sources to STM images. During the initial noise checking of the program, we found a 50 Hz noise in the signal. We found that this noise was from the power supply and the earth loop in the electronics. In order to avoid this, we used an isolation transformer to isolate the earth of the STM from the other apparatus, which significantly reduced the 50 Hz noise. To reduce the thermal drift of the sample relative to the STM head, the booth is air-conditioned to provide a constant temperature around 20 ℃. (In fact, by taking many STM images in sequence, over night, the thermal drift is still evident.

But this level of drift (~0.4 Å/s) is acceptable.

3.1.2 UHV

3.1.2.1 UHV system

Fig. 3.2 shows a block diagram of our UHV chamber, associated with pumping and measurement systems. With the aim of obtaining a better vacuum, two chambers (the main chamber and the preparation chamber) and a load-lock are set up in the system. Under such design, the dosing of PCB molecule and the purification testing with the mass spectrometer were performed in the preparation chamber. The tip annealing process was performed in the load-lock. Tips and samples were transferred to the load-lock first, then to the preparation chamber, and finally to the main chamber. Under these conditions, the main chamber retained relatively good ultra high vacuum which was crucial to our experiments. The pressure of the main chamber is maintained by an ion pump (Varian Diode 300) with a titanium sublimation pump (TSP) attached to it. The pressure of the main chamber monitored by the ion gauge attached is in the middle 10^{-11} torr range, which is sufficient to keep a clean surface intact for several days. The pressure of the preparation chamber is maintained by an ion pump (Varian Diode 150). The main turbo molecular pump (Pfeiffer) is used when the preparation chamber needs to be pumped down from the atmosphere. The pressure of the preparation chamber monitored by the ion gauge attached is normally in the upper 10^{-10} torr range. The load-lock and the roughing line are pumped down by a smaller turbo molecular pump (Pfeiffer)

connected to the load-lock and a rotary pump (Edwards RV 5 Dual-Mode Vacuum Pumps) connected to the roughing line. The pressure of the load-lock monitored by the penning gauge can reach the middle of 10^{-8} torr range after one or two days pumping. The pressure of the roughing line monitored by the pirani gauge can be pumped below 10^{-1} torr. Liquid samples can be stored in the test-tube, which can then be connected to the gas line through one of the three gas valves (V7-V9). In our experiment, the chlorobenzene molecule was stored in the test-tube, which is connected to the gas line through V7.

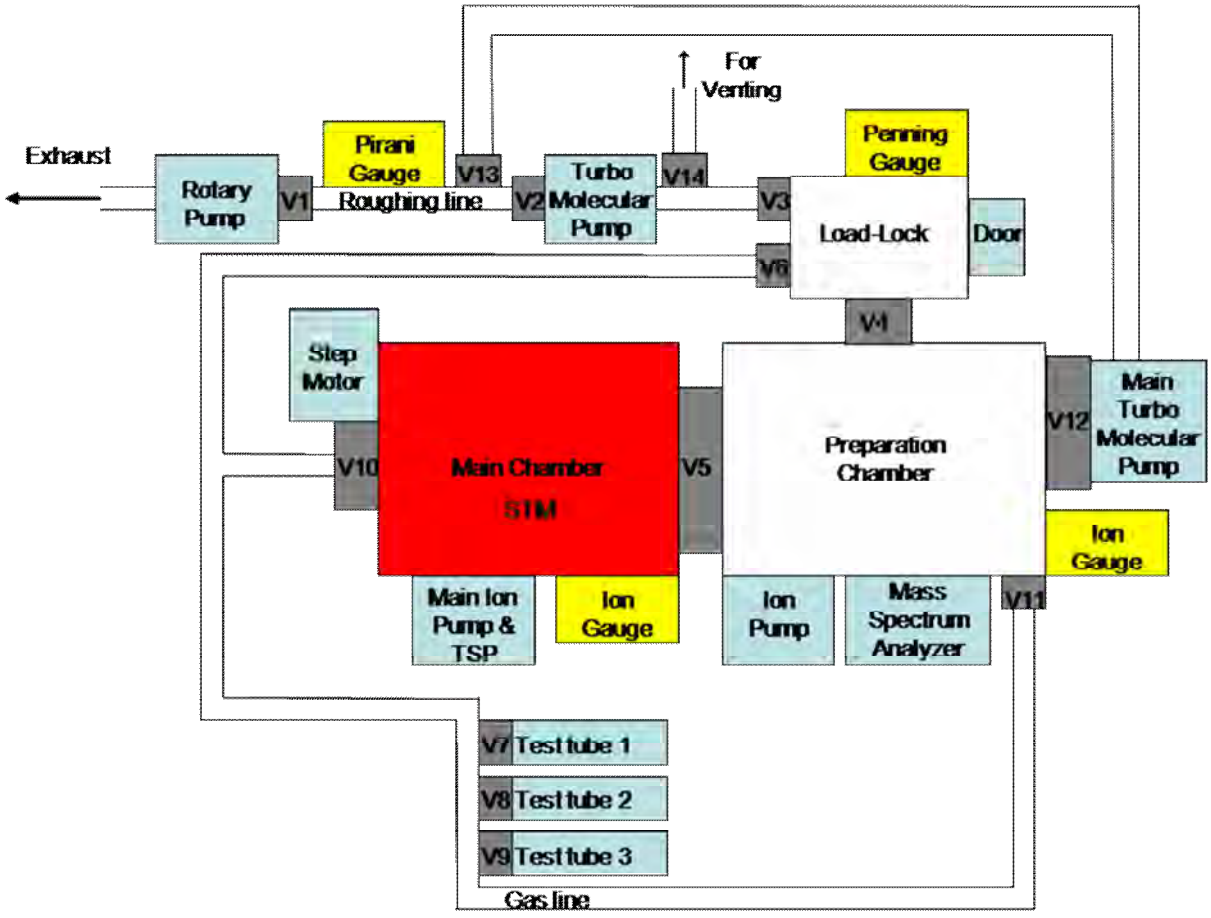

Figure 3.2 A block diagram of the UHV chamber, not to scale. V1-V14 in the block diagram stand for valves in the system.

3.1.2.2 Pumping

If the whole system is vented, pumping and baking is needed, the main chamber, the preparation chamber, the load-lock and the gas line need to be connected together, thus the three gate valves (V3, V4, V5, V12) and the gas valve (V6) have to be opened. To start with, the valve V1 can be opened and the roughing line can be pumped by the rotary pump. When the pressure in the roughing line drops below 10^{-1} torr, the valves (V13, V2) can be opened and the whole system is pumped by the rotary pump. When the pressure in the roughing line drops below 10^{-1} torr again, two turbo molecular pumps can be started and the penning gauge can be turned on after several minutes to monitor the pressure of the load-lock, the preparation chamber and the main chamber. Once the pressure monitored by the penning gauge drops below 10^{-7} torr, the two ion gauges can be turned on to monitor the pressure in the main chamber and the preparation chamber respectively. The main ion pump and the ion pump should not be started until the pressure in both chambers drops below 10^{-8} torr. Afterwards, the gate valves (V5, V4) can be shut. When the pressure of the preparation chamber drops to middle 10^{-10} torr range, the gate valve V12 and the valve V13 can be shut and the main turbo pump can be vented (the venting of the main turbo pump is independent from the other parts of the system). The pumping of the system is then complete. Furthermore, in order to perform STM experiments, the load-lock and the roughing line should be vented as described in section 3.1.2.4.

3.1.2.3 Baking

If the pressure of the main chamber cannot be pumped down to 10^{-10} torr range, baking is needed in order to get rid the contamination in the main chamber. To bake the whole system, 5 thermal isolation shields are needed to form a block on the UHV table together with some heating tapes attached to certain places of the system. The lamps attached to the thermal isolation shields will provide the heat during the baking. The heating tapes are wrapped around the system to provide additional heat during the baking, especially in locations where there are big stainless steel blocks, which are hard to bake to the high temperature, such as the big gate valves (V5 and V12), the base of the main chamber and the preparation chamber. The apparatuses which are not designed to be baked and the test-tubes have to be uninstalled before the baking starts. Also all the feedthroughs and the glass monitor porters need to be covered with aluminum foil, in order to prevent uneven temperature generating around these places, which might cause damage to them. The baking temperature should be above 100 ℃, in order to get rid of the water and other contaminants, but at the same time should not be higher than 125 ℃, which is restricted by STM, to prevent the piezoelectric tubes of the STM being depolarized. Thermocouples are attached to certain places, e.g., the base of the chamber and the preparation chamber, and the top of the main chamber of the UVH system, to monitor the temperatures during the baking. A programme written in Labview by Dr. Peter Sloan is used to control the power provided to lamps and heating tapes to ensure that the desired temperature for certain parts of the UVH system are achieved during the baking. The baking can take 2 days or more, depending on the pressure of the chambers. Once the pressure of the

main chamber drops to 10^{-10} torr range, the baking can be stopped. The system should be left to cool down naturally for several hours before the thermal isolation shields are disassembled. Once the temperature of the system returns to the booth temperature, the baking of the system is complete.

3.1.2.4 Venting

The venting of the UVH system is all done through the load-lock by the valve (V14) using nitrogen gas. Thus the part of the system to be vented has to be connected to the load-lock. Before venting, the roughing line and the load-lock need to be pumped first, then all the monitors and pumps of desired venting parts, which can only work at high vacuum, need to be turned off, e.g., the main ion pump, the ion pump, two ion gauges and the penning gauge. Valves (V1 and V2) have to be shut before the rotary pump can be shut to avoid the probability of oil contaminating the other parts of the system through the roughing line during the venting process. Afterwards, the turbo molecular pump connected to the load-lock can be turned off. The leaking valve should not be opened too early (which can be judged by the sound from the turbo fan), before the turbo fan slows down, otherwise the rapid stop to the turbo fan caused by nitrogen gas will shorten the lifetime of the turbo molecular pump. Nitrogen gas is provided through a silicon tube connected to the leaking valve V14. By listening to the sound generated by the turbo fan, the leaking valve V14 can be opened slowly. Once the turbo fan is completely stopped, the leaking valve V14 can be opened fully to ensure that the nitrogen gas fills the desired venting parts of the system, the venting of the system is

then complete.

3.1.2.5 Sample and tip transfer

The transfer of the sample holder or the tip holder is done first by transferring to the load-lock, then to the preparation chamber, and finally to the main chamber. The sample holder, the tip holder, the fork in the transfer arm and the wobble stick used in this process are shown in Fig. 3.3. There are two trenches in the outer area of the sample holder and the tip holder that can be "caught" by the fork in the transfer arm, the wobble stick and the STM sample stage. By "catching" the sample holder or the tip holder in the trenches, the sample holder or the tip holder can be passed by the transfer arm from the load-lock to the main chamber and finally be slid into the STM sample stage and fastened there. The transfer procedure for the sample holder or the tip holder into the UHV system is the same. In order to transfer the sample holder or the tip holder into the UHV system, the load-lock needs to be vented by nitrogen gas following the procedure as described above. The door installed on the load-lock can be opened and the sample holder or the tip holder held by special pliers can be passed into the load-lock and "caught" by the fork of the transfer arm at the lower trench. The door can then be closed and the load-lock pumped. After the pressure in the load-lock drops to $\sim 1\times10^{-6}$ mbar, the gate valve V4 can be opened and the sample holder or the tip holder can be transferred into the preparation chamber by the transfer arm and "caught" by the fork of the other transfer arm in the preparation chamber. When this is done, the transfer arm in the load-lock can be retreated to the load-lock and the gate valve V4 can be shut. Afterwards, the gate valve V5

can be opened and the sample holder or the tip holder can be transferred into the main chamber by the transfer arm and "caught" by the wobble stick. When this is done, the transfer arm can be returned to the preparation chamber and the gate valve V5 can be shut. During this process, the STM sample stage should be maintained at its lowest position, otherwise there will not be enough space. Once it is done, the STM sample stage should be lifted to the highest position so the sample holder or the tip holder can be slid into the STM stage and fastened, or alternatively they can be stored in the shelf in the main chamber for future use.

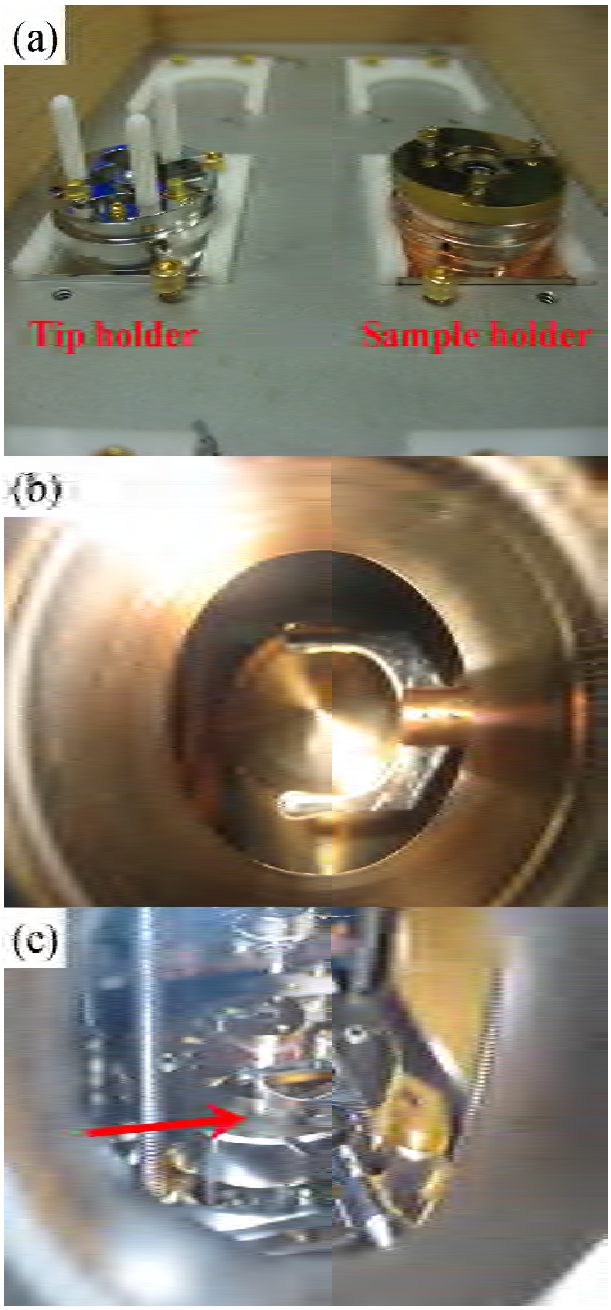

Figure 3.3 (a) The sample holder and the tip holder. (b) The fork in the transfer arm and (c) the wobble stick used in the UHV system. The red arrow indicates the wobble stick.

If a new tip needs to be installed, then the tip holder containing a new tip should be slid into the STM sample stage and fastened. The STM head should be lowered carefully and slowly towards the STM sample stage. There are three holes located between the three piezoelectric tubes in the STM head. The structure of the tip holder is similar but with three piezoelectric tubes replaced by three PVC legs; once the tip holder is fastened into the STM sample stage,

these legs are positioned towards the corresponding holes on the other side, such that when the STM head is lowered, the legs match to the holes. Once the STM head is lowered to the desired position, the tip can be inserted into the center of the center piezoelectric tube. Then the metal wire on the tip holder, which is used to fix the tip, can be released by the wobble stick. After this, the STM head can be retreated to the top position again and the tip holder can be transferred out of the STM sample stage using the wobble stick. The tip transfer process is then complete.

3.1.3 Tip preparation

A sharp STM tip is required in order to get a high resolution STM image, since the resolution of an STM image depends on the radius of the tip. Two main processes need to be done to generate a sharp tip for the experiment. The first is chemical etching in NaOH solution and the second is tip heating in the UHV system.

For the chemical etching process, 2 M NaOH solution, an Omicron tip etching control unit and a homemade tip etching system is used. The Omicron tip etching control unit controls the differential cut-off process. The W wire used in the experiment was purchased from Advent (tungsten wires, 99.95% purity, 0.25 mm diameter). The wire will be cleaned and then cut into shorter wires using metal pliers. Two differential cut-off processes are needed, one to remove the cracked part at the end of the W wire, generated by the mechanical cutting, and a second to produce the actual tip. The etching parameters must be well adjusted [77] such that the aspect ratio is around one and the tip is cylindrically symmetric and sharp. The aspect ratio of

the tip should not be too high, otherwise mechanical vibrations will be caused and generate noise for the STM imaging. After the tip is produced, it needs to be cleaned. A tip generated by this method is shown in Fig. 3.4. The diameter of the tip is ~100 nm.

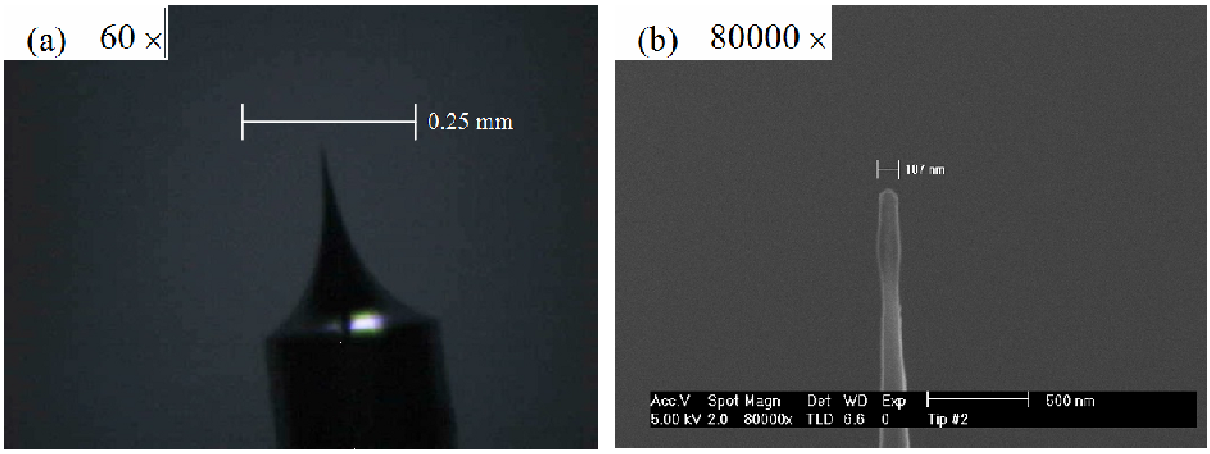

Figure 3.4 Tip images from an optical microscope (left) and an SEM (right) (taken by Dr. Jedsada Manyam). The top end of the tip measures ~60-100 nm across.

For the tip heating process, the tip is mounted on a modified ion gauge and then installed to the load-lock. A DC power is then applied through the feedthrough to heat the tip resistively. To do this, the load-lock needs to be pumped down to 10^{-6} range, then the tip is heated for 2 seconds at 6.4 A (~1300 K), then for a further 5 minutes at 3 A and finally cooled down for 10 minutes [78]. This procedure removes the oxide layer around the tip and the load-lock is vented and the tip can then be transferred to the tip holder for future use.

3.1.4 Surface preparation

Silicon samples are cut from n-type (phosphorus doped) single crystal wafers 0.38 mm thick

with a resistivity between 1 and 30 Ω cm purchased from Goodfellow company. For non-local desorption experiments on the stepped surface, silicon samples are cut from n-type (phosphorus doped) single crystal wafers 0.356-0.406 mm thick with a resistivity between 1 and 100 Ω cm and off orientation $0.5^{o} \pm 0.5^{o}$ purchased from Cemat Silicon SA company. For the temperature dependent non-local desorption experiments, silicon samples are cut from p-type (boron doped) single crystal wafers 0.5-0.55 mm thick with a resistivity between 0.01 and 0.02 Ω cm purchased from Siltronix company. A small piece (2 mm × 10 mm) of silicon sample cut from the silicon wafer using a diamond knife is mounted into the sample holder. Before transferring to the load-lock, surface dust on the sample and sample holder is removed using N_2 gas. Once in the main chamber the sample are degassed at 700 ℃ first for half a day to get rid of the water and oil on the surface. Afterwards the samples are repeatedly flashed at ~1300 ℃ (950 ℃ for the temperature dependent non-local desorption experiments, lower temperature in order to reduce the defect on the surface due to the boron appearance to the surface) for 10 seconds and cooling for 10 minutes until the pressure in the main chamber drops below 2×10^{-10} torr. The final step in surface preparation is the reconstruction process consisting of a flashing again at 1300 ℃ (950 ℃ for the temperature dependent non-local desorption experiments) for 5 seconds, followed by a rapid cooling down to 950 ℃ and then slow cooling (1 ℃/s) down to room temperature. A well reconstructed near defect-free (<0.97%) Si(111)-7×7 surface achieved after this process is shown in Fig. 3.5. For the temperature dependent non-local desorption experiments, due to the small size of boron atoms, the defect on the reconstructed surface was ~10%.

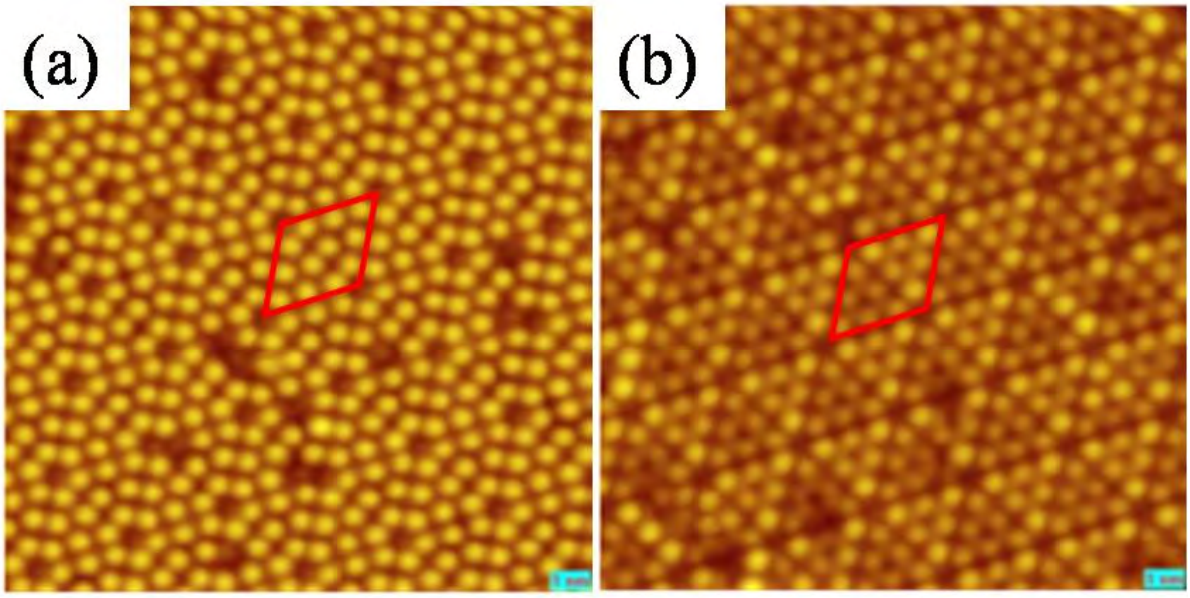

Figure 3.5 STM images of the Si(111)-7×7 surface with one unit cell in red rectangle. (a) An STM image taken at positive bias voltage (+1.0 V, 103 pA, 150 Å × 150 Å). (b) An STM image taken at negative bias voltage (-1.0 V, 103 pA, 150 Å × 150 Å).

3.1.5 Sample preparation

3.1.5.1 Chlorobenzene dosing

The chlorobenzene used in this experiment was purchased from Sigma-Aldrich company. Around 10 ml chlorobenzene liquid is extracted and put into the test tube by the pipette. The test tube is then installed to the gas line through the gas valve V7. Before depositing onto the silicon surface the chlorobenzene sample needs to be cleaned, using the "freeze-pump-thaw" method, and checked using the mass spectrometer. The turbo molecular pump connected to the load-lock is used to perform the "freeze-pump-thaw" procedure. First, the load-lock needs to be pumped down following the procedure described in section 3.1.2.2. When the pressure in the load-lock drops to ~10^{-6} mbar gas valve V6 can be opened slowly to pump down the

gas-line until the pressure in the load-lock drops back to ~10^{-6} mbar again. Afterwards, liquid nitrogen is used to freeze the chlorobenzene in the test tube. Initially, some bubbles containing the contamination gas may be observed trapped in the chlorobenzene solid. Once the chlorobenzene is completely frozen the gas valve V7 can be opened slowly to let the turbo molecular pump pump away the contamination gas that was not trapped into the chlorobenzene solid. Then, by tap water, the chlorobenzene solid can be thawed. The gas valves V7 can be closed after the chlorobenzene solid is thawed thoroughly, in order not to pump away too much chlorobenzene gas. This is a cycle of the "freeze-pump-thaw". These cycles need to be repeated until no bubbles of contamination gas can be seen. After the purification of the chlorobenzene liquid using the "freeze-pump-thaw" method, the purity of the chlorobenzene liquid can be tested by the mass pectrometer. V6 can be closed and V7 opened for a while to fill the gas line with chlorobenzene gas. Then V5 can be opened to take the mass spectra of chlorobezene gas to compare with mass spectra data. Once this is done, V5 can be closed and V7 can be opened for a while again to fill the gas line with chlorobenzene gas. Then chlorobenzene gas in the gas-line is ready for the deposition. The deposition of chlorobenzene gas on the silicon surface in the main chamber is done by the step motor attached to the leak valve on the main chamber, which can be controlled by the programme written in Labview by Dr. Peter Sloan. During experiments, different desired amounts of chlorobenzene were introduced to the Si(111)-7×7 surface, while the maximum deposition pressure was maintained below 5×10^{-8} torr in order not to contaminate the main chamber.

3.1.5.2 PCB dosing

Due to the low vapour pressure of the PCB molecules at room temperature, similar gas line dosing for the chlorobenzene is not applicable to the PCB molecule, thus a NATC (near ambient-temperature effusion cell) together with a compatible control thermostat CCx-304B vpc is used for the PCB molecule deposition. The PCB used in this experiment is PCB No. 15 purchased from Sigma-Aldrich company. Around 100 mg PCB powder is put into the tube of the NATC (near ambient-temperature effusion cell) and then the NATC system is installed to the UHV system through the load-lock, as shown in Fig. 3.6. In order to install the NATC, the load-lock needs to be vented and the transfer arm originally connected to the load-lock needs to be uninstalled. Before the first time PCB deposition, new PCB powder needs to be cleaned using the following procedure. First the load-lock needs to be pumped down, following the procedure described previously. Then both the load-lock and the NATC needs to be baked at 70-90 ℃ for 2-3 hours, followed by natural cooling to room temperature. The baking should not be too long, or at too high temperature, otherwise all the PCB molecules in the tube may be evaporated. After baking the NATC, the PCB should be more purified and ready for the deposition. We tried to check the purification of the PCB molecules by the mass spectrometer in the preparation chamber, however, only very weak corresponding signals were detected. This might be due to the miss align of the mass spectrometer to the opening of the tube of the NATC in the load-lock. When the hot PCB molecule is evaporated from the tube of the NATC, most of them stick to the cold stainless steel preparation chamber.

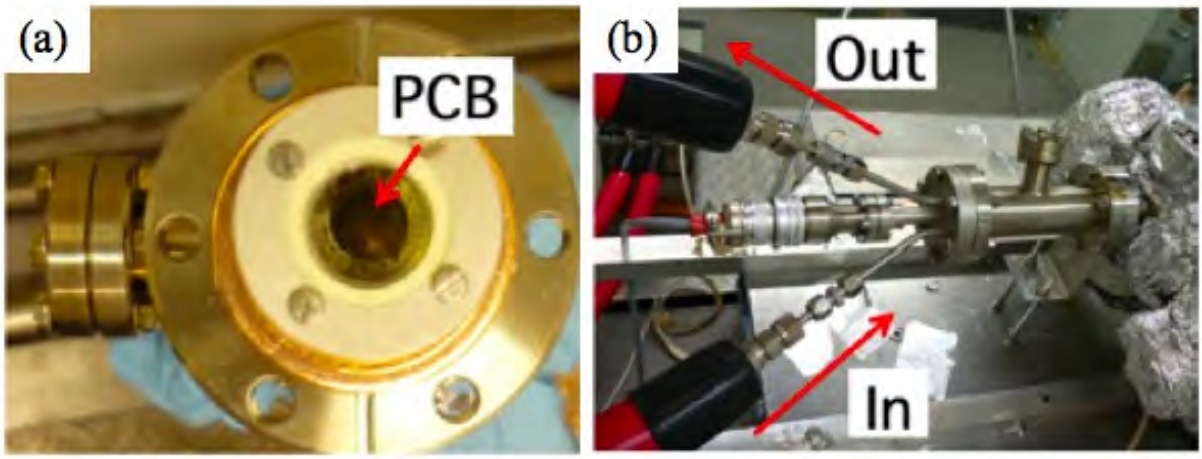

Figure 3.6 (a) The tube of the NATC. (b) NATC connected to the load-lock. (Image from [79])

For PCB deposition, the temperature of the NATC only needs to be increased to ~50 ℃, then the sample holder with the silicon sample can be transferred from the STM main chamber to the preparation chamber and faced to the opening of the NATC tube in the load-lock. The leak valve between the load-lock and the preparation chamber can be gradually opened to let the pressure of the preparation chamber increased to ~5×10^{-9} torr for 2~3 s to finish the PCB deposition, then the silicon sample can be transferred back to the STM chamber. In order to achieve a desired deposition density, different deposition parameters were tested by Dr. Sumet Sakulsermsuk through trial and error. Generally, a dose of 0.015 L at ~5×10^{-9} torr for 2~3 s was found to produce a coverage of less than 0.8 PCB molecules per Si(111)-7×7 unit cell, which is considered sufficient for the experiments.

3.2 Benchtop SPM

3.2.1 Benchtop STM

The benchtop STM used for the experiments is from Digital Instruments (NanoScope III STM). The mechanism of the STM working in ambient condition is the same as that in the UHV condition and is as described in section 3.1.1. The benchtop STM is made up of the following parts

1. The scanner and coarse approaching system. As shown in Fig. 3.7 (a), the piezoelectric tube at the center of the STM head (indicated by the blue arrow) is used for moving the tip in the X, Y and Z direction on the sample surface during scanning. The STM tip is inserted into the smallholding tube, which is attached to the piezoelectric tube (indicated by the red arrow). For the experiment, the STM head is placed on top of the STM stage, supported by three screws. Two screws, indicated by the red arrow in Fig. 3.7 (b), can be adjusted manually to lower the STM tip towards the sample for coarse approach. During the coarse approach, a commercial optical microscope is used to monitor the gap between the STM tip and the sample; when the gap is relatively small, the auto approach can be started. By controlling the step motor installed to the third screw (indicated by the blue arrow), the third screw can be lifted, thus the tip on the other side of the STM head can be brought closer to the surface until it reaches tunnelling range. The sample can be clamped by the wire on the STM stage, which also provides electric connection.

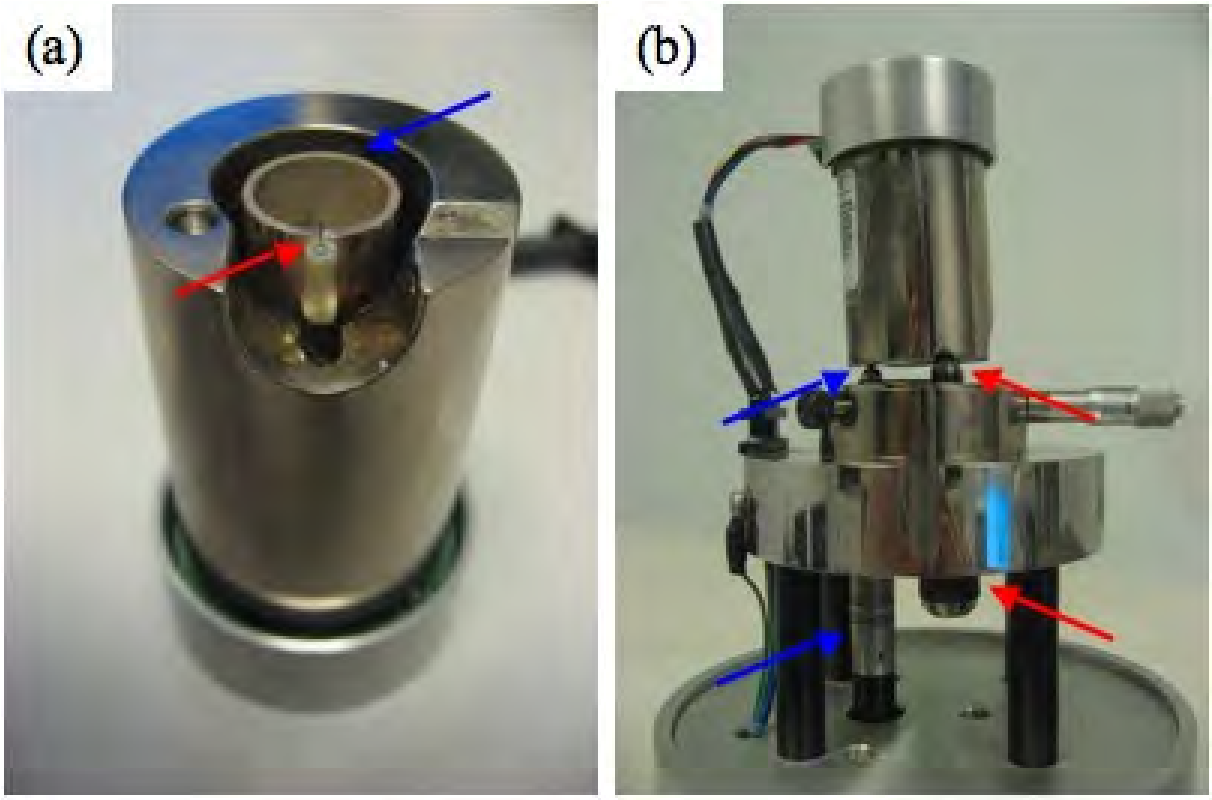

Figure 3.7 (a) The picture of the STM head of the benchtop STM system. The red arrow indicates the tip position and the blue arrow indicates the piezoelectric tube. (b) The picture of the benchtop STM stage with the STM head. The red arrows indicate the two screws for coarse approaching and the blue arrows indicate the screw driven by the step motor for auto approaching.

2. The feedback system. The controlling electronics for the benchtop STM is: the NanoScope IIIa SPM controller from Digital Instruments company.

3. The computer system. The programme used for data acquisition and analysis is Nanoscope STM from Digital Instruments company.

4. The tip. The Pt/Ir tip cut from Pt90/Ir10 wire from Advent is used in the benthtop STM system, owing to its easy production procedure and inert property in the ambient condition. Unlike the W tip used in the UHV condition, the Pt/Ir tip is prepared by mechanical cutting done using metal pliers. The pliers need to be positioned nearly parallel to the Pt/Ir wire and dragged away from the Pt/Ir wire during the cutting process in order to produce a relatively

sharp tip. If the tip needs to be modified during the scanning this can be achieved by crashing it intentionally onto the surface, or to the step edge, by faster scanning or suddenly changing of the gain. The tip should be cut to ~8 mm and should be slightly bent in the middle part of the wire before being inserted into the small holding tube to ensure attachment; loose attachment may result in more noise.

5. The vibration isolation system. The whole benchtop STM is supported by a vibration isolation base, while the whole benchtop STM is placed on an AFM platform, supported by the compressed air legs to further reduce the vibration level.

3.2.2 Benchtop AFM

The benchtop AFM used for the experiments is a Dimension 3100 built by Digital Instruments company. As discussed before, the mechanism of the AFM is comparable to the STM and AFM comprises following parts:

1. The scanner and the coarse approach system. As shown in Fig. 3.8 (a), the piezoelectric tube is used for moving the AFM tip in the X, Y and Z direction on the sample surface during the scanning. As shown in Fig. 3.8 (b), the AFM tip is first installed in the tip holder (indicated by red arrow), and then the tip holder is installed on the piezoelectric tube. Another special tip holder (indicated by blue arrow) with a plastic skirt are used for the experiment in the liquid state. The plastic skirt needs to be put on to protect the AFM head from short circuiting by the liquid during the measurement. The step motor attached to the AFM head can be controlled using the programme for both the coarse approach and the auto approach.

For measurements in the liquid state, 15 ml buffer solution needs to be applied to the AFM tip by pipette, before lowering the AFM tip into the sample droplet on the HOPG surface, in order to avoid getting a bubble trapped between the AFM tip and the tip holder when the tip meets the sample droplet. If a bubble does form, the laser beam will be deflected by the bubble and the approach procedure cannot be completed.

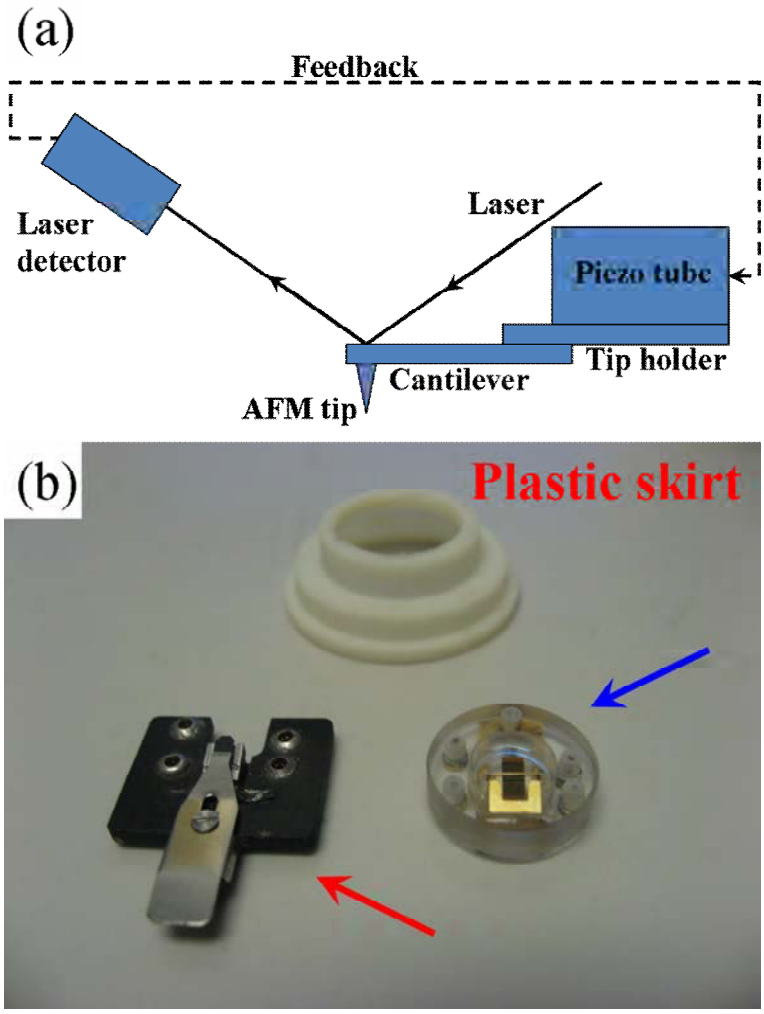

Figure 3.8 (a) Schematic picture of the AFM head of the benchtop AFM (not to scale). (b) Two types of tip holder for the AFM experiments. The one used in the dehydrated (liquid) state is pointed by the red (blue) arrow together with the plastic skirt used in the liquid state experiment.

2. The deflection system and the feedback system. A laser beam is generated on top of the

hollow piezoelectric tube. The laser beam passing through the hollow piezoelectric tube is reflected by the back side of the AFM cantilever, then by the reflecting mirror on the side and finally travels to the laser detector in the AFM head. AFM monitors the deflection of the tip to maintain the constant force. The controlling electronics for the benchtop AFM is NanoScope IIIa SPM controller together with NanoScope Dimension 3100 controller from Digital Instrument company.

3. The computer system. The programme used for data acquisition and analysis is Nanoscope 5.12r4 provided from Digital Instrument company.

4. The tip. The AFM tip used in the experiment for contact mode imaging was purchased from Veeco (Model MSCT). The AFM tip used in the experiment in tapping mode imaging was purchased from Vista probes (T300R). Two types of tip holders were used in the experiments, as shown in Fig. 3.8 (b). The tip holder indicated by the red arrow was used for measurements performed in the dehydrated state and the tip holder indicated by the blue arrow was used for measurements performed in the liquid state. The AFM tip is clamped to the tip holder, the crystal beneath the AFM tip can oscillate the tip for tapping mode imaging. The second tip holder indicated by the blue arrow was used for measurements performed in the liquid state.

5. The vibration isolation system. The AFM platform is supported by compressed air legs, which provide vibration isolation.

3.2.3 Surface preparation

3.2.3.1 HOPG surface

The HOPG surfaces used in this experiment were purchased from Momentive (10×10×2 mm). The HOPG block was cut into smaller pieces (10×5×1 mm). Each time one piece was used, a new fresh surface needed to be cleaved before the mucin experiment and the Au cluster decoration process. The cleaving process was quite simple and done using the magic tape from Scotch company. A new piece of magic tape was applied to the HOPG surface smoothly and carefully; to ensure the tape was fully attached, some pressing on top of the tape might be desired. The magic tape could then be removed from the HOPG surface smoothly and carefully, exposing the fresh HOPG surface. This process could be repeated until the shining HOPG surface without broken pieces of HOPG on top was achieved.

3.2.3.2 Au cluster decorated HOPG surface

Two types of size-selected Au_{55} cluster-decorated HOPG surface were used in this experiment; one was with 150 nm mean distance between the clusters and the other was with 110 nm mean distance between the clusters. These gold cluster decorated HOPG surfaces were prepared by Dr. Feng Yin. After a new fresh HOPG surface was prepared using the cleaving method described above, they were transferred to the cluster source to produce the size-selected Au_{55} cluster-decorated HOPG surface. The deposition energy of the Au_{55} cluster was

23 eV/atom, which was enough to pin the Au_{55} clusters on the HOPG [80] against the STM scanning.

3.2.4 Sample preparation

The mucin sample used in this experiment was purchased from Sigma-Aldrich: Mucin from porcine stomach, Type II (M2378). The mucin was purchased as a dehydrated, slightly yellow powder. The HEPES ((4-(2-Hydroxyethyl)piperazine-1-ethanesulfonic acid) buffer solution used in this experiment was purchased from Sigma-Aldrich (HEPES solution 1 M, pH 7.0-7.6). The ultra pure water used in these experiments was prepared within our group. In the beginning of every week, by diluting the mucin powder and (or) the HEPES buffer solution with the ultra pure water, different new stock solutions were prepared. By mixing different stock solutions with each other, or with ultra pure water, on parafilm pieces, desired concentrations of mucin samples for the experiments were produced. One such solution comprised mucin concentration of 0.2 mg/ml and HEPES concentration of 10 mM, one was with HEPES concentration of 10 mM and the other one was with mucin concentration of 0.2 mg/ml. These stock solutions were stored in the refrigerator at 4 ℃. Prior to each experiment, certain amounts of the corresponding stock solution were extracted by the pipette from the stock solution and put onto a fresh piece of parafilm.

3.3 Data analysis procedure

3.3.1 STS data analysis procedure

The main Matlab programme used for generating the STS data is written by Dr. Peter Sloan. As mentioned previously, in order to generate the $(dI/dV)/\overline{(I/V)}$ spectra, variable-gap *I-V* spectra were processed using standard techniques [10, 81]. The tunnelling current was measured, while tip-sample separation was changed with respect to the changing of the bias voltage. In the standard variable separation STS, a modulation technique (for example, a lock-in amplifier) is applied to acquire the *dI/dV* curve and afterwards be derived by the synchronically acquired $\overline{(I/V)}$ curve. However, the time spent on acquiring the *dI/dV* curve by using the lock-in amplifier was too long, the target molecule usually desorbed even during a single measurement. Consequently, instead of generating the *dI/dV* curve by a lock-in amplifier, numerical differentiation of *dI/dV* from the *I-V* curve was performed. Details of the whole process are illustrated below.

First, a symmetric V-shape z-ramp was used (typically approaching the tip by 1.3 Å per 1 V decrease in the bias voltage) to amplify the current signal in the band-gap region. Each *I-V* spectrum typically spanned from +2.5 V to -1.7 V with 5 mV voltage steps. After the variable-gap *I-V* data was acquired, each *I-V* spectrum was first corrected for the offset at zero voltage. Fig. 3.9 (a) shows the *z-V* curve during ramping. Fig. 3.9 (b) shows the raw variable-gap *I-V* spectrum.

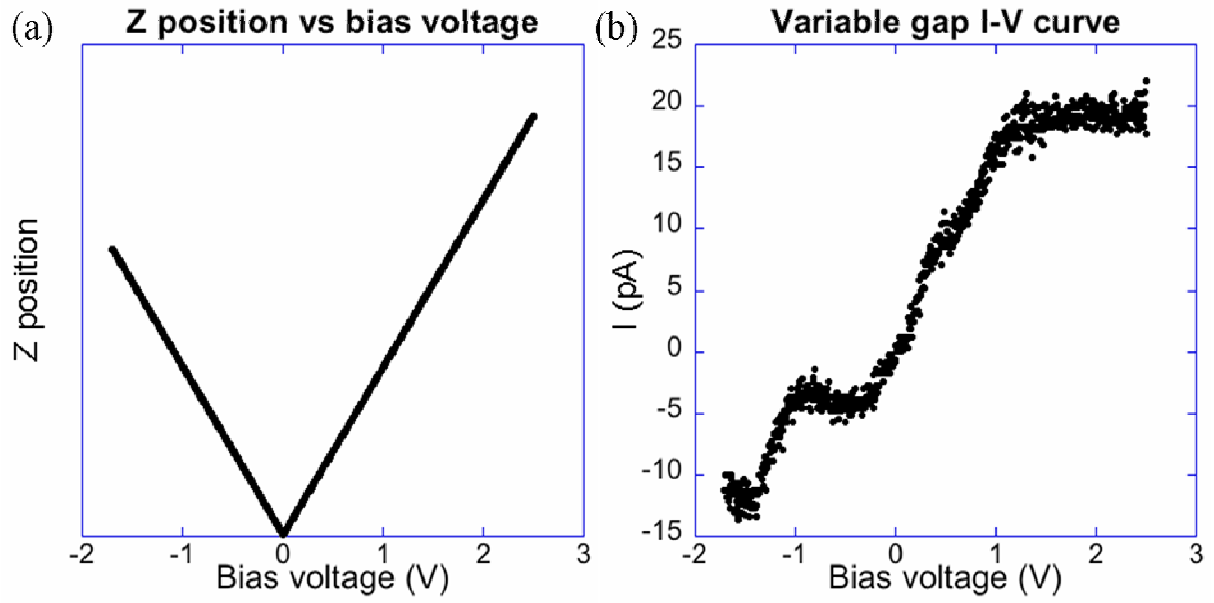

Figure 3.9 (a) *z*-*V* curve shows the *z* position versus the bias voltage during the *V*-shape gap ramping, while acquiring the spectrum. (b) Raw data of the variable-gap *I*-*V* curve.

Then each variable-gap *I*-*V* spectrum was converted to constant gap by the way of the exponential dependence of I on z, $I(z) = I(z_0)e^{-2\kappa(z-z_0)}$, with decay constants κ of 1 $Å^{-1}$ (as mentioned in section 2.1.1.2). Fig. 3.10 (a) shows the converted *I*-*V* curves in different κ. Afterwards, the converted constant gap *I*-*V* spectrum was smoothed using a function "sgolayfilt" (which contains the "Savitzky-Golay filter", the same as the smooth sub-function in the differential function) to allow the $\overline{(I/V)}$ to be generated. A linear regression model was used in this function with a 505 mV sliding window. Fig. 3.10 (b) shows the *I*-*V* curves using different size smooth windows in the smooth function.

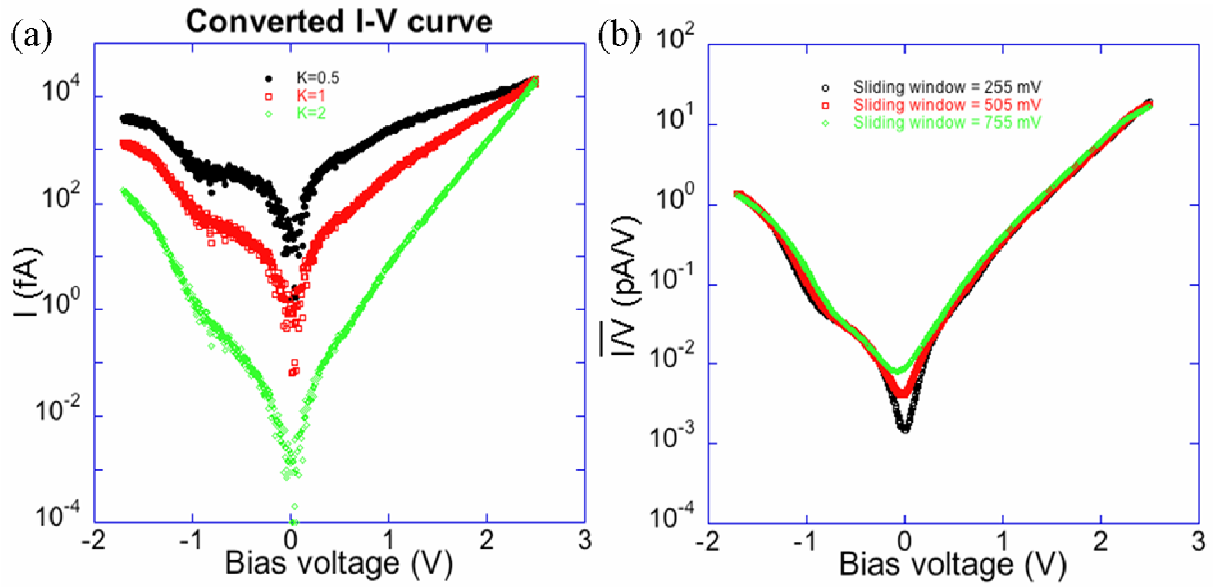

Figure 3.10 (a) Converted *I-V* spectrums using different κ. Black dots stand for $\kappa = 0.5$, red dots stand for $\kappa = 1$ and green dots stand for $\kappa = 2$. (b) *I-V* curves using different size sliding windows in the smooth function. Black dots stand for the sliding window equals 255 mV, red dots stand for the sliding window equals 505 mV and green dots stand for the sliding window equals 755 mV.

Meanwhile, a differential function "movingslope" is used to compute the differential *dI/dV* from the converted constant gap *I-V* spectrum. A "Savitzky-Golay filter" smooth sub-function using the linear regression model was performed in this differential function with a 250 mV sliding window. Fig. 3.11 shows a series of *dI/dV* curves obtained using different orders of the fitting polynomial, 1st order, 2nd order and 3rd order with different sliding windows 75, 250 and 500 mV.

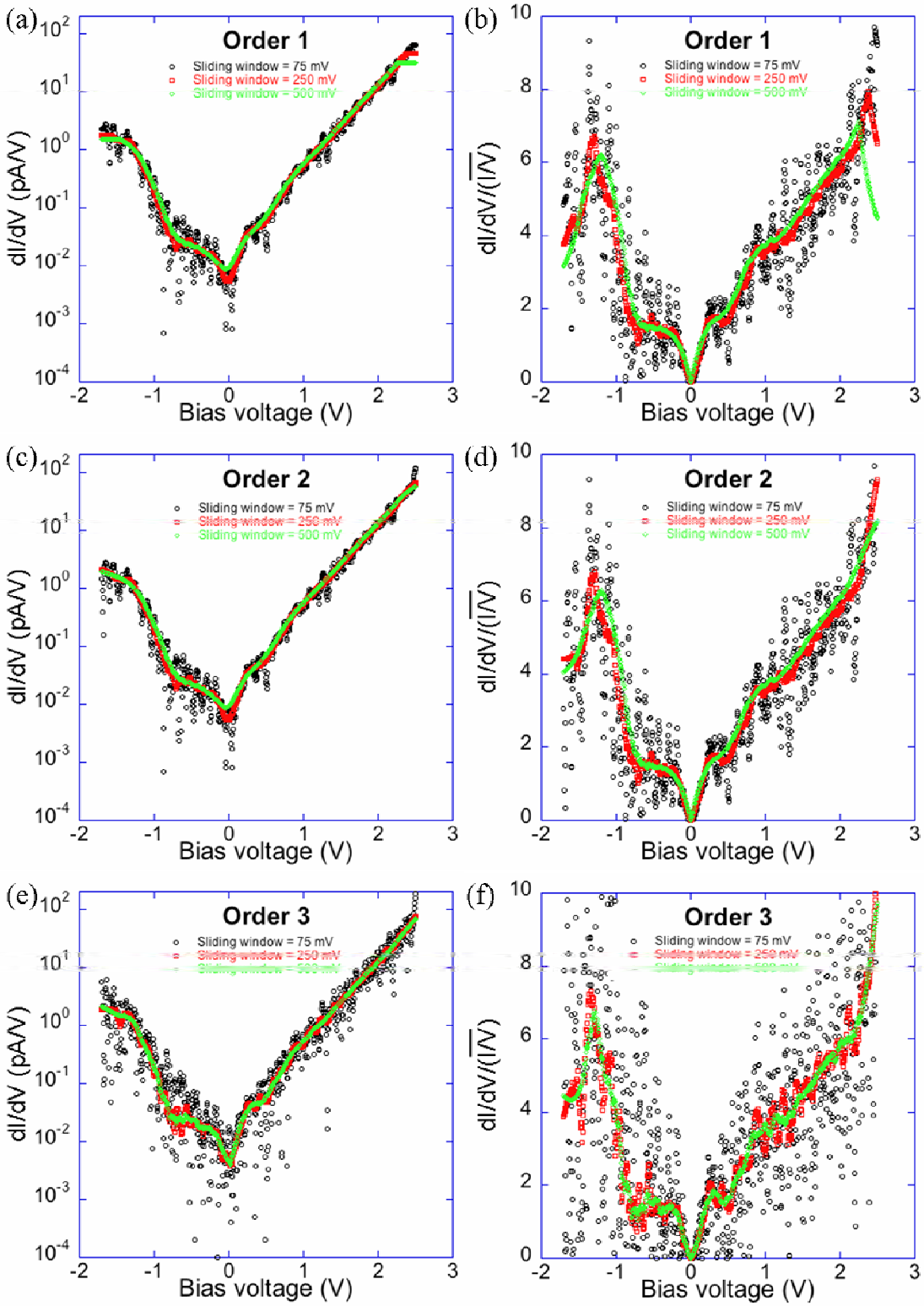

Figure 3.11 *dI/dV* curves using different size sliding windows and different regression models in the differential function, (a) for linear, (c) for quadratic and (e) for cubic; the resulting $(dI/dV)/\overline{(I/V)}$ curves using different size sliding windows and different regression models in the differential function, (b) for linear, (d) for quadratic and (f) for cubic. Black dots stand for the sliding window equals 75 mV, red dots stand for the sliding window equals 250 mV and green dots stand for the sliding window equals 500 mV

Thus, the $(dI/dV)/\overline{(I/V)}$ spectra was generated by dividing the *dI/dV* over the $\overline{(I/V)}$. Finally, multiple sets of $(dI/dV)/\overline{(I/V)}$ taken over different molecules were averaged together to generate the final spectra presented in this paper, as shown in Fig. 3.12.

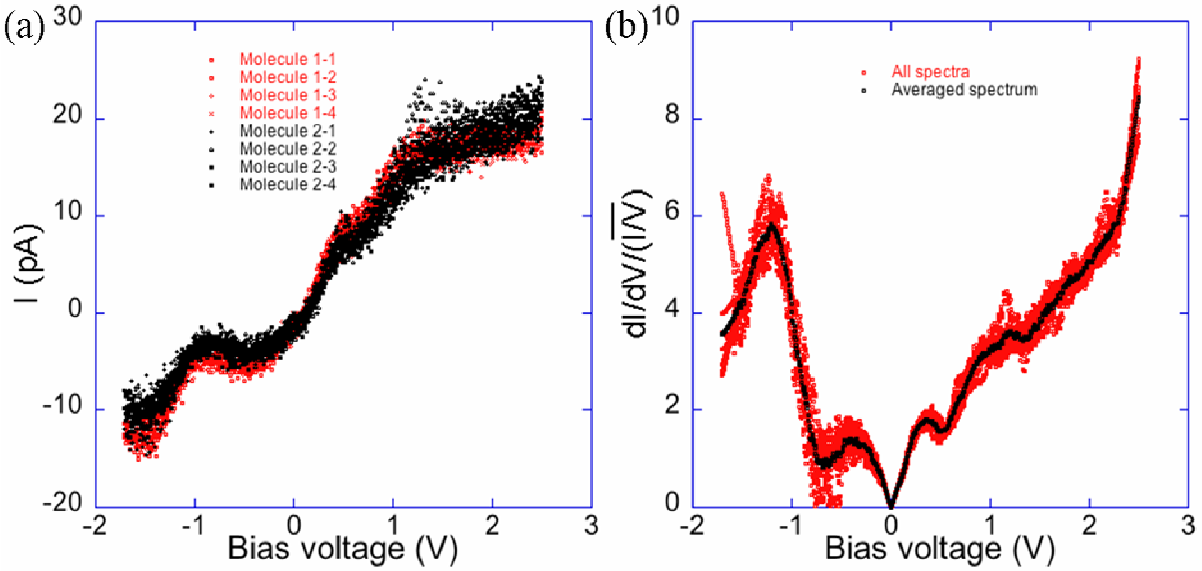

Figure 3.12 (a) Sets of *I-V* curves from different molecules; (b) $(dI/dV)/\overline{(I/V)}$ curves generated according to (a) and the final averaged $(dI/dV)/\overline{(I/V)}$ curve. Red dots stand for all data and black dots stand for the averaged data.

3.3.2 STM data analysis procedure

In order to generate non-local desorption data for chlorobenzene molecules on the Si(111)-7×7 surface, a programme written in Matlab by Dr. Peter Sloan was used that increased the accuracy and the efficiency of data analysis. Three types of images were acquired for this programme, STM images taken before electron injection, STM images taken during electron

injection and STM images taken after electron injection. The programme comprised two main stages. The first stage identified sites those were occupied by chlorobenzene molecules and those were not occupied by chlorobenzene molecules. The second stage compared two STM images taken before and after electron injection to locate sites where desorption occurred.

In the first site identification step, the programme opened an STM image; the area where the analysis needed was chosen and cut from the STM image. Within this area features such as contaminations or different domains and surface steps should be avoided by cutting them from the area. Once this was done, three primitive corner holes within one half unit cell could be selected from the image; the programme took this as the primitive mesh and extrapolated it over the whole surface. All adatom sites with respect to each unit cell were then circled and, by comparing with a threshold value, brighter sites (unoccupied sites) were highlighted by yellow circles, while dimmer sites (occupied sites) were highlighted by red circles. If either the mapping of adatom sites or the assignment of occupied sites and unoccupied sites were not accomplished desired, reselection of three primitive corner holes within one half unit cell was needed. Normally, the assignment of occupied sites and unoccupied sites done by the software was near perfect; however, any incorrectly assigned sites could be corrected manually. Fig 3.13 (a) and (b) give an example of STM images taken before (a) and after (b) the electron injection, after the process mentioned above. This procedure needed to be performed for different domains on different terraces respectively for both STM images taken before electron injection and STM images taken after electron injection.

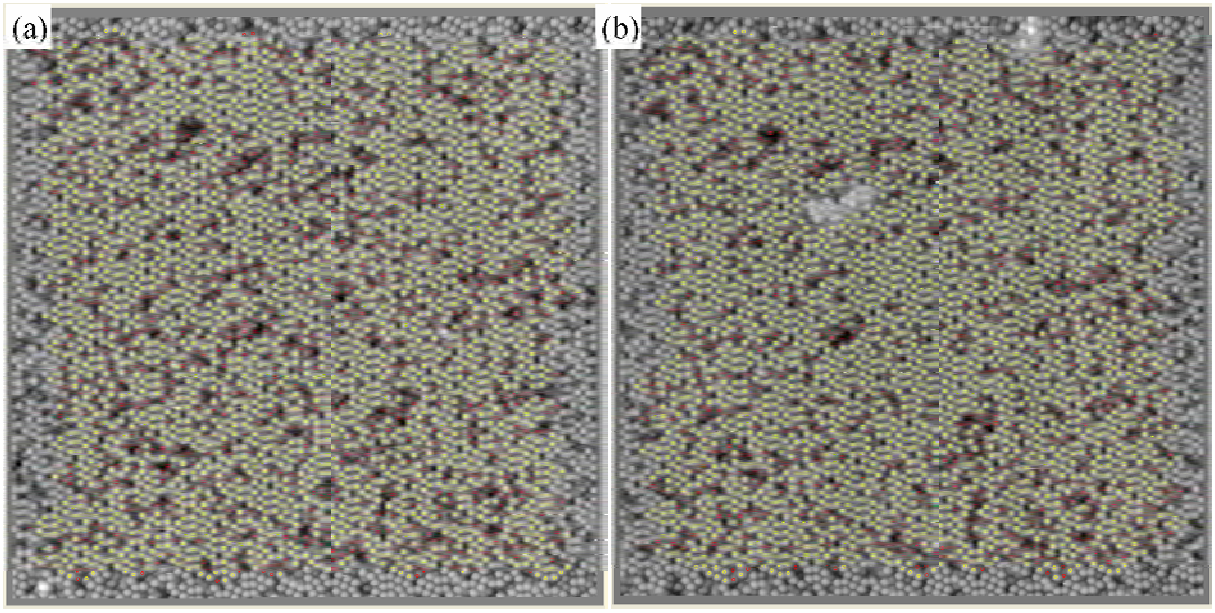

Figure 3.13 (a) An STM image taken before the electron injection after the programme processing. (b) An STM image taken after the electron injection after the programme processing.

In the second stage, modified STM images of the same domain on the same terrace taken before the injection and taken after the injection, together with the STM image taken during the injection, were selected. Then the injection site needed to be identified in the STM image taken before the injection. By comparing the selected area of the STM image taken before the injection together with that of the STM image taken after the injection, the injection site in the STM image taken after the injection could be found by the programme, as shown in Fig. 3.14 (a) and (b). By comparing corresponding sites in STM images before and after the injection, sites that were changed from occupied to unoccupied site could be recorded with respect to the injection site identified by the programme, as shown in Fig. 3.14 (c). Then the desorption probability $P(r)=N(r)/N_0(r)$ can be extracted from STM images by the programme and could be exported for further analysis, as shown in Fig. 3.14 (d). $N(r)$ was the number of desorbed chlorobenzene molecules at annulus r after the injection, while $N_0(r)$ was the number of chlorobenzene molecules at annulus r before the injection.

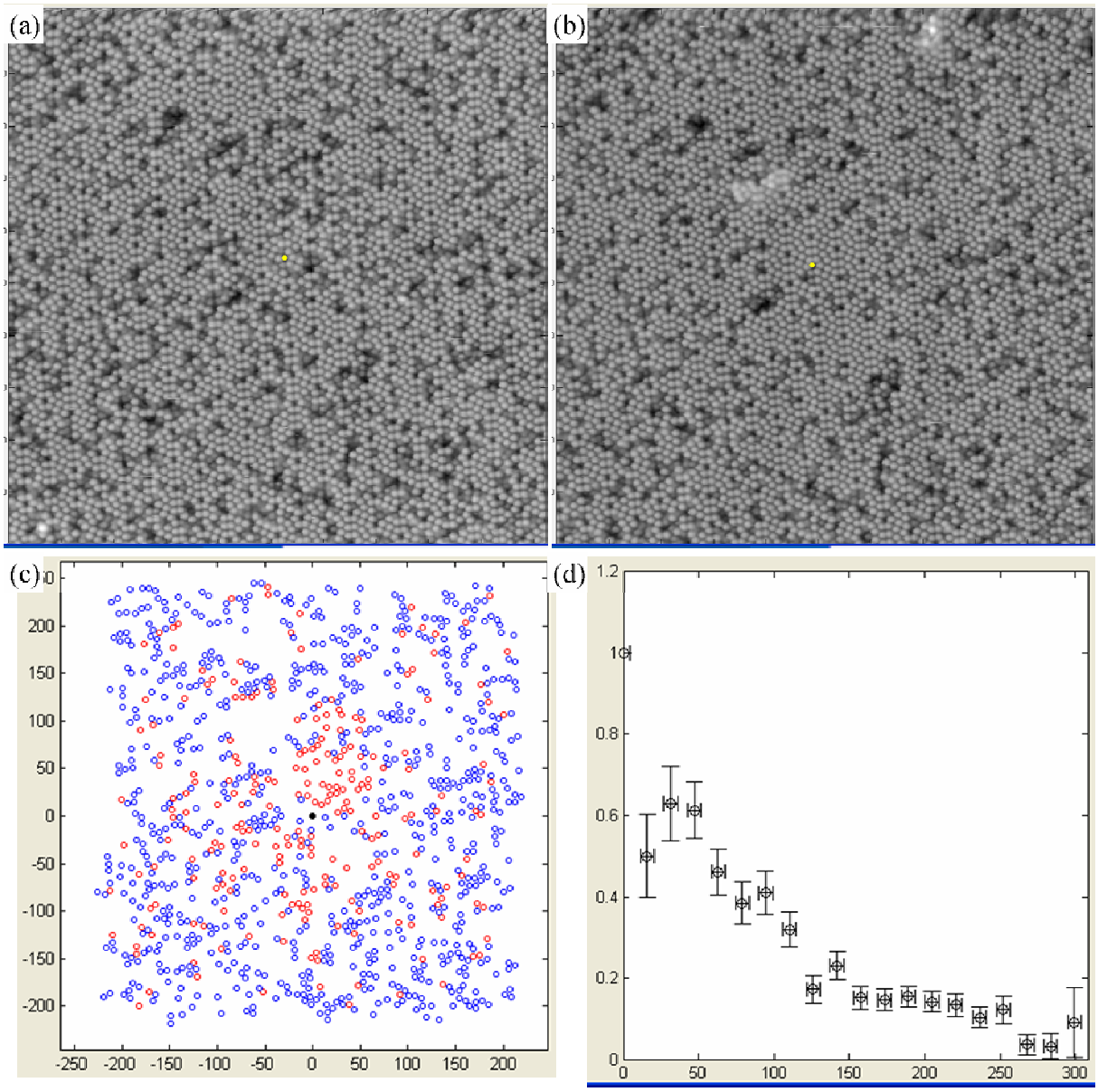

Figure 3.14 STM images taken before (a) and after (b) the electron injection. The yellow dot in (a) indicated the injection site is assigned manually, while the yellow dot in (b) indicated the same position after the injection is found by the programme. (c) The image generated by the programme indicates the cholorobenzene sites. The black dot in the centre stands for the injection site. Blue dots stand for sites remain occupied after the electron injection. Red dots stand for sites changed from occupied to unoccupied after the electron injection. (d) An example of the desorption probability *P(r)* vs radial distance data extracted from STM images by the programme processing.

Chapter 4 UHV STM study of chlorobenzene on the Si(111)-7×7 surface

This chapter is a supporting chapter for the chlorobenzene desorption on the Si(111)-7×7 surface, comprising a STS investigation on the chlorobenzene and a STM investigation of non-local desorption of chlorobenzene. It is divided into five sections. The first section describes the motivation and general introduction to the work. The second and third sections contain the spectroscopic results relating to the chlorobenzene adsorption geometry and the desorption mechanism. The fourth section shows non-local desorption of chlorobenzene on the stepped surface together with the temperature dependent non-local desorption of chlorobenzene. The final section gives the conclusion of these experiments, including confirmation of the rest atom involvement in the bonding structure, correlation of the adsorbate states to the thresholds in the desorption yield, and the demonstration of the non-local desorption process driven by electrons scattered from the bulk and the phonon assisted non-local desorption at low temperature. The main results of this work are prepared for publications.

4.1 Introduction and motivation

The Si(111)-7×7 surface is one of the standard substrates for performing atomic manipulation, although others such as Cu(001) and Si(100)-2×1 are also often used in this field of work. On

these substrates, atomic manipulations have been carried out on many different molecules, including chlorobenzene, benzene, pyridine and biphenyl andamino-nitro-azobenzene, and in various fashions, such as desorption, dissociation, switching and isomerisation [53, 54, 60, 82-86]. As such different reactions of these molecules on different substrates have been studied, among them, the chlorobenzene and similar molecules are of the key interest [87, 88]. Previously, the chlorobenzene molecule has been observed for various behaviours on the Si(111)-7×7 surface, such as adsorption, desorption, diffusion, and dissociation [40-42, 61, 62, 83-86]. Despite of a lot of investigation on the reaction of chlorobenzene on this substrate, the adsorption geometry of chlorobenzene on the Si(111)-7×7 surface still remains uncertain. Although several experiments have been performed and useful information and indirect evidence for the chlorobenzene adsorption geometry have been achieved, direct evidence of the proposed 2, 5 di-σ binding geometry [89] has never been found before. In this chapter, by the use of the scanning tunnelling spectroscopy (STS) technique, we acquired the direct evidence for the 2, 5 di-σ binding geometry, showing that beside one silicon adatom of the surface forming a C-Si bond with the chlorobenzene, the rest atom of the surface also forms a C-Si bond with the chlorobenzene. Furthermore, the same technique is used to investigate the desorption threshold of the chlorobenzene on the Si(111)-7×7 surface. And the non-local desorption effect found in the same system have also been studied.

4.2 STM and STS study of chlorobenzene adsorption

4.2.1 Previous study of chlorobenzene adsorption geometry

4.2.1.1 Si(111)-7×7 surface

The DAS (dimer-adatom-stacking-fault) model, proposed by Takayanagi *et al*. [90] is generally used to describe the Si(111)-7×7 reconstruction structure. According to this model, there are two reconstructed surface layers on top of unreconstructed bulk layers. In the topmost layer, there are 12 adatoms with one dangling bond each in one unit cell. These 12 adtoms are silicon atoms (indicated by the red points in Fig. 4.1), which can generally be "seen" by the STM under normal condition. In the first layer, except for atoms that form bonds directly with topmost adatoms, there are 6 rest atoms (indicated by brown points in Fig. 4.1) located among adatoms with one dangling bond each in a unit cell. These 6 rest atoms can be "seen" under certain conditions, for example, at low positive bias voltage and negative bias voltage. The second are located below the first layer. For the first unreconstructed layer, in the positions corresponding to the angles of the hexagonal unit cell, 4 silicon atoms with one dangling bond each are exposed in locations known as "corner holes". So a 7×7 hexagonal shape reconstructed unit cell consists of 12 adatoms, 6 rest atoms and 1 corner hole (each corner hole is shared by 4 unit cells). Due to the stacking structure, one of the half unit cell is named the "faulted half unit cell", and the other the "unfaulted half unit cell", as shown in Fig. 4.1. These different half unit cells can be distinguished at either low positive bias voltage, or negative bias voltage as shown in Fig 4.2. The size of one edge of the mesh is

~26.9 Å. Normally, after the surface has been annealed at high temperature and reconstructed as mentioned in Chapter 2, there will be steps generated on the surface. Depending on whether the surface is originally miscut or not, the miscut angle, the flowing direction of the resistant heating current, and whether the area is bunched or not, different numbers of steps with different heights can be observed. The height of a single step on the Si(111)-7×7 surface is ~3.1 Å [91]. This will be discussed further in stepped surface experiments in section 4.4.2.

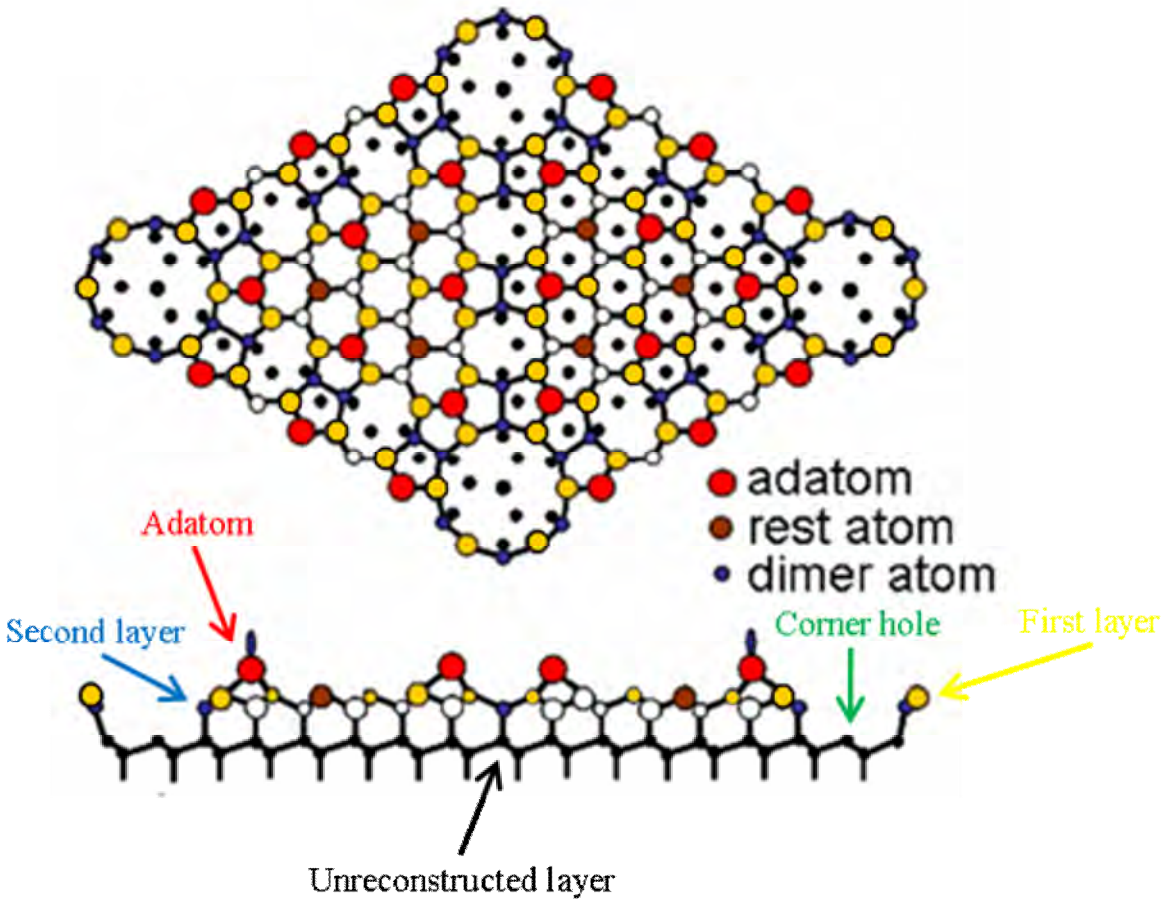

Figure 4.1 Top view and side view of the Si(111)-7×7 unit cell based on the DAS model with faulted half unit cell on the right. Red points indicate adatoms, brown points indicate rest atoms, yellow points indicate atoms in the first layer except for rest atoms, and blue points indicate dimer atoms in the second layer. (Image modified from Fig. 2 of ref. [92])

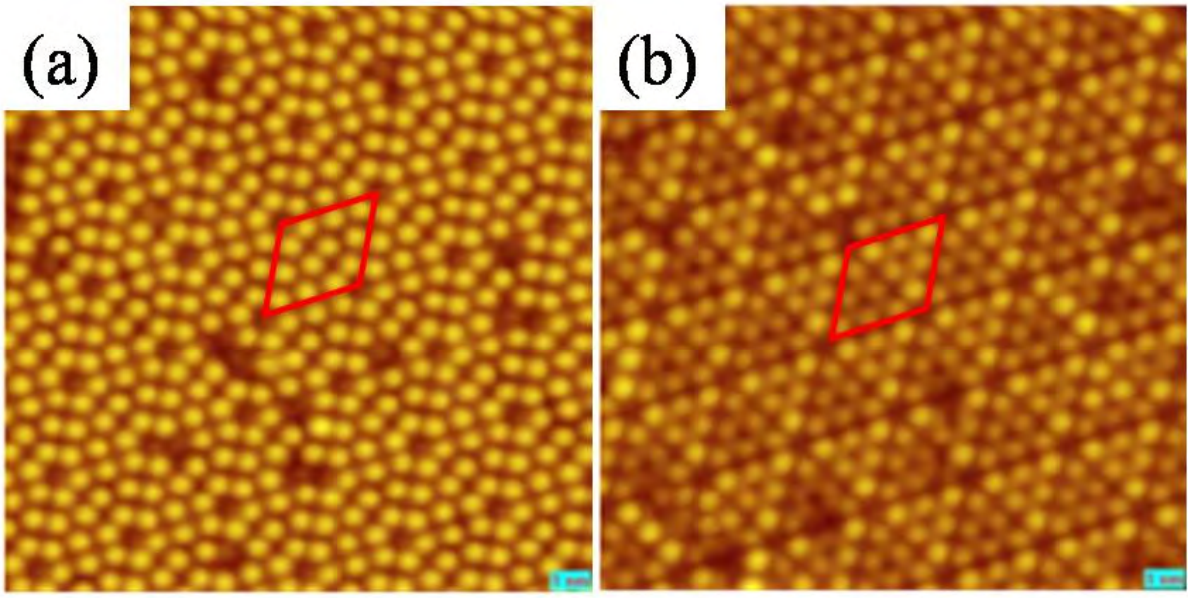

Figure 4.2 STM images of the Si(111)-7×7 surface with one unit cell in red rectangle. (a) An STM image taken at positive bias voltage (+1.0 V, 103 pA, 150 Å × 150 Å). (b) An STM image taken at negative bias voltage (-1.0 V, 103 pA, 150 Å × 150 Å).

4.2.1.2 Chlorobenzene absorption on the Si(111)-7×7 surface

From the previous study of Chen *et al.* [86] of the adsorption of chlorobenzene, preferred adsorption occurs on the faulted half unit cell with respect to the unfaulted half unit cell, and on centre adatoms with respect to corner adatoms at the ratio around 2:1. By comparison with the reaction preference between centre adatoms and corner adatoms for NH_3 on the Si(111)-7×7 surface, a "bridge" adsorption geometry for the chlorobenzene adsorbate was suggested, whereby a chlorobenzene molecule is bonded to an adatom-rest atom pair on the surface. Thus, due to the disturbance of the aromatic ring, the two wings on each side of the two bonded carbon atoms point up slightly, giving a bonding geometry that has been named the "butterfly" structure. This suggested adsorption geometry is supported by the observation that the saturation coverage obtained was 0.13 ML [86]. Given that for one 7×7 reconstruction unit

cell, there are 49 primitive unit cells, 0.13 ML (based on the definition given by the author) will yield 6 molecules per 7×7 reconstruction unit cell, which corresponds to the number of rest atoms in one reconstructed unit cell.

Another important investigation of the chlorobenzene adsorption geometry was reported by Cao *et al.* [89]. In this paper, they obtained two new clues as to the bonding structure. The first was from the HREELS result, where a splitting of two different C-H stretching modes was found in the spectrum, indicating that two chemical bonds were formed instead of one single chemical bond. The second was from a D-atom pre-exposure experiment. Since the D-atom preferentially adsorbed onto rest atoms, detection of physisorbed chlorobenzene after the D-coverage increased to 1/3 ML (given one unit cell in the 7×7 reconstruction structure has 18 dangling bonds, 6 dangling bonds of rest atoms out of 18 dangling bonds is 1/3.) strongly suggested the involvement of the rest atom in the chlorobenzene adsorption.

Due to the similarity between benzene and chlorobenzene, the similar bonding geometry in the adsorption of benzene on the Si(111)-7×7 surface can provide insight into the bonding geometry of chlorobenzene. Based on the HREELS results for benzene adsorption on Si(111)-7×7, Cao *et al.* [93] ruled out the π-bonding model for benzene adsorption, where benzene is bonded only to a single dangling bond of the surface, and concluded that formation of two chemical bonds between two carbon atoms in benzene and two adjacent Si atoms with dangling bonds.

All the above point to a structure in which adsorbed chlorobenzene molecule is in the 2,5 di-σ bonded butterfly structure, as shown in Fig. 4.3. However, direct evidence or observation, notably by structural tools such as STM, of this proposal is still lacking.

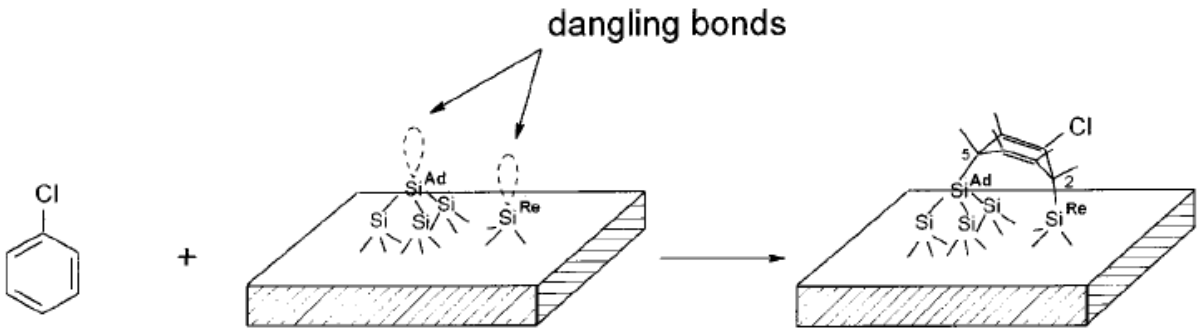

Figure 4.3 A schematic diagram of chlorobenzene adsorption on Si(111)-7×7 in a 2,5 di-σ bonded butterfly structure. The adatom and the rest atom bonded to the molecule are indicated by arrows. (Images and caption modified from ref. [89])

4.2.2 STS study of chlorobenzene adsorption geometry

In STM images shown in Fig. 4.4 and Fig. 4.5, the chlorobenzene molecule is presented as a missing adatom and a brightened rest atom. In Fig. 4.4 (a), the molecule is on the faulted half, and in Fig. 4.5 (a) the molecule is on the unfaulted half. The identification of the faulted and unfaulted half unit cell was done by scanning the surface away from the target molecule at negative bias voltage in the same domain of the target molecule. This rest atom appears either brighter or dimmer in the images depending on the magnitude of the positive bias voltage. Moreover, in the image two adjacent adatoms next to the bonding rest atom are both slightly brighter than neighbouring adatoms at positive bias voltage. Finally, the darkening of the middle adatom in the nearest different half unit cell can also be resolved at negative bias voltage in both figures [42, 83].

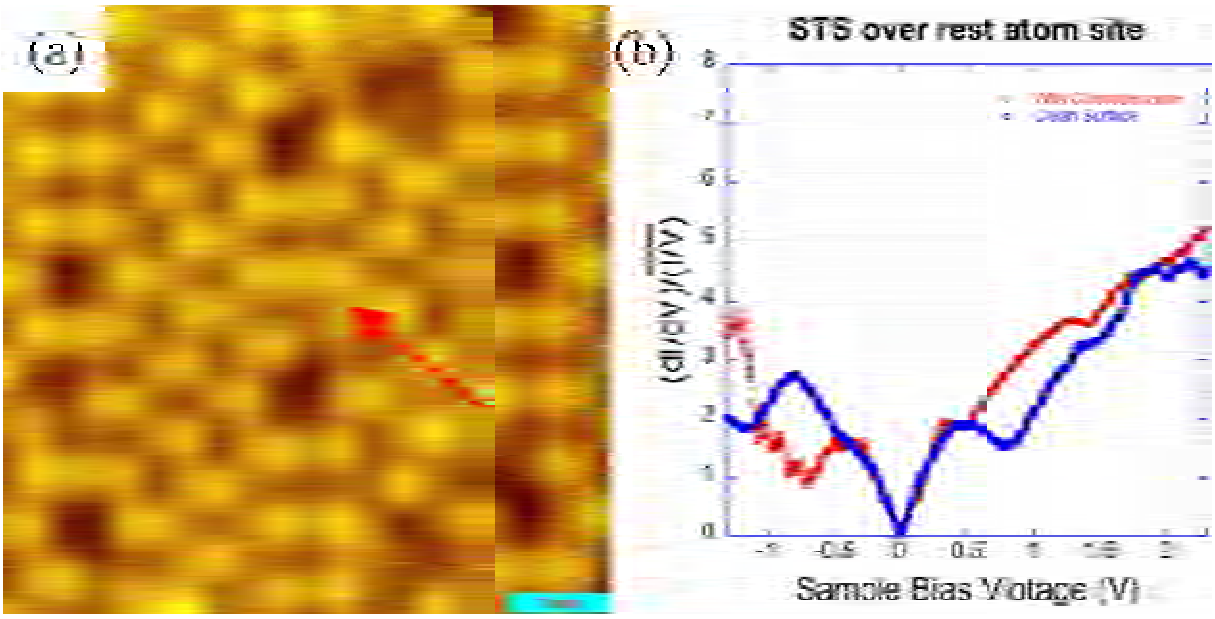

Figure 4.4 (a) An STM image of a chlorobenzene on the **faulted half** unit cell of the Si(111)-7×7 surface, the red arrow shows the site where STS was performed. The STM image was acquired at +1.47 V, 19.6 pA, 60 Å × 60 Å. (b) The STS curve acquired at the site as shown in (a) for a clean surface (blue curve) and for the surface with a bonded molecule (red curve).

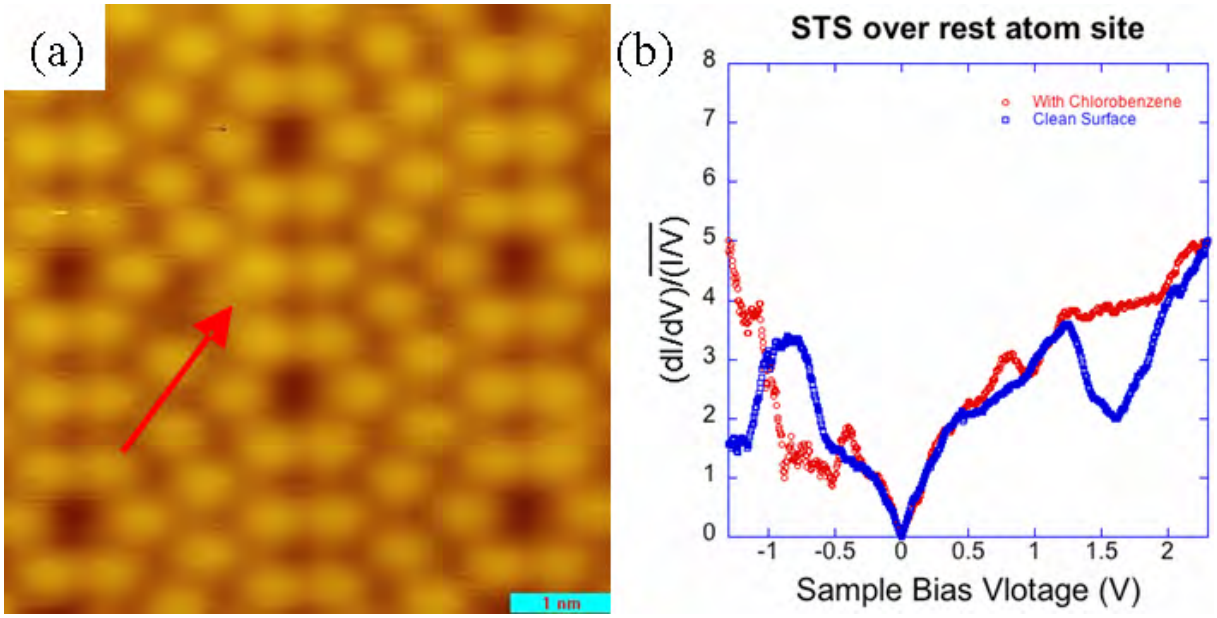

Figure 4.5 (a) An STM image of a chlorobenzene on the **unfaulted half** unit cell of the Si(111)-7×7 surface, the red arrow shows the site where STS was performed. The STM image was acquired at +1.47 V, 21.0 pA, 60 Å × 60 Å. (b) The STS curve acquired at the site as shown in (a) for a clean surface (blue curve) and for the surface with a bonded molecule (red curve).

Based on previous papers [94-96], the peak in STS curve at around -0.8 V was contributed by

the rest atom state. Here, in both Fig. 4.4 (b) and Fig. 4.5 (b) for the faulted and unfaulted half unit cells, we observe a peak at around -0.9 V in the curve for the clean surface. In both Fig. 4.4 (b) and Fig. 4.5 (b), when comparing STS curves for a surface sites with chlorobenzene adsorbed (red) and a clean surface (blue), an important change is observed: the elimination of the rest atom state in the curve (red) for the adsorbed molecules. From the previous study [94], a missing rest state and missing adatom state confirmed that new bonds were formed between the rest atom and the adsorbed molecule in the case of the NH_3 reaction with the Si(111)-7×7 surface. The elimination of the rest atom state in curves (red) for the surface with adsorbed chlorobenzene shown in Fig. 4.4 (b) and Fig. 4.5 (b) provides the direct evidence that a bond is formed between the rest atom and the adsorbate.

4.3 STM and STS study of chlorobenzene desorption

Based on previous manipulation studies [41, 42, 61, 83], there were two processes occurring when a pulse of current was applied by the STM tip to a chemisorbed chlorobenzene on a Si(111)-7×7 surface; one was desorption of the chlorobenzene molecule from the surface and the other was dissociation of the C-Cl bond in the chlorobenzene molecule. These investigations found a voltage dependence of the desorption process. Theoretical discussion in [41] suggested that the π orbital of the carbon ring might be involved in the desorption process, which in calculation matched quite well with the desorption threshold. However, direct experimental results, which can reveal the correspondence between electronic states and desorption thresholds, have not been reported. Here we used STS to reveal the relevant

state.

4.3.1 Previous study of chlorobenzene desorption

Like the example given in section 2.3.2 for Cl diffusion on the Si(111)-7×7 surface, STM can be applied to the field beyond observing the surface morphology. Just as Cl diffusion could be induced by STM, desorption and dissociation of chlorobenzene induced by the STM were found. In the previous studies of Sloan and Palmer [41, 42, 61, 82, 83], detailed investigations were reported of the property of desorption and dissociation processes for chlorobenzene on the Si(111)-7×7 surface. The desorption process showed a clear voltage dependence, with two thresholds for the onset of desorption located at +2.1 V and -1.2 V surface bias. Fig. 4.6 shows the voltage dependence of the desorption process under different experimental conditions. The voltage dependence of the desorption was independent of different tip configurations, adsorption sites and dopant types, which indicated the desorption mechanism was related to the excitation of the molecule-substrate bond. Theoretical work was carried out, by M. F. G. Hedouin and Professor M. Persson, to find which state might be involved in this process.

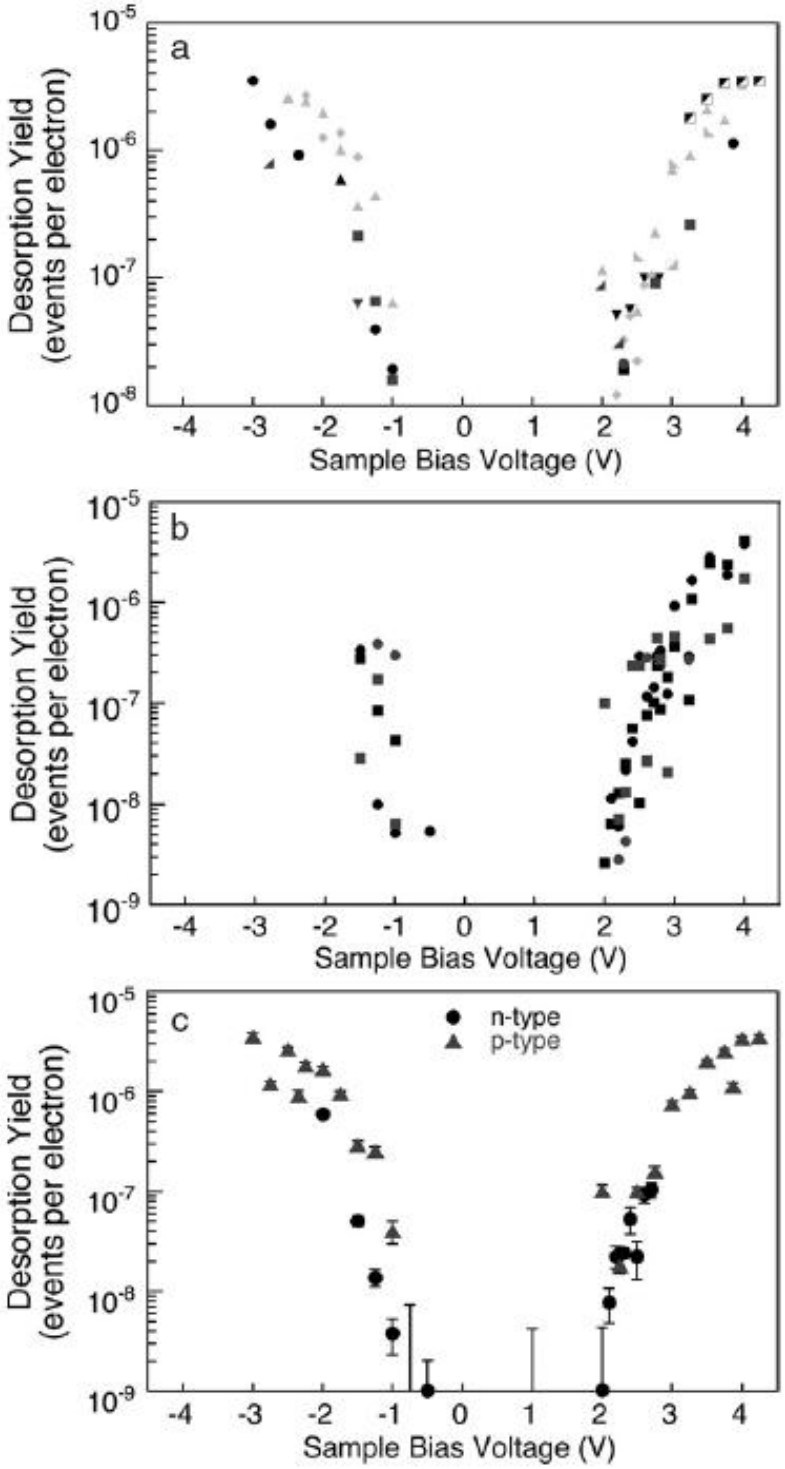

Figure 4.6 (a) Desorption yield of the chlorobenzene molecule as a function of the applied voltage acquired under 16 different tip conditions. (b) Desorption yield of the chlorobenzene molecule at different adsorption sites as a function of the applied voltage. The grey, black, square and circle symbols represent the data acquired at the faulted half unit cell, the unfaulted half unit cell, middle adatoms and corner adatoms. (c) Desorption yield of the chlorobenzene molecule on different doped samples as a function of the applied voltage. The circle and triangle represent the data acquired on n-type and p-type samples, respectively. (Images and caption modified from ref. [42])

Fig. 4.7 (a) includes the calculated partial density of *p* states on of carbon atoms which are involved in the bonding of chlorobenzene. This figure correlates well with the thresholds for desorption at both polarities. Although the theoretical results fit nicely with the desorption threshold, direct experimental evidence of the states involved has yet to be provided. In following sections, through STS, these states we recorded in the electronic structure of the molecule-substrate system in accordance with the thresholds for desorption.

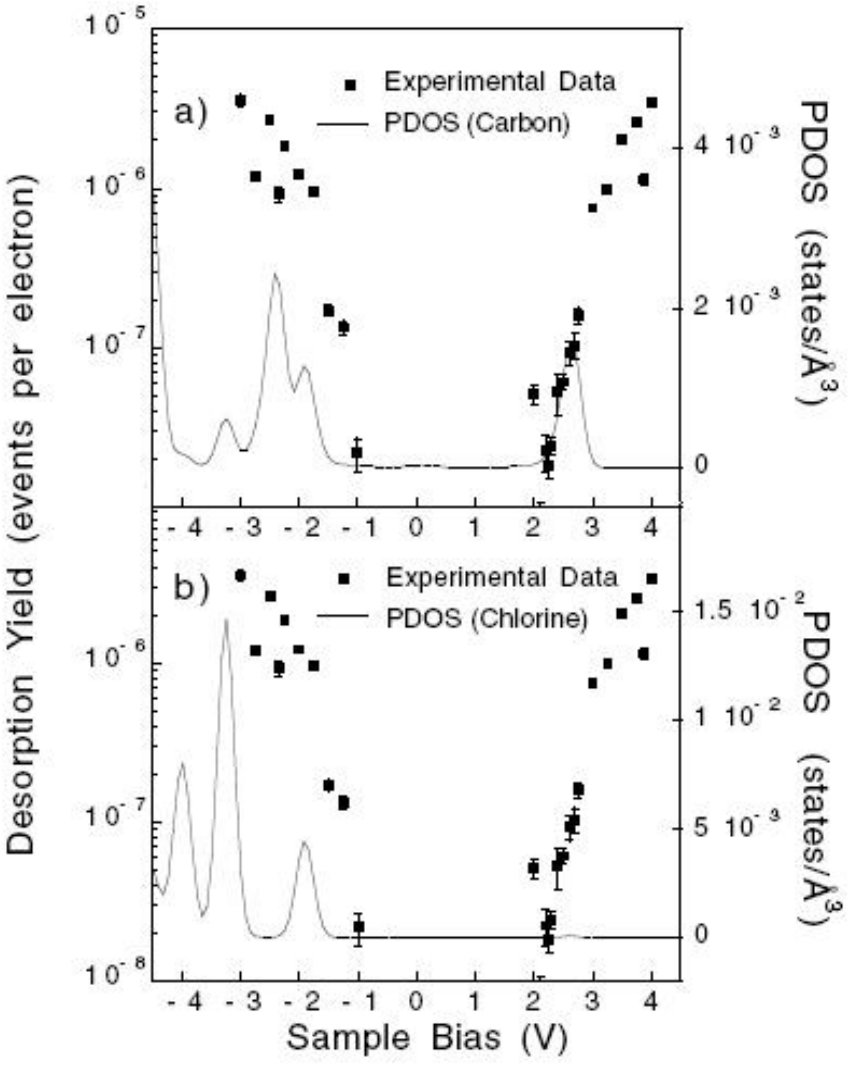

Figure 4.7 (a) Desorption yield of the chlorobenzene molecule as a function of the applied voltage compared with the calculated partial density of *p* states (solid lines) of the carbon atom in the ring. (b) Same condition for that of the chlorine atom. (Images and caption modified from ref. [41])

4.3.2 STS study of chlorobenzene desorption on the Si(111)-7×7 surface

Figs. 4.8 and 4.9 are STS curves acquired at different sites (on top of the bonded centre adatom and the corner adatom) on the faulted half unit cell and unfaulted halt unit cell according to the method described in section 3.3.1. Data for the desorption yield versus the voltage were included in the figures for comparisons. Previous studies have shown that the desorption yield was unaffected by the status of the tip [42], but whether the same is true in the STS is not known, therefore we performed STS of the surface with a chemisorbed molecule followed by that of a clean surface. The tip condition should be nearly the same in both cases and the features generated from the comparison between the former and latter STS curves unaffected by the tip status. We compared our STS data of the clean surface with that of another group, Mysliveček *et al.* [96] (see Table. 1) to assign different features in our curves to different surface states.

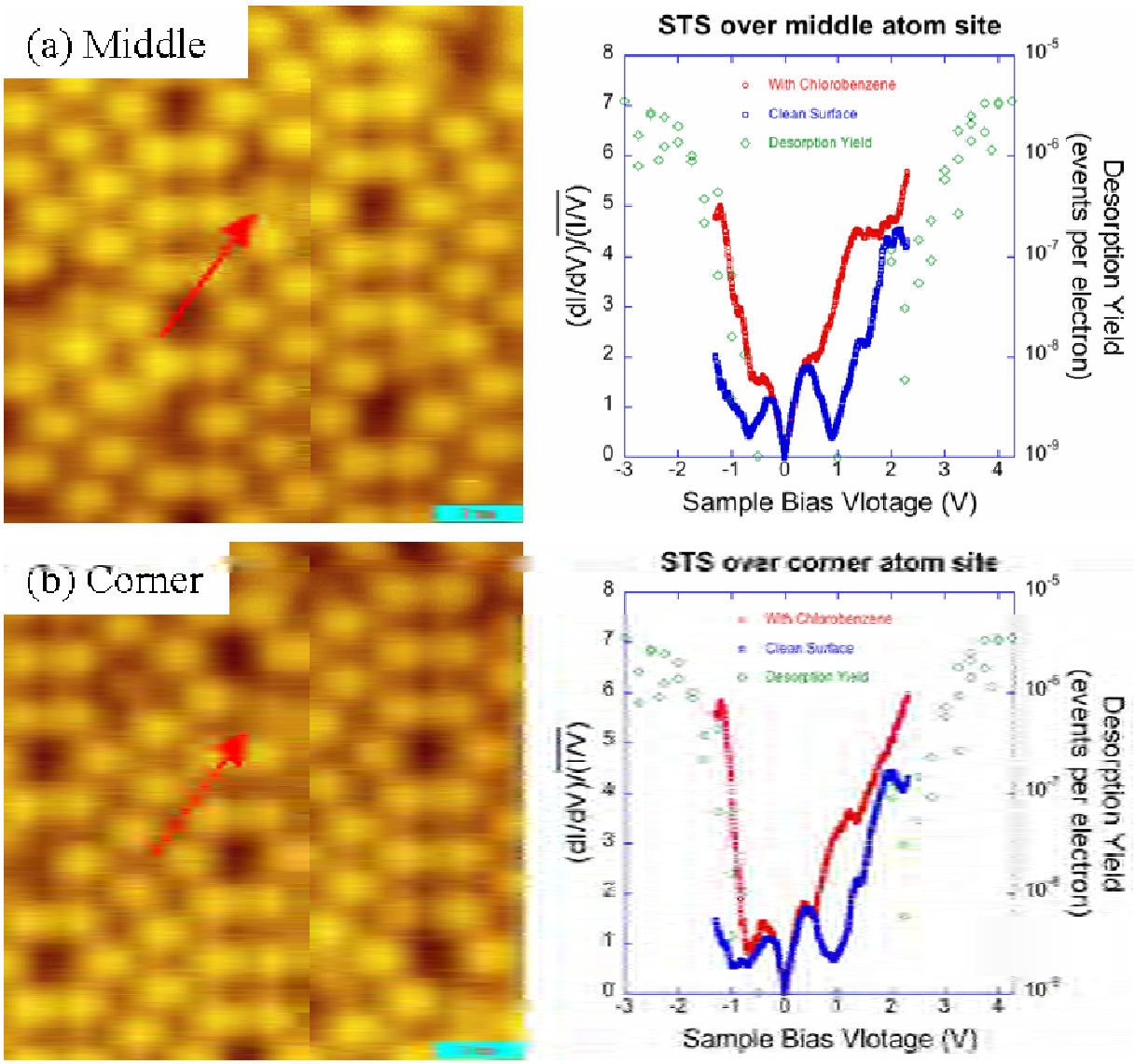

Figure 4.8 STS curves acquired at different bonded sites for both corner adatom-rest atom bonded chlorobenzene and middle adatom-rest atom bonded chlorobenzene in the **faulted half** unit cell. (a) STS curves taken in the middle adatom, as shown the STM images, of both the clean surface (blue) and the surface with a bonded molecule (red). The STM image was acquired at +1.47 V, 21.1 pA, 60 Å × 60 Å. (b) STS curves taken in the corner adatom, as shown in the STM image, of both the clean surface (blue) and the surface with a bonded molecule (red). The STM image was acquired at +1.47 V, 22.2 pA, 60 Å × 60 Å. Green diamonds are the desorption data from ref. [41].

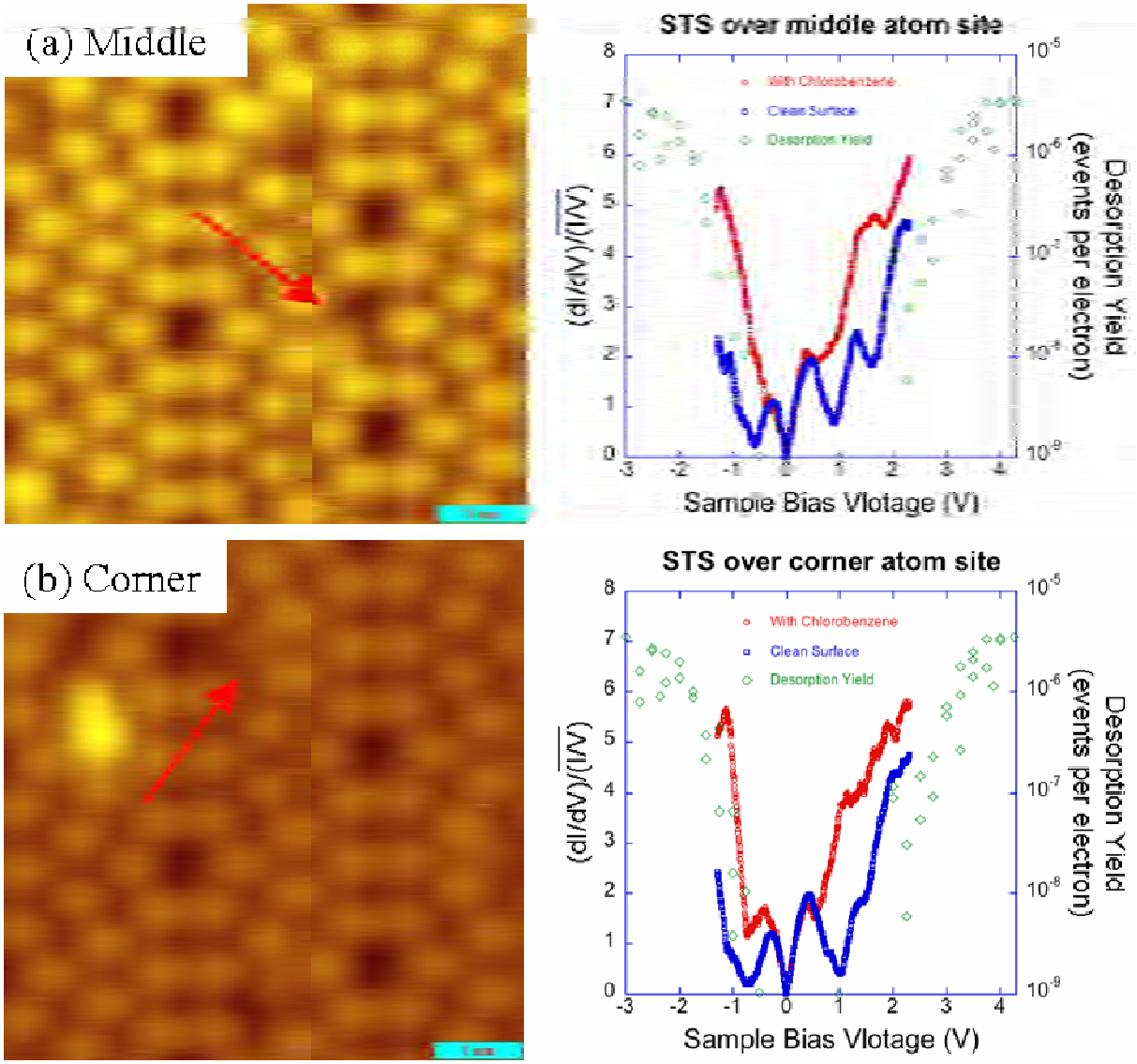

Figure 4.9 STS curves acquired at different bonded sites for both corner adatom-rest atom bonded chlorobenzene and middle adatom-rest atom bonded chlorobenzene in the **unfaulted half** unit cell. (a) STS curves taken in the middle adatom, as shown in the STM image, of both the clean surface (blue) and the surface with a bonded molecule (red). The STM image was acquired at +1.47 V, 20.9 pA, 60 Å × 60 Å. (b) STS curves taken in the corner adatom, as shown in the STM image, of both the clean surface (blue) and the surface with a bonded molecule (red). The STM image was acquired at +1.47 V, 21.0 pA, 60 Å × 60 Å. Green diamonds are the desorption data from ref. [41].

STS peak	Location	Energy at RT (eV)
S_2	Rest atoms	−0.78±0.05
S_1'	Faulted corner adatoms	−0.45±0.05
S_1	Corner adatoms	−0.14±0.05
U_1'	Center and corner adatoms	0.20±0.05
U_1	Corner adatoms	0.33±0.05
U_1''	Center adatoms	0.41±0.05

TABLE 1. Different peaks in the STS curve assigned to different physics origins on the surface at room temperature. (Images and caption modified from ref. [96])

In ref. [96], the peak in the STS curve at around -0.78 V was attributed to the rest atom state, while ours appears at -0.9 V, as mentioned in section 4.2.2. Peaks found by Mysliveček *et al*. at around -0.45 V and -0.14 V were assigned to the faulted corner and corner adatoms, respectively. Though we could not clearly make this distinction from our curves for the peak at -0.14 V, the peak at -0.4 V of Fig. 4.8 (b) was clear. As a result, we assigned peaks at -0.4 V in Fig. 4.8 (b) to faulted corner adatoms. At positive bias voltage, there were three peaks in ref. [96], however, in our spectra, we could not identify corresponding features. However, the peak at around +0.4 V, which was usually assigned to the adatom state [97], was clearly seen in our curves, so we attributed this peak at +0.4 V to both center and corner adatoms. One feature that had to be mentioned was the backbond state at +1.4 V [97], Mysliveček *et al.* did not find this in their experiments, but we could distinguish it in Fig. 4.8 and Fig. 4.9. Overall, our curves matched well with the previous work, which enabled us to compare our STS data with the data from desorption experiments.

For chemisorbed chlorobenzene, the most significant change between the electronic structure

of the clean surface (blue curve) and that of the chemisorbed molecule bonded surface (red curve) was a peak at around -1.2 V and a plateau at +1 V to +2 V in Fig. 4.8 and Fig. 4.9. At negative voltage, the peak at -1.2 V was in good agreement with the onset of the desorption. At positive voltage, the new state (a plateau at +1 V to +2 V) generated by the adsorbate did not seem to match the onset of the desorption threshold start at +2.1 V [41]. This mismatching at positive voltage will be explained in section 4.4 and is thought to be due to another important phenomenon in this system, i.e., non-local chlorobenzene desorption on the Si(111)-7×7 surface. The key conclusion from this experiment is that at negative voltage, a new generated states at -1.2 V matching to the desorption threshold is confirmed by the STS investigation.

4.4 STM study of chlorobenzene non-local desorption

4.4.1 Previous study of chlorobenzene non-local desorption

During the investigation of chlorobenzene molecule desorption on the Si(111)-7×7 surface, we noted some chlorobenzene molecule desorption occurred several nanometers away from the place where electrons were injected. Fig. 4.10 gives an example of such a process where, after the pulse was applied at the centre of the area, chlorobenzene molecules desorbed from the centre to the outer area.

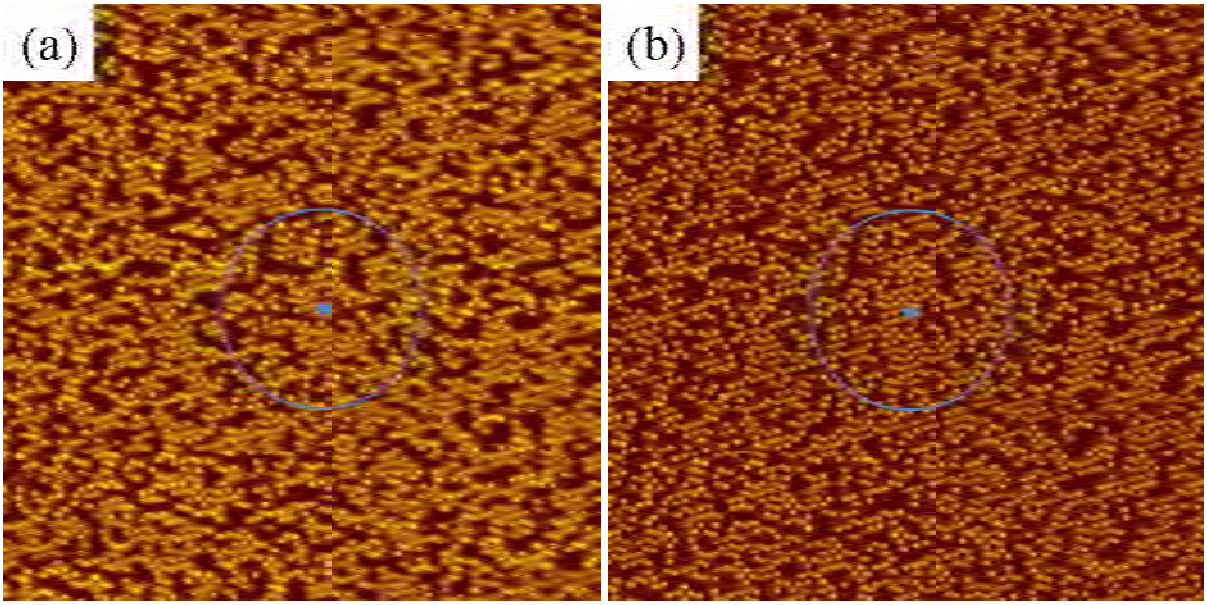

Figure 4.10 STM images taken before (a) and after (b) a pulse applied in the centre of the image (+1.0 V, 50 pA, 51.2 nm × 51.2 nm). The blue dot indicates the injection site. The area circled shows the main non-local desorption area.

The experiment carried out by Sloan *et al.* [40] investigated non-local chlorobenzene desorption on the flat Si(111)-7×7 surface. It was found that the efficiency of non-local chlorobenzene desorption with respect to the injection site was proportional to the local density of states at the corresponding energy. At +2.1 V, the local density of states is maximized over the corner holes, so injection at above +2.1 V can result in more efficient non-local chlorobenzene desorption, as shown in Fig. 4.11.

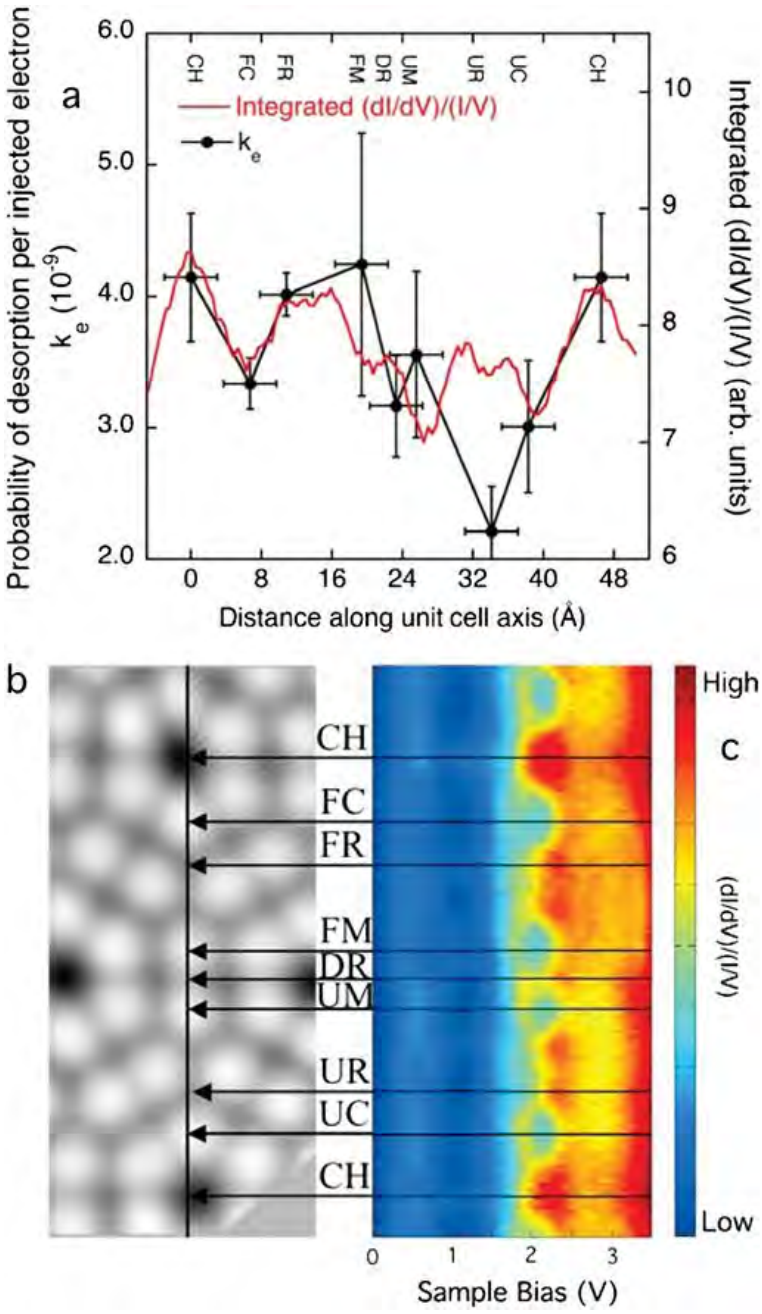

Figure 4.11 (a) Non-local desorption probability per chlorobenzene molecule per electron under +2.7 V pulse (black line) at different sites on the surface. CH, FC, FR, FM, DR, UM, UR and UC stand for corner-hole, faulted corner adatom, faulted rest atom, faulted middle adatom, dimer row, unfaulted middle adatom, unfaulted rest atom and unfaulted corner adatom sites, respectively. The integrated STS data over +2.0 to +2.7 V of the clean surface is shown in the red line. (b) An STM image shows corresponding sites on the surface. (c) The STS data over different sites as indicated in (b). (Images and caption modified from [40])

This indicated that the desorption of the chlorobenzene did not depend only on the threshold of the molecular state, but also on the surface state. This explained why the state observed in

the STS curve (a new state at +1 to +2 V) did not match the threshold of the chlorobenzene desorption at positive voltage (+2.1 V), while it did match at negative voltage. Furthermore, non-local desorption could also occur across the surface steps. This, together with non-local desorption dependence on the injection site, indicated that there might be a surface state (a channel) located a few layers below the outmost surface layer that crossed the steps uninterrupted.

4.4.2 Non-local desorption of chlorobenzene on the stepped Si(111)-7×7 surface

Quantified experiments were carried out on the stepped Si(111)-7×7 surface. If our proposal is right, then there must be a point where this surface state is truncated. When the step is high enough, such that non-local desorption is stopped by the step. To ensure a wide variety of different step heights on the surface, miss-cut ($0.5^{o} \pm 0.5^{o}$) silicon samples were used in these experiments. Injections on the high terrace as well as the low terrace were carried out for both electron and hole injections. The injection site was selected to be the first corner hole closest to the step edge. Since the step edge can be several nanometers wide, this can provide more data points on both high and low terraces. Steps of up to 5 layer height were tested for the electron injection and up to 4 layer height for the hole injection. The applied pulse was +3.3 V for 10 s. The experiments were performed as follows. Firstly, an area with a step edge across the middle was located and an STM image before the pulse recorded under the passive condition at +1.0 V, 100 pA. Then a pulse was applied to the selected site in the middle of STM image, either on the high terrace or the low terrace. After the pulse, another STM image

was recorded under the passive condition, as shown in Fig. 4.12.

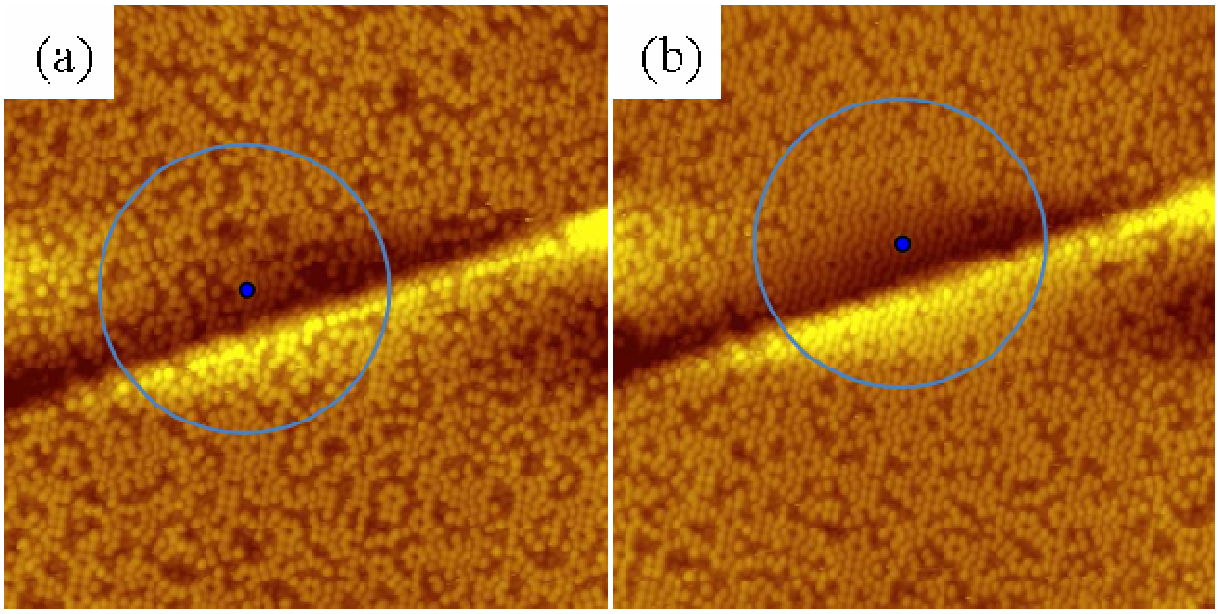

Figure 4.12 (a) STM image before the electron injection (+1.0 V, 100 pA, 45 nm × 45 nm). (b) STM image after the electron injection (+1.0 V, 100 pA, 45 nm × 45 nm). The step is a double step. (Injection at ±3.3 V, 400 pA, 10 s). The blue dot indicates the injection site.

The images were processed using the Matlab programme written by Dr. Peter Sloan as described in section 3.3.2. The data of the desorption probability *P(r)* versus the distance *r* from the injection site was generated using this programme. The desorption probability is the ratio of the number of desorbed molecules to the total number of molecules before the injection. *P(r)* can be averaged over the distance to generate P_{HL} or P_{LH}, where P_{HL} is the average probability of non-local desorption on the high terrace for the injection on the low terrace, and P_{LH} is the average probability of non-local desorption on the low terrace for the injection on the high terrace. Finally, the desorption ratio

$$Desorption\ ratio\left(HL/LH\right)=\frac{P_{HL}}{P_{LH}} \tag{4.1}$$

can be generated, as shown in Fig. 4.13.

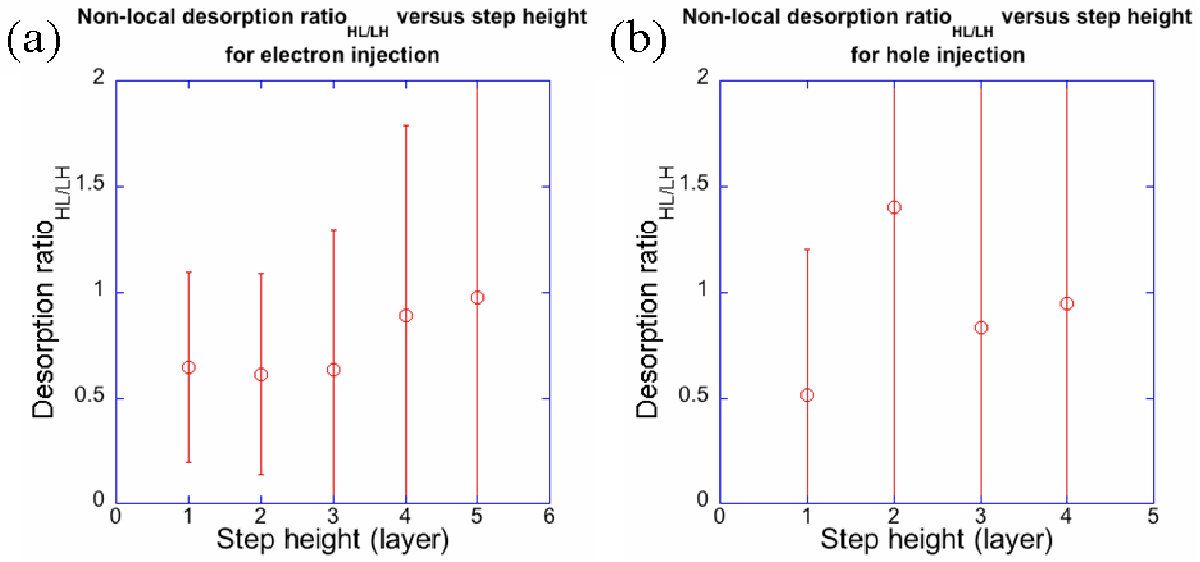

Figure 4.13 (a) Non-local desorption ratio$_{HL/LH}$ versus step height for the electron injection. (b) Non-local desorption ratio$_{HL/LH}$ versus step height for the hole injection. The desorption ratio$_{HL/LH}$ means the ratio of the probability of non-local desorption occurred on the high terrace for the injection on the low terrace to the probability of non-local desorption occurred on the low terrace for the injection on the high terrace.

If there is a point where the step is high enough that this surface state is truncated then, it should be apparent in Fig. 4.13. If a certain height of the step can stop the electron or the hole from transferring across the step, then P_{LH} (for the electron or the hole transfers "uphill") will be much smaller than P_{HL} (for the electron or the hole transfers "downhill"). This is because electron or hole transfers "downhill" can still occur on the surface even if the "underground" channel is cut. However, except for the data from the step height less than 4 layers for the electron injection and the step height less than 2 layers for the hole injection, all the ratios for different step heights were around one for both the electron injection and the hole injection. This result indicates that both the electron and the hole cannot quite sense the step. Also since nearly all the ratio data are below 1, it may show that the non-local desorption favours the electron flowing from the low terrace to the high terrace ("uphill"). These results may indicate

that electrons may not travel through a channel lying certain layers below the surface, but instead go into the bulk and then bound back to the surface to cause non-local desorption.

4.4.3 Non-local desorption of chlorobenzene at different temperatures

Beside the step height dependent non-local desorption experiments performed on the stepped Si(111)-7×7 surface, temperature dependent non-local desorption experiments can also provide more information about non-local desorption mechanism. The previous investigation done by Dr. Peter Sloan has shown at low temperature (77 K and 4 K), non-local desorption probability seemed to reduce greatly, and nearly no radius decay of non-local desorption probability could be seen. Therefore, in order to find out when the non-local desorption phenomenon disappears, non-local desorption experiments at different temperatures (77 K, 120 K, 175 K, 230 K, 293 K, 313 K and 323 K) were performed. In order to compare the results acquired at low temperature with room temperature and above, high conductance boron doped silicon samples were used in these experiments. Electron injections were done at +2.7 V, 800 pA for 8 s. The experiments were performed in a similar fashion as the stepped experiments described in section 4.4.2 above. The images were processed using the Matlab programme written by Dr. Peter Sloan as described in section 3.3.2, and data of desorption probability *P(r)* versus distance *R* from the injection site was generated. By applying the equation from ref. [40],

$$k_e f(r) = -e2\pi r \ln\left[N(r)/N_0(r)\right]/stIL \tag{4.2}$$

the chlorobenzene desorption probability per impinging electron per molecule at radius r from

the injection site was generated. $N_0(r)$ is the number of molecules on the annulus at radius r before injection and $N(r)$ is the number of molecules on the annulus at radius r after injection, so $N(r)/N_0(r)$ can be derived from $1-P(r)$ (since $P(r)$ is the ratio of the number of desorbed molecules to the total number of molecules before the injection). k_e refers to the chlorobenzene desorption probability per impinging electron, $f(r)$ refers to the radial decay of the current, s=1 represents the fraction of the current flow across the surface, t is the injection time, I is the injection current, and L=5 Å refers to the cross section of a single chlorobenzene molecule.

Fig. 4.14 (a) shows the desorption probability versus the radius from the electron injection site from previous experiments done by Dr. Peter Sloan on the low conductance sample and Fig. 4.14 (b) shows the experiment in the current study done on the high conductance sample at room temperature. Through the comparison between Fig. 4.14 (a) and (b), several features can be noticed. First, the length of the suppression region (where the desorption probability increases as the radius increases) close to the injection site is roughly the same for both cases, within around 75 nm. Second, the maximum desorption probability on the low conductance sample is slightly higher than that on the high conductance sample. This may be due to the presence of fewer defects on the low conductance sample than the high conductance sample. Since the programme generally counts dark spots before and after the injection, and the defect normally exhibits as the dark spot on the surface, unaffected by the injection, the presence of defects may result in a “less effective” desorption probability on the high conductance sample. Third, the desorption probability on the low conductance sample decays much faster than that on the high conductance sample, indicating a shorter decay length.

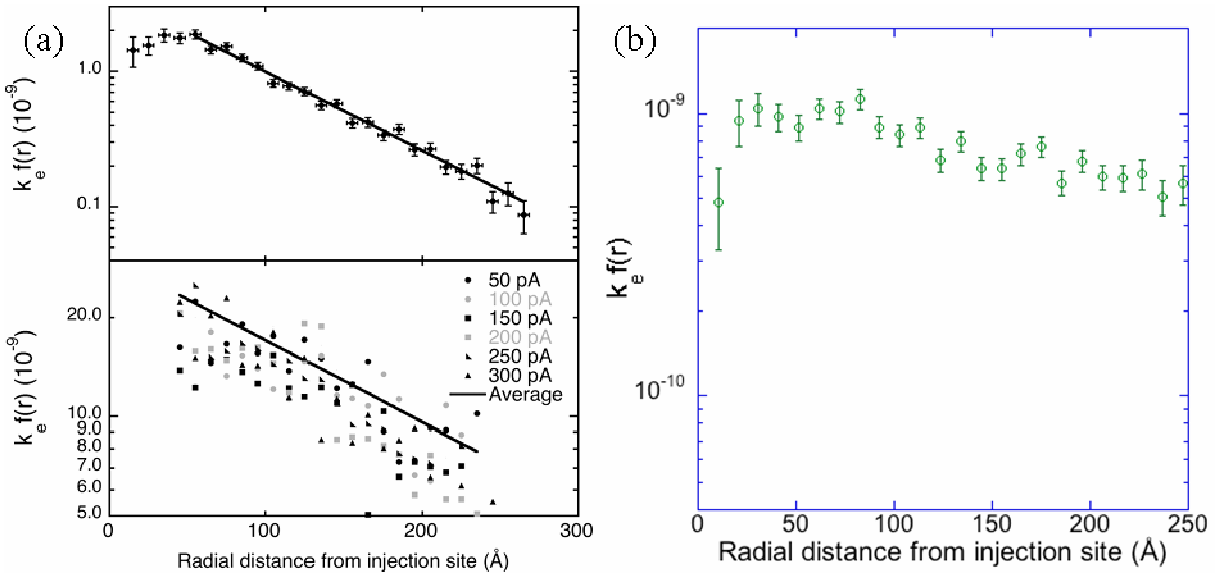

Figure 4.14 (a) Non-local desorption probability as a function of the radius from the injection site on the low conductance sample at room temperature (electron injection at +2.7 V). (b) Non-local desorption probability as a function of the radius from the injection site on the high conductance sample at room temperature (electron injection at +2.7 V, 800 pA, 8 s).

Figs. 4.15 (a) to (d) show STM images before and after the electron injection at 77 K and 230 K, respectively, showing clearly that the non-local desorption region is bigger at higher temperature. Non-local desorption experiments on the high conductance sample over a range of different temperatures are shown in Fig. 4.15 (e). Generally, the maximum desorption probability increases as the temperature increases (except for the case at 323 K). It also shows that the length of the suppression region close to the injection site increases as the temperature increases. At 77 K, the suppression region is only around 20 nm, while it increases to around 75 nm at 293 K, as mentioned above. At 313 K, the suppression region is over 200 nm, much longer than that at 293 K; and at 323 K, there is no decay apparent at all within 250 nm range, which may indicate the suppression region longer than 250 nm. This may be the reason why the maximum desorption probability at 323 K is smaller than that at 293 K and 313 K. This suppression region may originate from the electric field beneath the tip, which may hinder the molecule desorption beneath the tip.

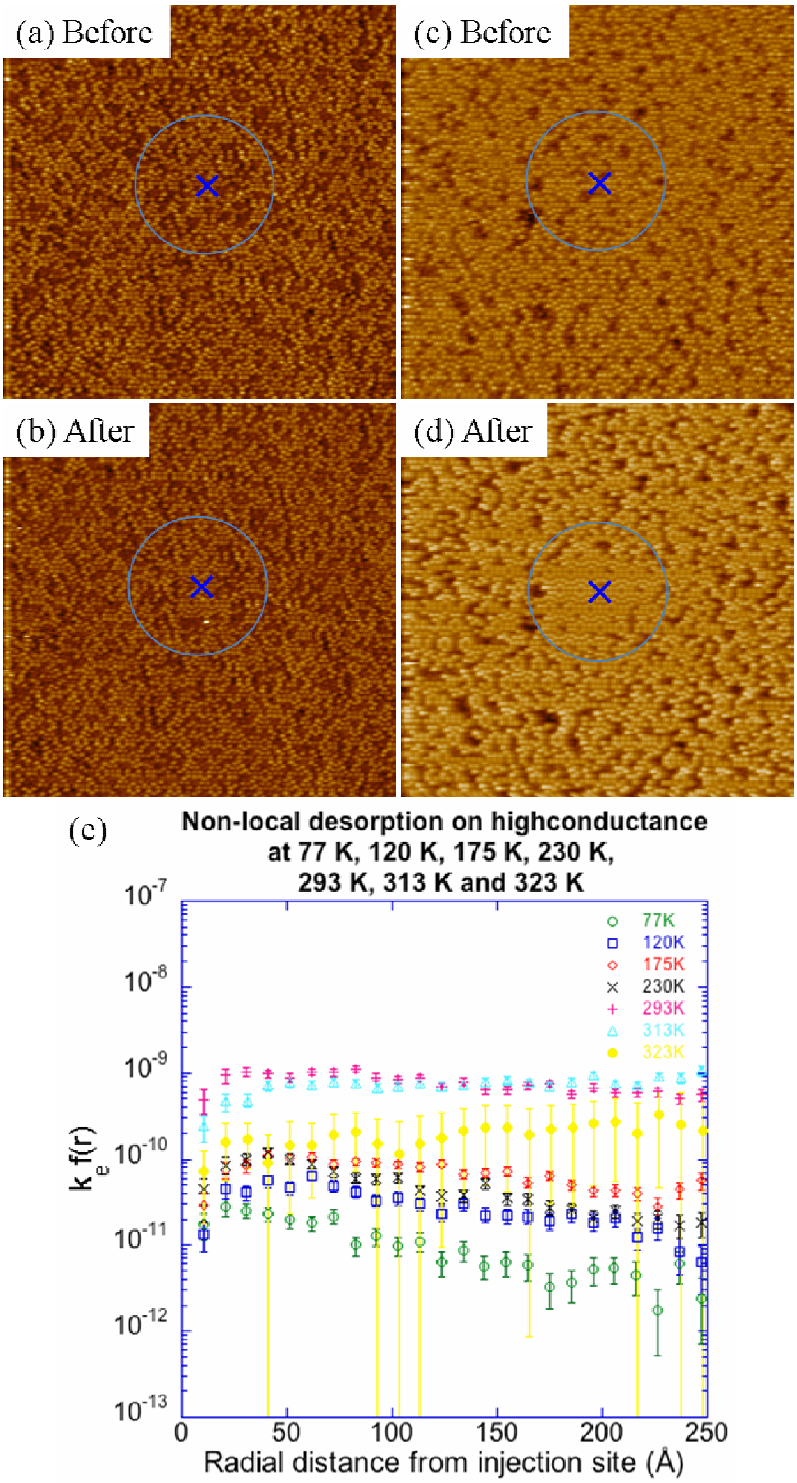

Figure 4.15 STM images before (a) and after (b) the electron injection at 77 K (images taken at 1.0 V, 100 pA, 51.2 nm × 51.2 nm). STM images before (c) and after (d) the electron injection at 230 K (images taken at 1.0 V, 100 pA, 51.2 nm × 51.2 nm). The blue crosses indicate the injection site. (e) Non-local desorption probability as a function of the radius from the injection site on the high conductance sample (electron injection at 2.7 V, 800 pA, 8 s for 293 K, 313 K and 323 K; electron injection at 2.7 V, 800 pA, 80 s for 77 K, 120 K, 175 K and 230 K). Different colour symbols represent experiments performed at different temperatures.

Furthermore, the decay length increases as the temperature increases as shown in Fig. 4.16. Fig 4.16 (a) shows the data set chosen for plotting the decay length as a function of the temperature. Due to the presence of the suppression region close to the injection site, the data at 77 K are chosen from 20 nm, then the data at 120 K, 175 K and 230 K are chosen from 30-40 nm; and the data at 293 K are chosen from 75 nm. The decay length is calculated from the exponential fitting function $k_e exp(-r/\lambda)$ which indicates radial decay of the surface current according to ref. [40], as shown in Fig. 4.16 (b). In Fig. 4.16 (b), the decay length increases as the temperature increases. Thus it is evident that the hot electron transport (the electron injected from the tip) is enhanced as the temperature increases. Also the scale of the decay length (from 100 nm to 300 nm) is similar with that (170 nm) in the previous study [98]. However, to our best knowledge, we have not been able to find the temperature dependence of the hot electron scattering length, which could explain our results.

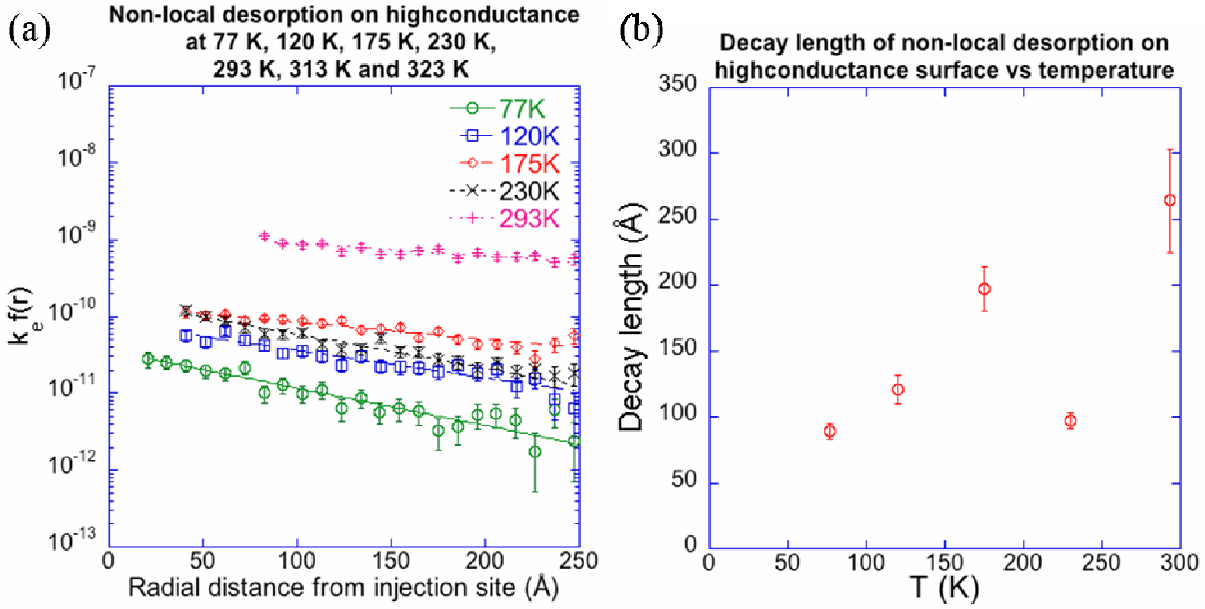

Figure 4.16 (a) Non-local desorption probability data set chosen from Fig. 4.15 (e) for plotting the decay length as a function of the temperature. (b) The decay length as a function of the temperature on the high conductance sample.

On the other hand, from the measurements shown in Fig. 4.15, there is a clearly temperature dependence of the desorption rate in the non-local desorption process. In order to gain more information of the non-local desorption process, we draw the Arrhenius plot, based on the following equations. According to the rate equation of non-local desorption, we have

$$\frac{dN}{dt} = \frac{I}{e} tNA \exp^{-\frac{E}{k_B T}} \tag{4.3}$$

where I is the injection current, e is the charge of a electron, t is the time of electron injection, N is the total number of molecules on the surface within the analysis region, A is the pre-exponential factor, E is the activation energy, k_B is Boltzmanns constant and T is the temperature. By rearranging the equation and integrating on both sides, we have

$$LnN = \frac{t^2}{2}\frac{I}{e} A \exp^{-\frac{E}{k_B T}} + B \tag{4.4}$$

where B is the constant generated during the integration. Since at t=0, $LnN_{(t=0)}$=B, we can rearrange the equation as

$$Ln\frac{N}{N_0}\left(\frac{2e}{t^2 I}\right) = A\exp^{-\frac{E}{k_B T}} \tag{4.5}$$

where N_0 is the number of molecules at $t=0$.

Fig. 4.17 is generated by plotting all the measurements done at different temperatures according to the equation (4.5), where the activation energy E can be generated from the fitting curve in the graph. In Fig. 4.17, we can see two regions; one is measurements done at low temperatures on the right and the other is measurements done at high temperatures on the left. At low temperature region, the rate of non-local desorption decreases exponentially as the temperature decreases; an activation energy $E=16.7\pm4.8$ meV can be acquired from the fitting curve. This energy is much lower than the stretching mode of C-Si bond formed upon the chlorobenzene chemisorption on the Si(111)-7×7 surface together with the other vibrational modes of chlorobenzene on Si(111)-7×7 [89]. However, this number is quite close to the energy of surface phonons on adatom sites, which are around 6 to 10 THz (24 to 41 meV) [99]. Since the chlorobenzene molecule is bonded to the surface via the adatom site, and these phonons have an in-phase vibration fashion along the [111] direction that may help the chlorobenzene from desorbing from the surface, we tentatively propose that the non-local desorption chlorobenzene process is facilitated by surface phonons activated by the thermal energy at low temperature. In contrast, an activation energy $E=162\pm6$ meV can be calculated at the high temperature region in Fig. 4.17. We speculate that another vibrational mode is activated as the temperature increases. It may be from the C-Si stretching mode (~72 meV), where the energy from the injection electron is first stored and then couples to the C-Si streching mode. Or it maybe from the stabilisation of the negative ion resonance, where its lifetime increases and then couples to the chlorobenzene desorption channel. However, as

mentioned above, our results indicate that non-local desorption is hindered under the tip and this effect is greater at higher temperatures, i.e., 313 K and 323 K. Thus it is difficult to evaluate the activation energy and the activation mode at high temperature region based on the data we have acquired so far.

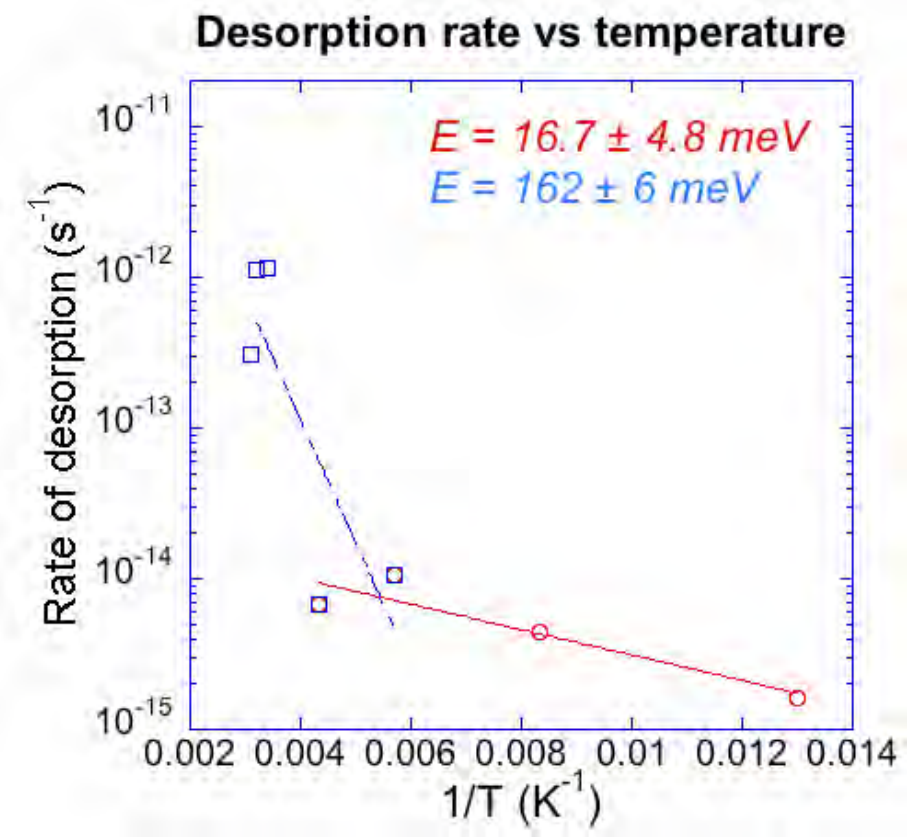

Figure 4.17 Arrhenius plot of the rate of non-local chlorobenzene desorption process. The red dots on the right side represent the measurements performed at 77 K, 120 K, 175 K and 230 K together with the fitting curve in red. The blue dots on the right side represent the measurements performed at 175 K, 230 K, 293 K, 313 K and 323 K together with the fitting curve in blue.

4.5 Conclusion

Through the STS investigation, a typical rest atom state at -0.8 V is found to be missing after

the chlorobenzene adsorption. This provides the direct evidence of the rest atom bonding to the chlorobenzene for chlorobenzene adsorption. From STS curves, a state at -1.2 V over the adatom site is found to match well with the previous established chlorobenzene desorption threshold, and is attributed to the π state causing the desorption. The non-local chlorobenzene desorption experiments across the surface step show that steps of up to 5 layers seems to have at the most small effect to the non-local desorption process and the non-local desorption may favour the "uphill" process rather than the "downhill" process. Combining these results, it indicates that the electron may not travel through the certain layer beneath the surface, but may in fact travel into the bulk and then scatter back to the surface to cause the reaction. Temperature dependent non-local desorption experiments show that the desorption probability increases as the temperature increases, and the decay length of non-local desorption increases as the temperature increases. Finally, we find that the non-local desorption process may be facilitated by the surface phonon over adatom sites at low temperature, and may be facilitated by the vibrational mode.

Chapter 5 UHV STM study of polychlorinated biphenyl (PCB) on the Si(111)-7×7 surface

This chapter presents the investigation of polychlorinated biphenyl molecules (PCB) (see Fig. 5.1) on the Si(111)-7×7 surface, combining imaging, manipulation and spectroscopy of these molecules by STM. The chapter is divided into four sections. The first section outlines the motivation for this work and provides a general introduction. The second section presents the STM investigation of the PCB molecule adsorbed on Si(111)-(7×7). The third section discusses STM manipulation of the PCB molecule and the related STS investigation of the mechanism of the manipulation. The final section gives the conclusions drawn from these experiments, including a discussion of various reactions induced by electron injection into different sites of the molecule and the corresponding adsorbate states. The main result of this work was published in Journal of American Chemical Society, T. L. Pan, S. Sakulsermsuk, P. A. Sloan, and R. E. Palmer, Site- and Energy-Selective Intramolecular Manipulation of Polychlorinated Biphenyl (PCB) Molecules. *J. Am. Chem. Soc.*, **133**, 11834 (2011) (see appendix).

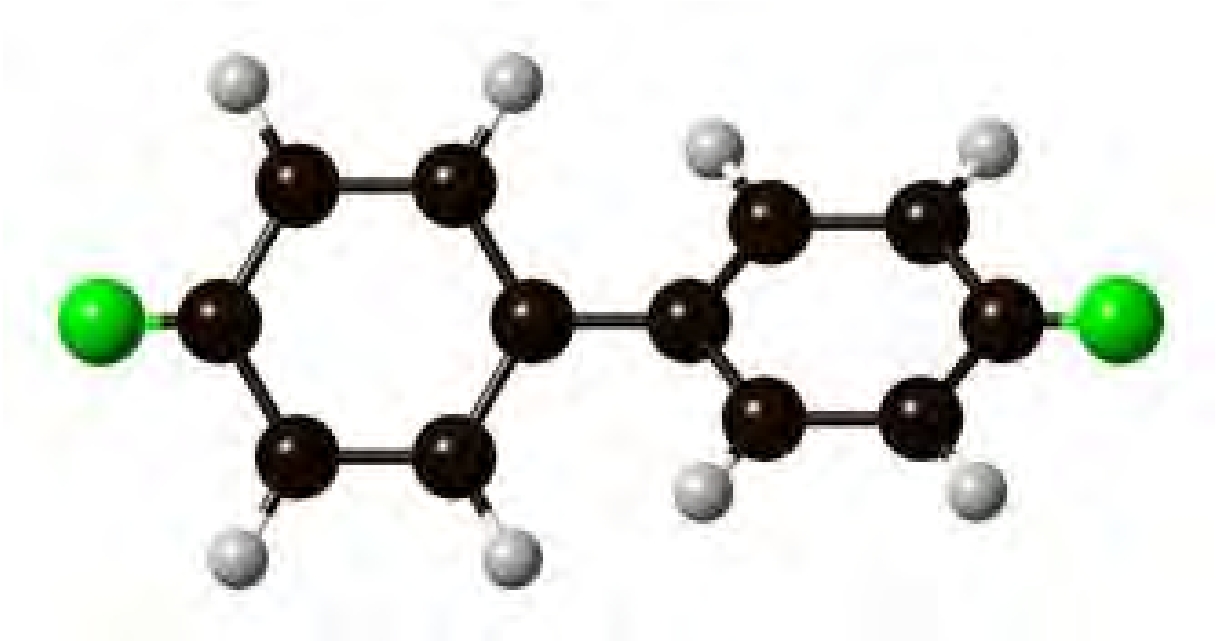

Figure 5.1 A schematic picture of 4, 4'- dichlorobiphenyl molecule. White balls represent hydrogen atoms, black balls represent carbon atoms and green balls represent chlorine atoms. Due to the twist angle 40° of the biphenyl rings with respect to each other [100], the right phenyl ring is shown at a rotated angle.

5.1 Introduction and motivation

PCB molecules are of great interest to many researchers due to the widespread use of these chemicals in industry [101] and their persistence within the environment together with the great danger and harm caused by them [101, 102]. Thus it is important to have a better knowledge of these molecules, although "real world" considerations are somewhat removes from UHV STM.

PCB molecules are interesting here for the reason that it is a more complex molecule than chlorobenzene, yet many similarities with chlorobenzene. It can be loosely viewed as a "twin pack" of chlorobenzene molecules. From previous studies of chlorobenzene, two main dynamical processes induced by STM can take place, desorption and C-Cl bond dissociation.

Since the PCB molecule is more complex than the chlorobenzene molecule, besides the possible desorption and dissociation reactions, more reaction channels may well exist. Also, due to the presence of two phenyl rings, two spatially separated electron injection positions are available. This provides the possibility of inducing manipulation outcomes dependent on injection site as well as the energy dependence. Furthermore, due to the similarity of the PCB molecule to the chlorobenzene molecule, we can compare STM induced desorption and dissociation in PCB to build on the published work on STM induced chlorobenzene desorption [41, 42, 61, 83, 103] and induced dissociation [61, 62].

5.2 STM study of PCB adsorptionon on the Si(111)-7×7 surface

The molecule studied for this experiment is 4, 4'- dichlorobiphenyl (as shown in Fig. 5.1). It is also known as PCB No.15. For convenience in this thesis, the 4, 4'- dichlorobiphenyl will be recorded simply as PCB. The chemical formula of this molecule is $C_{12}H_8Cl_2$, the length of the molecule is ~6 Å, the molecular weight is 222.8 amu and the melting point is 142~145 ℃ [104]. As mentioned in section 5.1, we chose the 4, 4'- dichlorobiphenyl molecule due to the similarity of this molecule to the chlorobenzene molecule, and due to its symmetry. Furthermore, among all congeners of dichlorobiphenyls, it has the highest vapour pressure, which will ease the deposition process.

The PCB deposition process has been described in detail in section 3.1.5.2. In order to achieve a desired deposition density, different deposition parameters have been tested by my colleague Dr. Sumet Sakulsermsuk. Generally, a dose at ~5×10^{-9} torr for 2-3 s will produce a

coverage of less than 0.8 PCB molecules per Si(111)-7×7 unit cell, which is the approximate density for the latter manipulation experiments. Fig. 5.2 shows a typical STM images of the Si(111)-7×7 surface after PCB dosing with various features indicated by red circles.

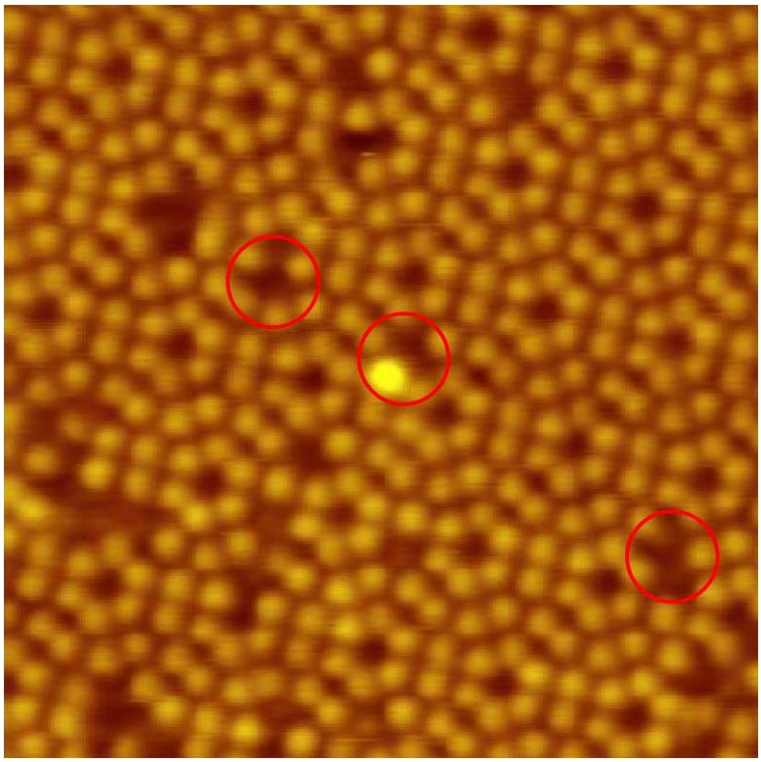

Figure 5.2 An STM image (1.5 V, 50 pA, 15 nm × 15 nm) shows three main features (indicated by red circles) observed on the Si(111)-7×7 surface after the PCB deposition.

Three main features observed are indicated by blue circles in Fig. 5.3, (a) single dark feature, (b) dark-dark feature and (c) bright-dark feature. The single dark feature, exhibiting a missing adatom, accounts for ~71% of total post PCB deposition features, dark-dark feature is ~23%; the most interesting feature is the bright-dark feature, although it only represents ~6% of features. It consists of a dark spot (akin to a missing adatom) and a neighbouring bright spot. This bright-dark feature looks roughly the same from +1 V to +2.6 V, except that the bright spot grows slightly brighter as the bias voltage is increased. Finally and most rarely, another

feature, which is similar to the bright-dark feature, can also be found on the surface. This feature possesses one or two "fuzzy" striped bright spots next to the dark spot. The stripe appearance implies that this feature is unstable. It is believed to undergo a switching reaction process between two bonding configurations.

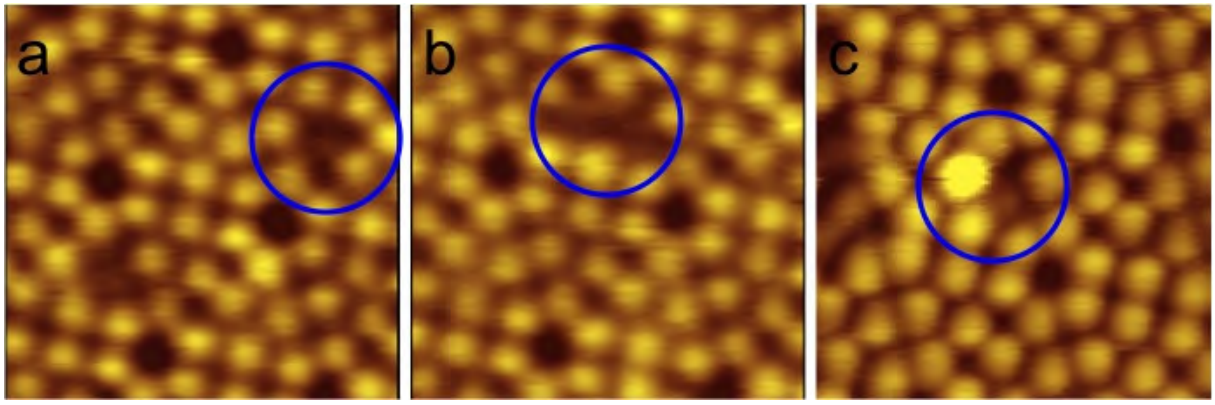

Figure 5.3 Detailed STM images of three main features observed after the PCB deposition (1.5 V, 20 pA and 6 nm × 6 nm). (a) The single dark feature, (b) the dark-dark feature and (c) the bright-dark feature.

As mentioned above, the PCB molecule can be simply viewed as a "twin pack" of chlorobenzene molecules. From previous studies [41], a single chlorobenzene molecule images as a missing adatom, as shown in Fig. 5.4 (a), upon chemisorption on the Si(111)-7×7 surface forming a di-σ bonding geometry. Due to the similarity between the PCB molecule and the chlorobenzene molecule, it is reasonable to hypothesise that one phenyl ring of the PCB molecule will form a similar di-σ bonding geometry on the surface and image as a missing adatom. Thus the dark spot of the bright-dark feature should correspond to a chemisorbed ring of the PCB molecule. On the other hand, based on the structure of the PCB molecule and the Si(111)-7×7 surface (the distance between the two furthest carbon atoms inside the PCB molecule is 6 Å, while the distance between the two neighbouring adatoms is

7.7 Å), it is geometrically unlikely that the other ring can also form the same bonding geometry. Then the bright spot of the bright-dark feature, we believe is due to the other ring in a "physisorbed" interaction with the surface. As shown in Fig. 5.4 (b), one chemisorbed phenyl ring of the PCB molecule forms covalent bonds with a rest atom and adatom pair (changing the local electronic structure), while the "physisorbed" phenyl ring of the PCB molecule only interacts weakly with the adatom of the surface beneath.

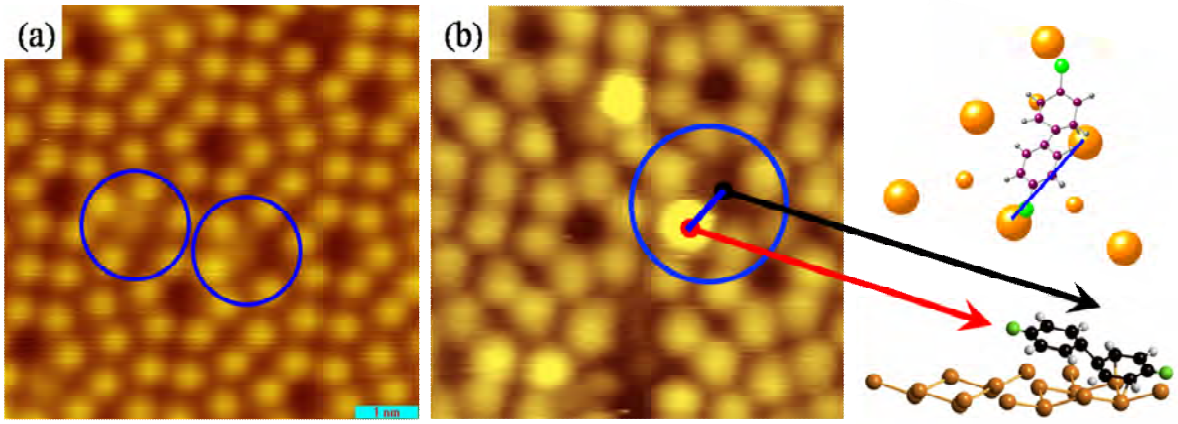

Figure 5.4 Comparison of the chlorobenzene molecule and the PCB molecule. (a) An STM image of the chlorobenzene molecule on the Si(111)-7×7 surface (1.9 V, 97.8 pA, 8 nm × 8 nm). Two chlorobenzene molecules indicated by blue circles. (b) An STM image of the PCB molecule on the Si(111)-7×7 surface (1.5 V, 20 pA, 6 nm × 6 nm), with the molecular model on the right. The blue circle indicates one PCB molecule with the blue line showing the relative position. The molecular model on the top shows the possible bonding geometry of the PCB molecule on the Si(111)-7×7 surface (top view) (Image from [79]). The molecular model on the bottom shows the possible bonding geometry of the PCB molecule on the Si(111)-7×7 surface (side view).

5.3 STM and STS study of PCB manipulation

5.3.1 STM study of PCB manipulation

Fig. 5.5 shows three main different reactions of the PCB molecule on the Si(111)-7×7 surface caused by electron injection. We name these reactions as follows: desorption, reconfiguration and "seesaw". Figs. 5.5 (a) to (b) show a complete desorption process. After a pulse applied to the PCB molecule, the molecule desorbed from the Si(111)-7×7 surface to reveal the clean surface beneath. This reaction also provides additional evidence that the bright-dark feature is one PCB molecule, since it leaves as a whole. The reconfiguration process is displayed in Figs. 5.5 (c) to (d). The former bright-dark feature is transformed into the latter double dark feature, indicating that the bonding geometry of the "physisorbed" ring is changed in this reaction. The newly generated dark feature of the original "physisorbed" ring is not always visible. In this case, as shown in Figs. 5.5 (e) to (f), the bright feature is gone and only the dark feature remains on the surface. However, in some cases, this invisible phenyl ring will recover again in subsequent STM images, showing that the reaction we see in Figs. 5.5 (e) to (f) is also a reaction process associated with the change of the bonding geometry of the "physisorbed" ring. Thus we take the phenomenon in Figs. 5.5 (c) to (f) into one reconfiguration process. The last reaction is the "seesaw" process shown in Figs. 5.5 (g) to (i). The former bright feature turns dark and the dark feature turns bright; afterwards the bright feature appears to swap between two neighbouring adatom sites adjacent to the new dark feature. This process may originate from the detachment of one phenyl ring and the re-adsorption of the other phenyl ring of the PCB molecule. The new-made adsorption configuration appears to be thermally unstable, switching between bonding configurations.

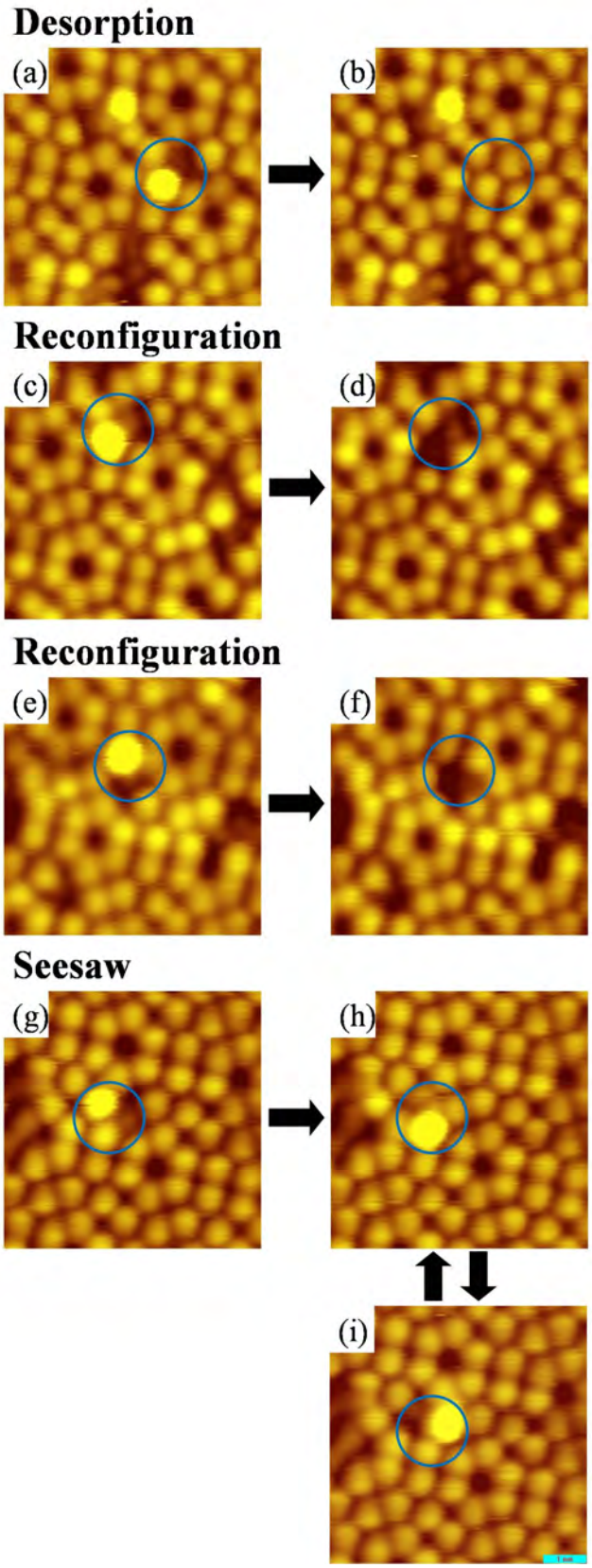

Figure 5.5 STM images (1.5 V, 20 pA, 6 nm × 6 nm) show different reactions that occurred after electron injection. The STM image (a) before and (b) after the PCB desorption process; (c, e) before and (d, f) after the PCB reconfiguration process; (g) before and (h, i) after the PCB seesaw process. Blue circles indicate relevant positions on the Si(111)-7×7 surface.

In order to acquire a deeper understanding of these reactions and to investigate the underlying mechanisms, systematic manipulation experiments have been performed. To prepare the STM, the tip was modified by applying positive or negative pulses until STM images of the Si(111)-7×7 surface together with the bright-dark feature of the PCB molecule imaged similarly to Fig. 5.2 (b). By making use of the tracking function of the RHK XPMPro programme, a target bright-dark molecule was "locked". Then STM tip was exactly positioned over the centre of either the bright side or the dark side of the target molecule followed by a 2s pulse applied at certain bias voltage. The outcome was then measured in a subsequent scan at a passive voltage +1.5 V, 20 pA. The pulse was applied 5 times, starting from a low bias voltage of +1.5 V, and if no reaction occurs, the pulse voltage was increased in increments of 0.1 V until a reaction occurred. In a few cases, some events were observed other than three main reactions, e.g., a large feature suddenly appears after the pulse, which is thought to be some contaminant, such as an oxide dropped from the tip to the surface. These few undesired incidents are discarded from the following reaction yield calculations. The reaction yield measured here is the probability that a certain reaction occurs out of all the 2s electron injection experiments at a certain bias voltage over a certain site (bright or dark). With the help of the tracking function, the injection site is within 1.6 Å of the centre of the site. Furthermore, we combine the neighbouring voltage data points, e.g., combining the data at 1.5 V and 1.6 V to generate one data standing for the region between 1.5 V to 1.6 V, in order to reduce the error bar. 410 PCB molecules were studied during this experiment.

Fig. 5.6 shows the reaction yield of three competing reactions as a function of the electron injection site and as a function of the bias voltage. Fig. 5.6 (a) shows the yield of the total

reaction (the sum of all the three main reactions), whereas Figs. 5.6 (b) to (d) shows that of the individual reaction channels. In Fig. 5.6 (a) we can clearly identify two energy regimes, i.e., below and above +2.5 V. Below +2.5 V, the probability of a reaction triggered by the electron injection into the dark side of the PCB molecule is on average higher than that into the bright side of the PCB molecule. On the other hand, when the bias voltage is increased above +2.5 V, the probability of a reaction triggered by the electron injection into the bright side of the PCB molecule is greatly increased, and much higher than that into the dark side of the PCB molecule. Differences of the reaction yields among these three channels can be clearly seen after they are plotted separately in Figs. 5.6 (b) to (d). The reaction probability of the desorption process as a function of the electron injection site and as a function of the bias voltage is shown in Fig. 5.6 (b), that of the reconfiguration process is shown in Fig. 5.6 (c) and that of the "seesaw" process is shown in Fig. 5.6 (d). Through the comparison, we can clearly observe that for the region below +2.5 V, only the desorption process occurs and the channels for the other two reaction processes are closed. Furthermore, the probability of desorption is favoured when the electron injects into the dark side rather than the bright side. According to our previous proposed adsorption geometry, the dark side is the site where the phenyl ring chemisorbed onto the surface, forming bonds with silicon atoms, and acts like an anchor for the PCB molecule. As a consequence, it is reasonable that electrons injected into this side will cause the most efficient bond cleavage process and release the PCB molecule from the surface. The yield of the desorption process starts to decrease for the region above +2.5 V, since the other two channels open, especially for the reconfiguration process. The probability of the reconfiguration process induced by the electron injected into the bright side of the PCB molecule is much higher and increases much faster than that into the dark side of

the PCB molecule. Based on our proposed adsorption geometry, the reconfiguration means the changing of the bonding configuration of the "physisorbed" ring with the surface. Therefore we suggest that the electron localization on the "physisorbed" ring after the electron injection into the bright side causes this strong interaction with the surface. Additionally, the low probability of the reconfiguration caused by the electron injection into the dark side of the PCB molecule might indicate that some electrons injected into the dark side of the PCB molecule seem to leak to the bright side and trigger the reconfiguration process.

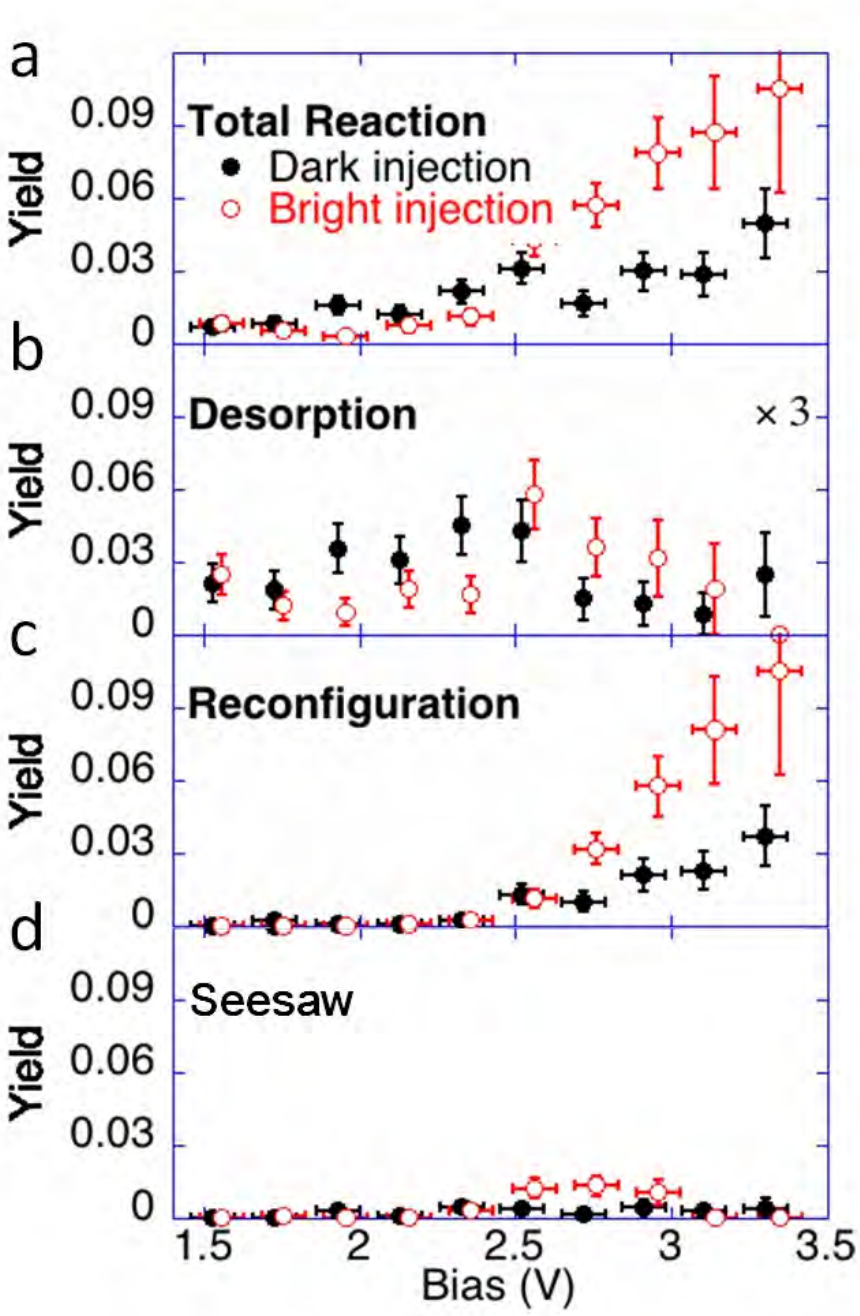

Figure 5.6 Probability of atomic manipulation of PCB on the Si(111)-7×7 surface as a function of voltage and intramolecular injection site. (a) Total reaction yield, (b) desorption yield, (c) adsorption reconfiguration yield and (d) seesaw yield as a function of the bias voltage. Red circles stand for the injection into the bright side of the molecule. Black dots stand for the injection into the dark side of the molecule. Red circles are displaced by 0.05 V for clarity. Yield means the probability that a reaction occurs averaged over all (2 s injection) experiments. The data are binned in 0.2 V intervals.

5.3.2 STS study of PCB manipulation

To cast more light on different behaviours of these reactions, STS measurements have been performed. The $(dI/dV)/(\overline{I/V})$ spectra were measured from 0 V to 3.5 V, with the tip ramping 1 Å/V away from the surface. A programme written by Dr. Peter Sloan is used to generate the STS curves from the variable gap *I-V* curves as mentioned in section 3.3.1. A decay constant (κ = 1 Å^{-1}) is used in the calculation to convert the variable gap *I-V* curves to the constant gap *I-V* curves. The *I-V* spectra were recorded over both the bright side and the dark side of the bright-dark feature for 100 different PCB molecules. The *I-V* spectra over adatoms on the clean Si surface have also been acquired for comparison. The target molecule would first be found and the STM tip would then be located on top of the target in the same fashion as that in the manipulation experiments (as shown in Fig. 5.7). When taking the spectra over the dark side, the contour difference between the dark side and the bright side would first be measured and then be applied to the retraction of the STM tip before acquiring the *I-V* spectra. This was to ensure the spectra taken over the dark side and the bright side shared the same physical height with respect to the underlying Si(111)-7×7 surface. The region from 3.3 V to 3.5 V is excluded due to distortions induced by the numerical differentiation procedure from the calculation.

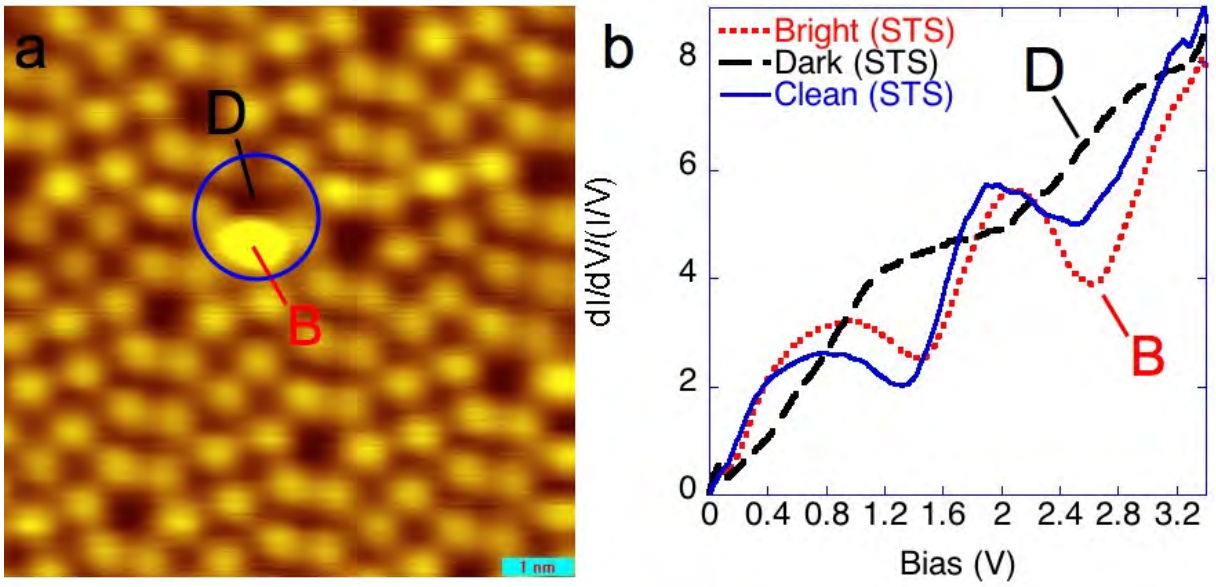

Figure 5.7 (a) An STM image shows the position where the STS data was acquired (+1.5 V, 20 pA). (b) STS curves taken at different sites. The red dotted line stands for the STS curve acquired over the bright side as labelled "B". The black dotted line stands for the STS curve acquired over the dark side as labelled "D". The blue line stands for the STS curve acquired over the adatom on the clean surface.

Different electronic states are evident from comparison of STS measurements of different sites of the PCB molecule and the corresponding clean site on the surface in Fig. 5.7 (b). By comparing between STS on the dark PCB site and a clean adatom site, we find that the typical adatom state of the clean surface at ~0.5 V is lost, and a new shoulder appears between +1.0 V and +2.2 V. This broad feature roughly matches with the area in the desorption yield data where the desorption yield of the dark side is higher than that of the bright side. We propose that this broad feature may be the remnant of the π* state on the dark side of the PCB molecule, where the injected electron causes the desorption process in a similar fashion as chlorobenzene. On the other hand, from the bright site of the PCB (red curve), there is a state that starts from +2.5 V and largely increases for the STS curve taken over the bright side of the PCB molecule. This red curve somewhat mimics the STS taken over the clean surface, but its state starting from +2.5 V is steeper than that of the blue one. This again matches the

threshold for the reconfiguration process at +2.5 V. We propose that the transient occupation of the injected electron into this state on the bright side of the PCB molecule accounts for the rapidly increased reconfiguration yield for the bright side injection and the slowly increased reconfiguration yield for the dark side injection. These features in STS curves also support our previous hypothesis that the dark side is the chemisorbed ring (which significantly changes the electronic structure of the surface) and the bright side is the physisorbed ring (which interacts little with the surface).

5.4 Conclusion

We have deposited PBC molecules onto the Si(111)-(7×7) surface at room temperature and discovered that, by controlling the electron intra-molecular injection site and energy, three different reaction channels can be triggered. We find the desorption process is preferred for the dark side injection over the bright side injection below +2.5 V, and by further comparing the STS curves acquired over the bright side, a broad electronic state between +1.0 V and +2.2 V appears to account for this phenomenon. We also find that above +2.5 V, two other reaction channels open and the desorption channel is suppressed. Among them, the reconfiguration process dominates and is preferred for the bright side injection. This appears to originate in a state that starts at +2.5 V in the STS curve of the bright side. Through these experiments, we show that by choosing the position (electron injection site) and the energy (applied bias voltage), we can selectively enhance or reduce the rate of a particular reaction.

Chapter 6 AFM and STM study of mucin on the HOPG surface

This chapter concerns the atomic manipulation of the bio-molecule Pig Gastric Mucin (PGM) on the bare and gold cluster-decorated highly ordered pyrolytic graphite (HOPG) surfaces using scanning probe microscopy (SPM) under the dehydrated state and the liquid state. It consists of four sections, the first being a motivation and general introduction. The second illustrates the results acquired in the dehydrated state on the bare HOPG surface by both the AFM and STM, showing that the mucin cannot be scanned without being swept away by the AFM tip and the sequential mechanical manipulation achieved by the STM under this condition. The third section shows the results acquired in the liquid state on both the bare and gold cluster-decorated HOPG surface by the AFM, demonstrates that the mucin molecule can be firmly attached to the gold cluster-decorated surface, providing an ideal surface for the future dissociation experiment. The final section gives the conclusions of these experiments and suggests potential future experiments. This main result of this work was accepted in G.I.T. Imaging & Microscopy, T. L. Pan, P. A. Sloan, and R. E. Palmer, Towards Manipulation of Single Proteins: Scanning Probe Microscopy in a Physiological Environment, *G.I.T. Imaging & Microscopy*. (see appendix).

6.1 Introduction and motivation

The disulphide bond plays a very important role in protein function. Among different interactions to maintain protein structure (hydrogen bonds, Van der Waals interactions, hydrophobic effects, etc.), the disulphide bond is the only covalent bond, thus it is of great interest to many researchers. Previously, the disulphide bond has been dissociated under UHV conditions by injecting electrons through the STM tip. In the experiment performed by Maksymovych *et al.* [65], in order to prepare methanethiolate (CH_3S) on the Au(111) surface, dimethyl disulphide (CH_3SSCH_3) was dosed into the UHV system. Afterwards, by using the pulse provided by the STM, dimethyl disulphide (CH_3SSCH_3) was dissociated into two methanethiolate (CH_3S) species; they found the threshold at around 900 mV. Such processes are illustrated in Fig. 6.1.

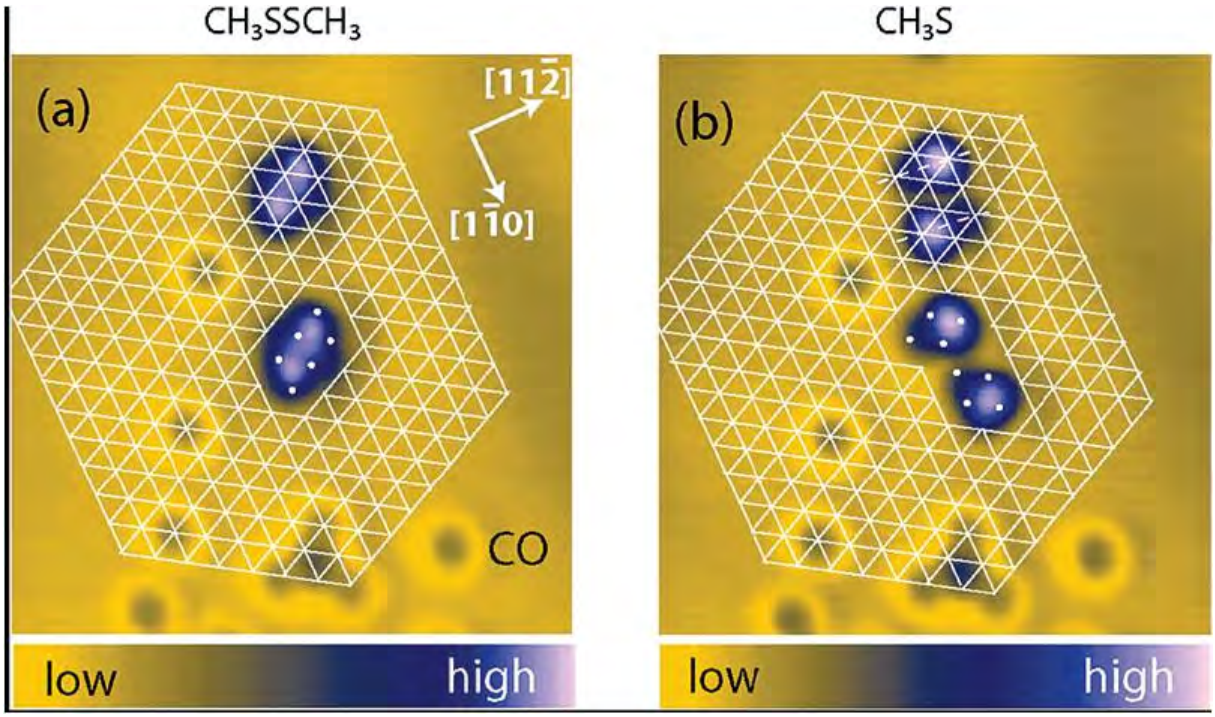

Figure 6.1 STM images before (a) and after (b) the dissociation process from dimethyl disulphide (CH_3SSCH_3) to methanethiolate (CH_3S) on the Au(111) surface. Dimethyl disulphide is shown as a blue elliptically shape double dots in (a) and methanethiolate is shown as two round dots in (b). The matrix indicates the Au(111) lattice. (Images and caption modified from ref. [65])

Not just by injecting electrons, but also by using chemical reactions, a similar disulphide bond cleavage process can be realized on surfaces. In the experiments carried out by Brayshaw *et al.* [105] they investigated the ocular mucin molecule in the physiological state on the gold surface (template-stripped gold (TSG) surface, which is atomically flat). The ocular mucin molecules imaged as coil like features under the tapping mode AFM as shown in Fig. 6.2 (a). By adding the disulphide bond reducing agent dithiothreitol (DTT), they found that part of the ocular mucin which was previously stabilized on the gold surface was removed due to the disulphide bond cleavage, while the rest of the molecule was still attached to the surface through the gold-cysteine bonds, as shown in Fig. 6.2 (b). The disulphide bond cleavage for bio-molecules by electron injection has not been performed so far. As a consequence, we chose mucin molecules as our target to begin exploring atomic manipulation of biomolecules by electron injection.

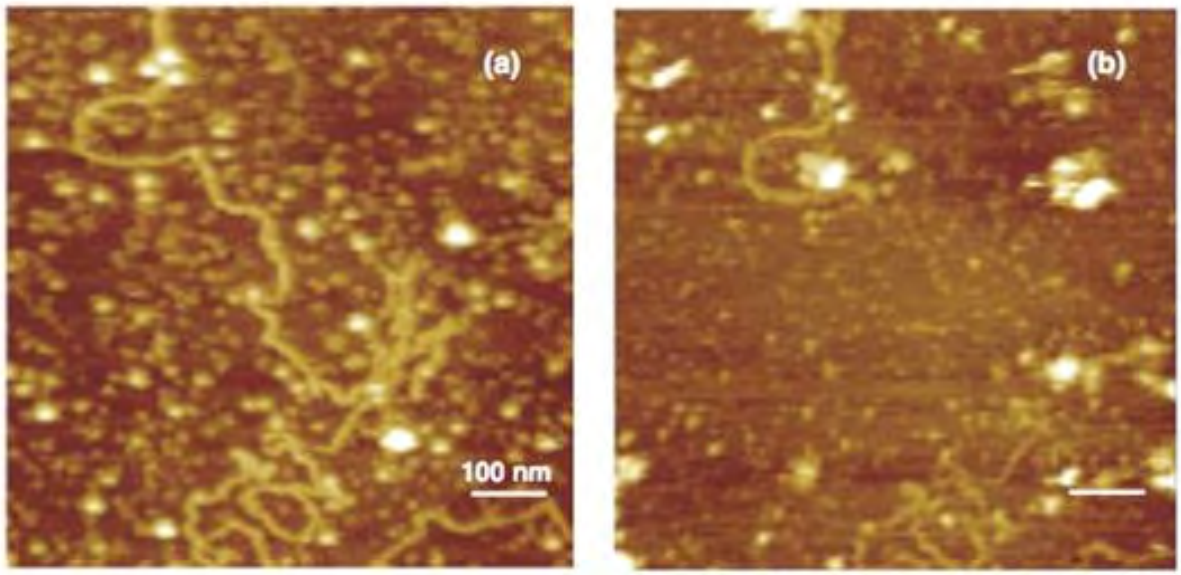

Figure 6.2 AFM images of the disulphide bond cleavage process of ocular mucin molecule in the physiological state on the gold surface, before (a) and after (b) adding 10 µl of 2 mM disulphide bond reducing agent dithiothreitol (DTT). The coil like feature in the images is ocular mucin molecule. (Images and caption modified from ref. [105])

Mucin is a member of a family of big and highly glycosylated proteins with high molecular weight (>10^6 Da) [106]. Mucin can be found on the surface of various organs, acting as a lubricating and protective layer. One of the unique properties of mucin is its ability to form gels [107, 108], e.g., gastric mucin forms layers on the stomach, preventing the stomach from suffering damage by its gastric acid.

Generally, the structure of the secretory mucins is similar (PGM is one of them) [109], it consists of two regions, PTS region and non-PTS region, as shown in Figs. 6.3 (a) and (b). The PTS region mainly comprises of three types of amino acids: proline ($C_5H_9NO_2$), threonine ($C_4H_9NO_3$) and serine ($C_3H_7NO_3$), and is highly glycosylated with O-linked oligosaccharides. This makes it present like a “bottle brush”. The non-PTS regions are rich in cysteine amino acids ($C_3H_7NO_2S$) and one very important domain called the C-terminal cystine knot domain also locates within these regions. The disulphide bonds will be formed

between these cysteine knot domains, giving another important property of mucin: polymerization. The mucin monomers can first form dimers and then connect into polymers, just like "sausages" as shown in Figs. 6.3 (c) and (d), and the final length can be up to micrometres. From the previous studies [110-113], a difference in height along mucin molecules has been observed by AFM, indicating the different width along the molecule (as it is a "bottle brush"). For PGM, the width of molecules can be from 20 nm to 100 nm, depending on the preparation procedure [114]. The monomer length is still unknown. However, it has been stated that the length of the whole molecular chain might be ~50 nm [115, 116]. For clarification and convenience, PGM will be written as mucin for short in the following discussion.

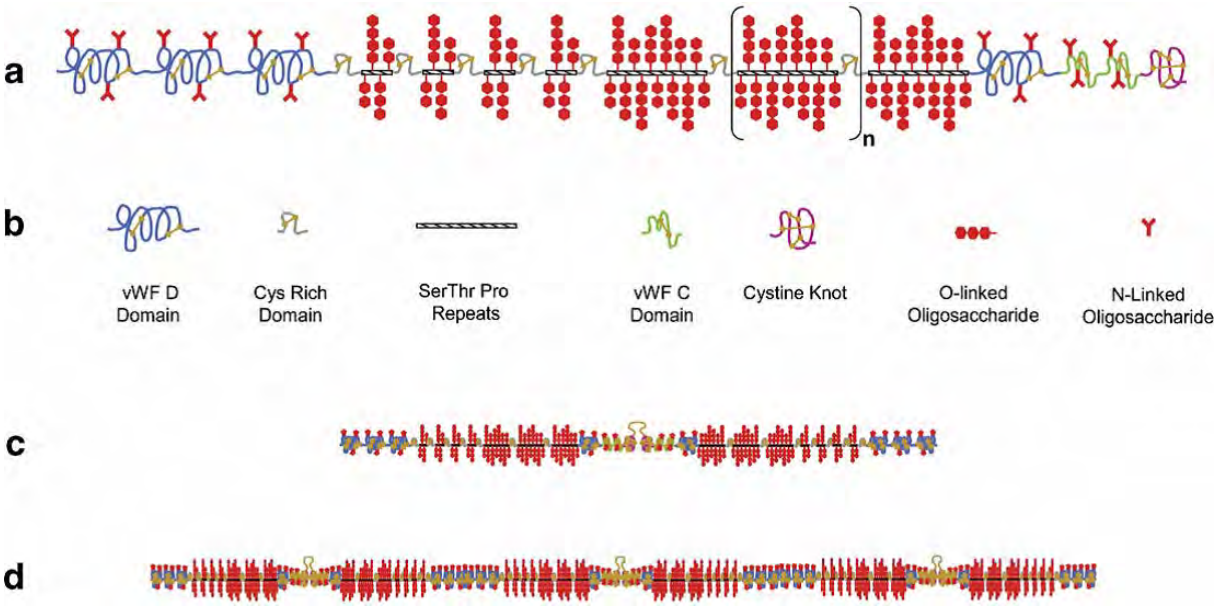

Figure 6.3 (a) The schematic picture of a PGM monomer. The parts with O-linked oligosaccharides are PTS regions, while the rest are non-PTS regions. (b) Symbols indicate different domains in (a). (c) A mucin dimer formed by two mucin monomers through the disulphide bond. (d) A mucin polymer formed by two mucin dimers through the disulphide bond. (Images and caption modified from ref. [117])

The mucin sample used in this experiment was purchased from Sigma-Aldrich: Mucin from

porcine stomach, Type II (M2378). The mucin was purchased as a dehydrated, slightly yellow powder. The HEPES ((4-(2-Hydroxyethyl)piperazine-1-ethanesulfonic acid) buffer solution used in this experiment was purchased from Sigma-Aldrich (HEPES solution 1 M, pH 7.0-7.6). The HEPES buffer solution could be used to maintain the pH value of the sample solution at around 7. The ultra pure water used in this experiment was prepared within our group. By diluting the mucin powder and (or) the HEPES buffer solution with the ultra pure water, different new stock solution was prepared. One such solution comprised mucin concentration of 0.2 mg/ml and HEPES concentration of 10 mM, one was with HEPES concentration of 10 mM and the other one was with mucin concentration of 0.2 mg/ml. These stock solutions could then be diluted with each other to prepare the sample solution at the desired concentration determined by the observation of the molecular density on the surface. For all mucin sample solutions with buffer, the HEPES concentration was always kept at 10 mM. Two types of surfaces were used in these experiments, bare HOPG surface and the gold cluster-decorated HOPG surface. The HOPG sample used in this experiment was purchased from Momentive (10×10×2 mm, grade ZYB, mosaic spread is 0.8° ± 0.2°). The gold cluster-decorated HOPG sample was prepared by Dr. Feng Yin, using our cluster source. In the previous studies [118-120], the size selected gold cluster-decorated HOPG surface has been demonstrated as a nice platform for immobilization the protein molecules onto the surface for AFM.

6.2 STM and AFM study of mucin in the dehydrated state

6.2.1 STM study of mucin adsorption on the bare HOPG surface

For the investigation of proteins by the SPM, different supporting substrates are used, e.g., mica, TSG, HOPG, etc. Mica is a group of the silicate, which possesses good basal cleavage property. It is widely used in protein research due to its simple preparation procedure, good flatness and the hydrophilic nature of the freshly cleaved surface. Since the oligosaccharide side chains of the mucin molecules are hydrophilic, mica is an ideal substrate for supporting and binding the mucin molecules. However, we aim to investigate the disulphide bonds within the mucin molecules against the injection of electrons, which requires the substrate to be conductive, unlike mica. TSG surface is conductive surface, possesses atomic flatness and the mucin molecule shows affinity for it. However, the mucin molecules bind to this surface by forming the gold-sulphur bonds, therefore most of the disulphide bonds are likely to break upon mucin adsorption on the surface. Thus, the easily prepared HOPG surface was chosen as our substrate. For each new experiment, a freshly cleaved HOPG surface was prepared by removing the outer layers several times using Scotch tape.

The experiment was first performed in the dehydrated state, since the STM provides an easy "click and go" method of acquiring the mucin molecule's morphology information and at the same time, electrons can be injected at a desired energy in the desired position with bias voltage applied, while the tip is scanning across the surface. Initially, an incubation-washing preparation protocol was adapted (where the mucin molecule was first incubated in the air on the surface for ~5 minutes before being washed by ultra pure water). Normally, under such

protocol the target molecules stuck to the surface remain, while salt from the buffer and the mucin molecules loosely bound to the surface were rinsed off. After the mucin molecule deposited on the bare HOPG surface, quite linear not coil-like features [105] could be observed on the surface, as shown in Figs. 6.4 (a) and (b) indicated by the black arrows and the blue ellipse. At low concentrations, these linear features were thin, with width only ~7 nm and height ~0.7 nm; in higher concentration experiments some other thicker features could be noticed, with width up to ~20 nm and height up to ~3 nm. Some of these linear features were stable, while others could be moved by the STM tip. These features were not found in the images acquired by tapping mode AFM in the liquid state in the previous study [113]. Due to the strange linear fashion of the features found in STM experiments, increasing concentration experiments were performed to examine whether such features were from mucin molecules or not. As the features were first acquired under an incubation-washing preparation protocol, the increasing concentration experiments were first carried out in the same way. However, the results from these experiments did not show a gradual increase in the numbers of linear features with gradually increased concentrations. Since there are not many binding sites for molecules except for surface defects, perhaps most of the unfirmly bound molecules were washed away before the scanning. Also the numbers of surface defects will not increase as the concentration of molecules, thus it did not show a gradual increase in the numbers of linear features. The increasing concentration experiments were then carried out in another way where the droplet of the mucin sample was left dried on the surface without washing. Counter-intuitively, except for some extremely large features on the surface as shown in Figs. 6.4 (c) and (d), no obvious increase in the number of linear features could be observed.

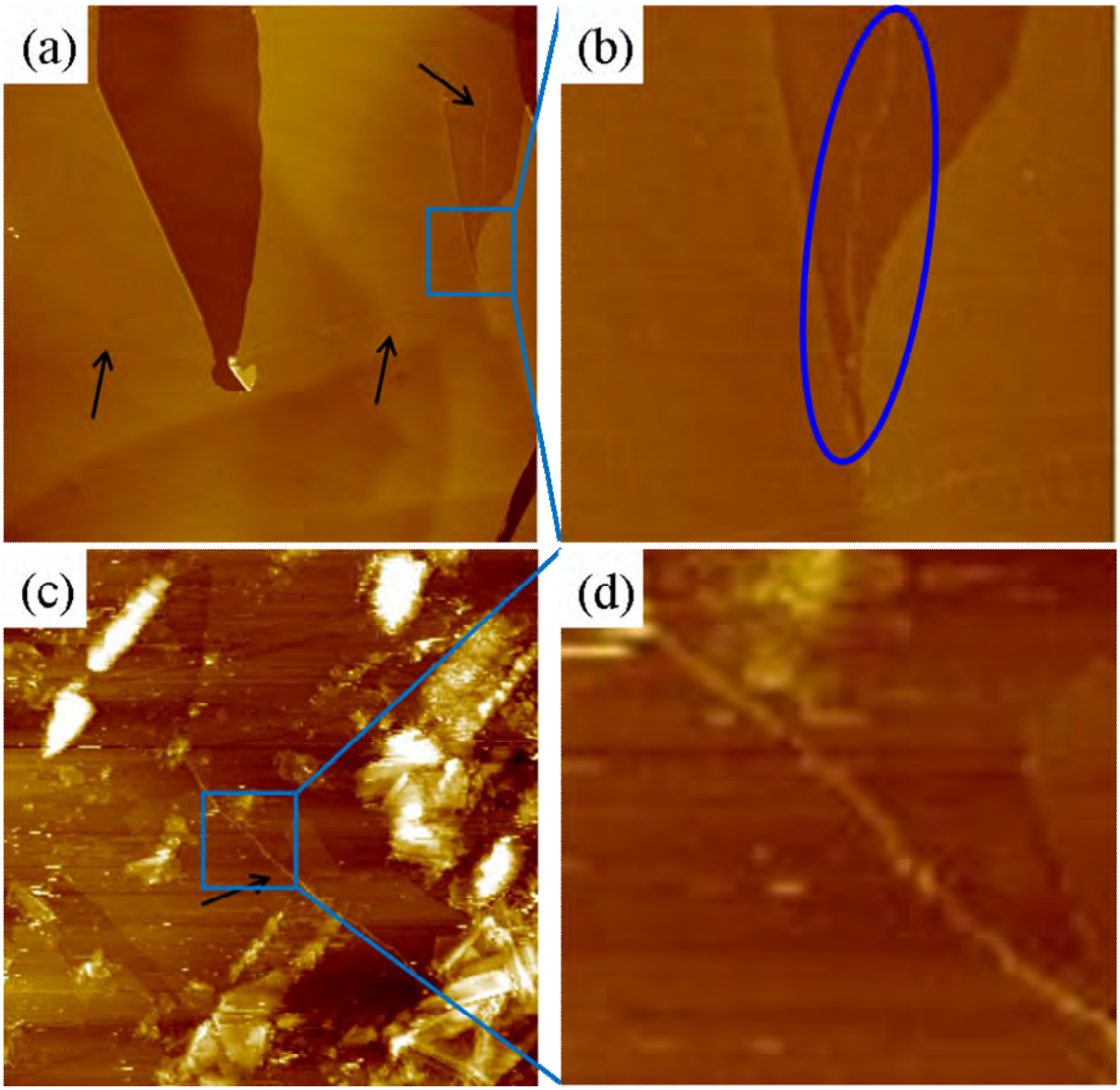

Figure 6.4 (a) STM images of 4 μg/ml mucin sample with buffer dried on the bare HOPG surface after washing (1 μm × 1 μm, 800 mV, 200 pA). (b) Magnified STM image of (a). (c) STM images of 2 μg/ml mucin sample with buffer dried on the bare HOPG surface without washing (1 μm × 1 μm, 800 mV, 200 pA). (d) Magnified STM image of (c). Black arrows and the blue ellipse indicate the linear features on the surface.

6.2.2 AFM study of mucin adsorption on the bare HOPG surface

As shown in Fig. 6.4, both STM images were taken with roughly the same mucin concentrations for different preparation protocols. From the comparison of images taken at

different concentrations, whether pre-washed or not, no greatly increase in the number of linear features could be noticed. This leads to a question of whether the features we observed in the STM were really mucin molecules. In order to solve this problem, tapping mode AFM was used to check the samples prepared under similar concentrations and the same protocols used before. Strikingly, the features observed under tapping mode AFM were completely different from that under the STM, as shown in Fig. 6.5.

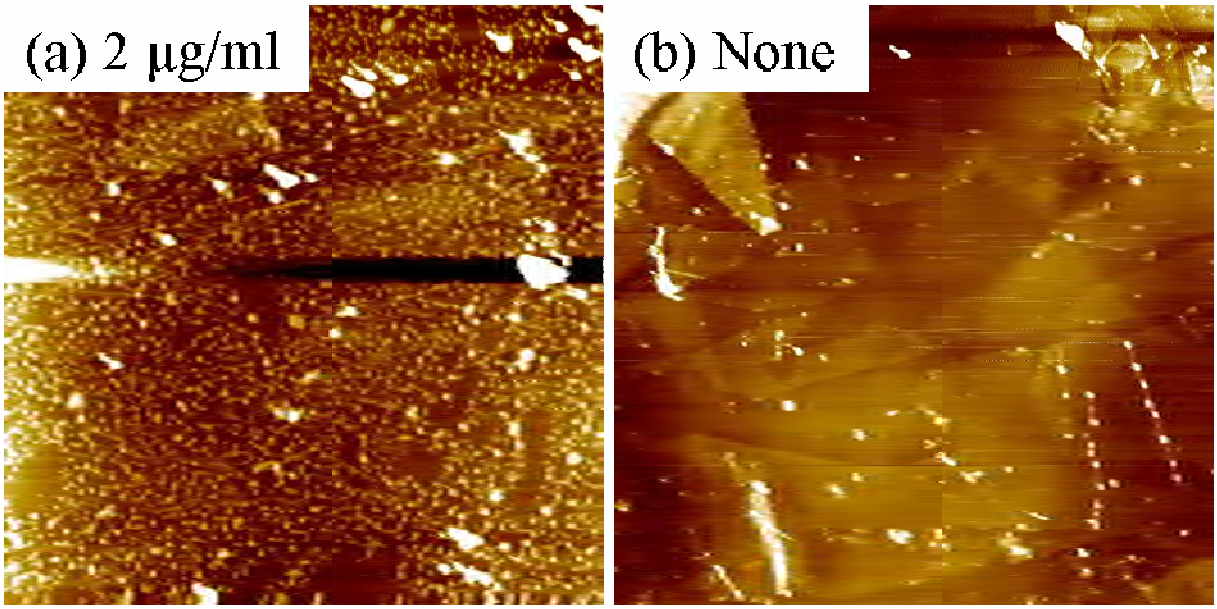

Figure 6.5 (a) Tapping mode AFM image of 2 µg/ml mucin sample with buffer dried on the bare HOPG surface without washing (10 µm × 10 µm, z scale 10 nm). (b) Tapping mode AFM image of 10 mM HEPES buffer sample dried on the bare HOPG surface without washing (10 µm × 10 µm, z scale 10 nm).

Fig. 6.5 (a) was acquired with tapping mode AFM on the same bare HOPG sample as Fig. 6.4 (c), but the two images are dramatically different. In fact, as shown in Fig. 6.5 (a), there were dendritic features as well as small globular features on the surface. The small globular features were among network forming dendritic features, which had not been observed with the STM. Are these features from the mucin molecule? In order to confirm this, control

experiments have been performed. Fig. 6.5 (b) shows the image acquired on the surface for the sample that only contained the buffer solution without mucin molecules. Based on the comparison between Figs. 6.5 (a) and (b), these dendritic features as well as small globular features were missing in the buffer only sample surface, which indicates that they were not from the buffer solution.

Furthermore, in order to acquire more information about these features from mucin molecules and try to find a right coverage of mucin molecules on the surface where single mucin molecule can be resolved, experiments under different concentrations were performed, as shown from Figs. 6.6 (a) to (f). From Fig. 6.6 (b), in high molecular concentration conditions, mucin molecules tended to first form dendritic features and then formed small globular features at certain sites (most likely the defect sites). And as concentration increases, excessive mucin molecules started to aggregate at certain sites to form even bigger globular features, as shown in Fig. 6.6 (a). This process is due to their aggregation property at high concentration and low pH conditions [107]. Under the intermediate concentrations as shown in Figs. 6.6 (c) to (e), before the mucin molecules are enough to form network-like features, they started to aggregate along the steps and then form fibre like features. As the concentration decreases, the length and the width of fibre features reduced. What is important was that the single molecular feature appeared only in the lowest concentration in Fig. 6.6 (f). The height of these features was around 0.5 nm to 1.5 nm (different from the features found in the 1 μg/ml experiments where were around 5 nm as shown in Fig. 6.6 (c)), which matched that from the literature. Thus the fibre-like features found under the higher concentrations should be from assemblies of several mucin molecules after drying, rather than that from a single extended mucin molecule. These results together prove that these fibre-like features

observed with tapping mode AFM were indeed mucin molecules, consistent with observations in Fig. 6.5 (a). They also demonstrate that mucin molecules must be partially or completely cleared from the surface by both the washing and the STM scanning in the dehydrated STM experiments, leaving only mucin molecules that attached to surface defects. If only the features that attached to surface defects remained on the surface after the washing and the STM scanning, then the numbers of these "survivors" will be independent of the mucin concentration. Therefore, it will be no surprise to find that the increased concentration did not increase the numbers of linear features in STM experiments.

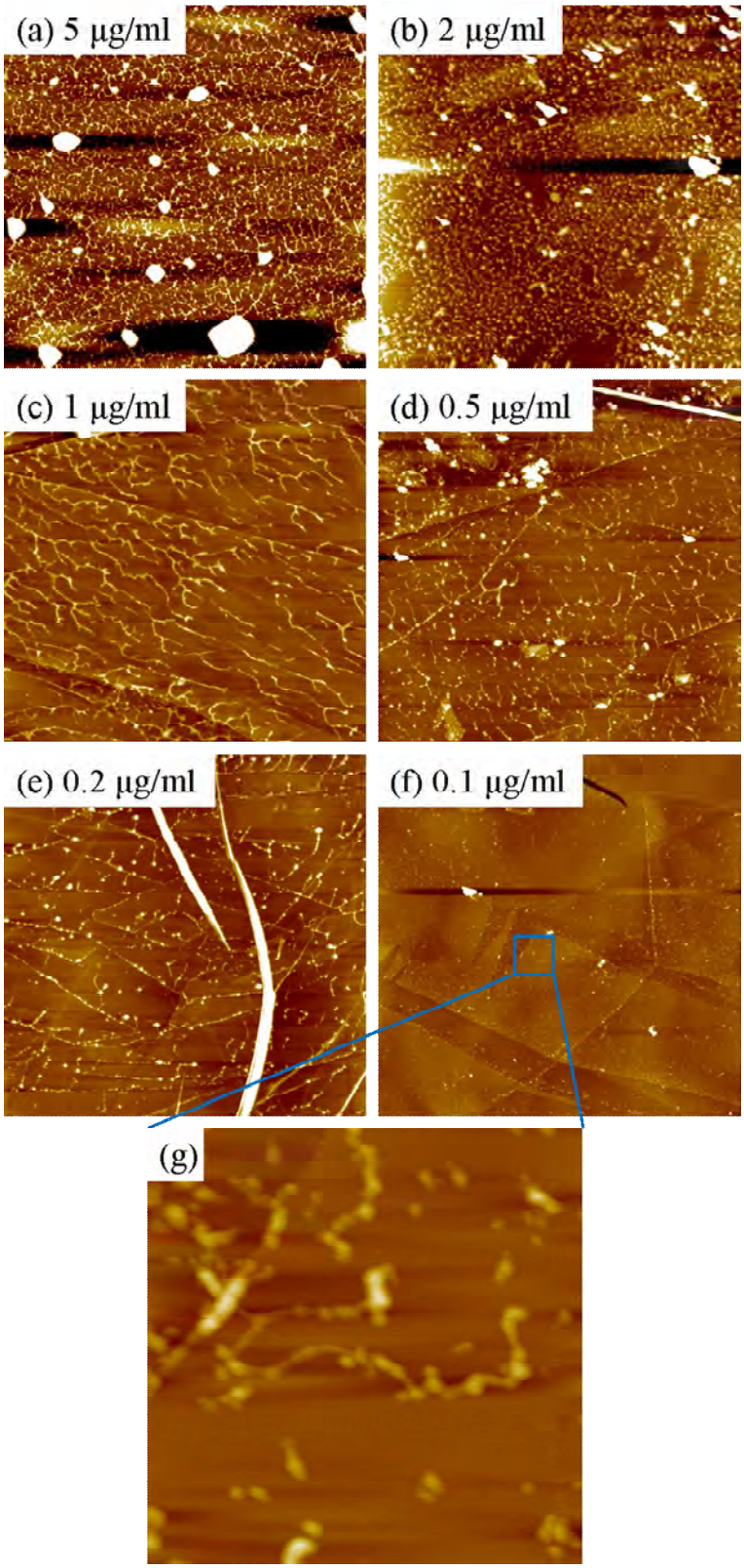

Figure 6.6 Tapping mode AFM images of the mucin sample with buffer dried on the bare HOPG surface without washing under different concentrations (10 µm × 10 µm, z scale 10 nm): (a) 5 µg/ml, (b) 2 µg/ml, (c) 1 µg/ml, (d) 0.5 µg/ml, (e) 0.2 µg/ml, (f) 0.1 µg/ml. (g) Magnified tapping mode AFM image of the centre part of (f) (1 µm × 1 µm, z scale 5 nm).

6.2.3 STM study of mucin manipulation on the bare HOPG surface

After the features found on the surface are confirmed to be mucin molecules, STM manipulation has been tried. As mentioned before, at higher mucin concentration, thicker linear features could be observed under STM. Following the discussion above, these thicker linear features were quite likely to be assemblies of several mucin molecules. Furthermore, both unstable and stable thicker linear features can be detected in the STM experiment in the dehydrated state. Some mechanical manipulations over these features were achieved during the experiments.

By counting the displacements along the linear features that happened during one image as shown in Figs. 6.7 (a) and (b), we can plot the relation between the interaction times versus the bias voltage under different tunnelling currents. Figs. 6.7 (c) and (d) show the relation between the bias voltage and the displacement count acquired under 40 pA and 400 pA, respectively. From the figures, we can clearly notice the trend that the displacement (which indicates the interactions between the tip and the molecule) during the scans reduced following the increase of the bias voltage in each case. Based on the relation between the bias voltage and the tip-surface gap, we know that under a certain tunnelling current, the small bias voltage means the small tip-surface gap, which implies more chances for the tip-molecule interactions. Thus these curves show that the displacements during the experiments together with the movement of the features afterwards were induced by the mechanical interaction between the STM tip and molecules.

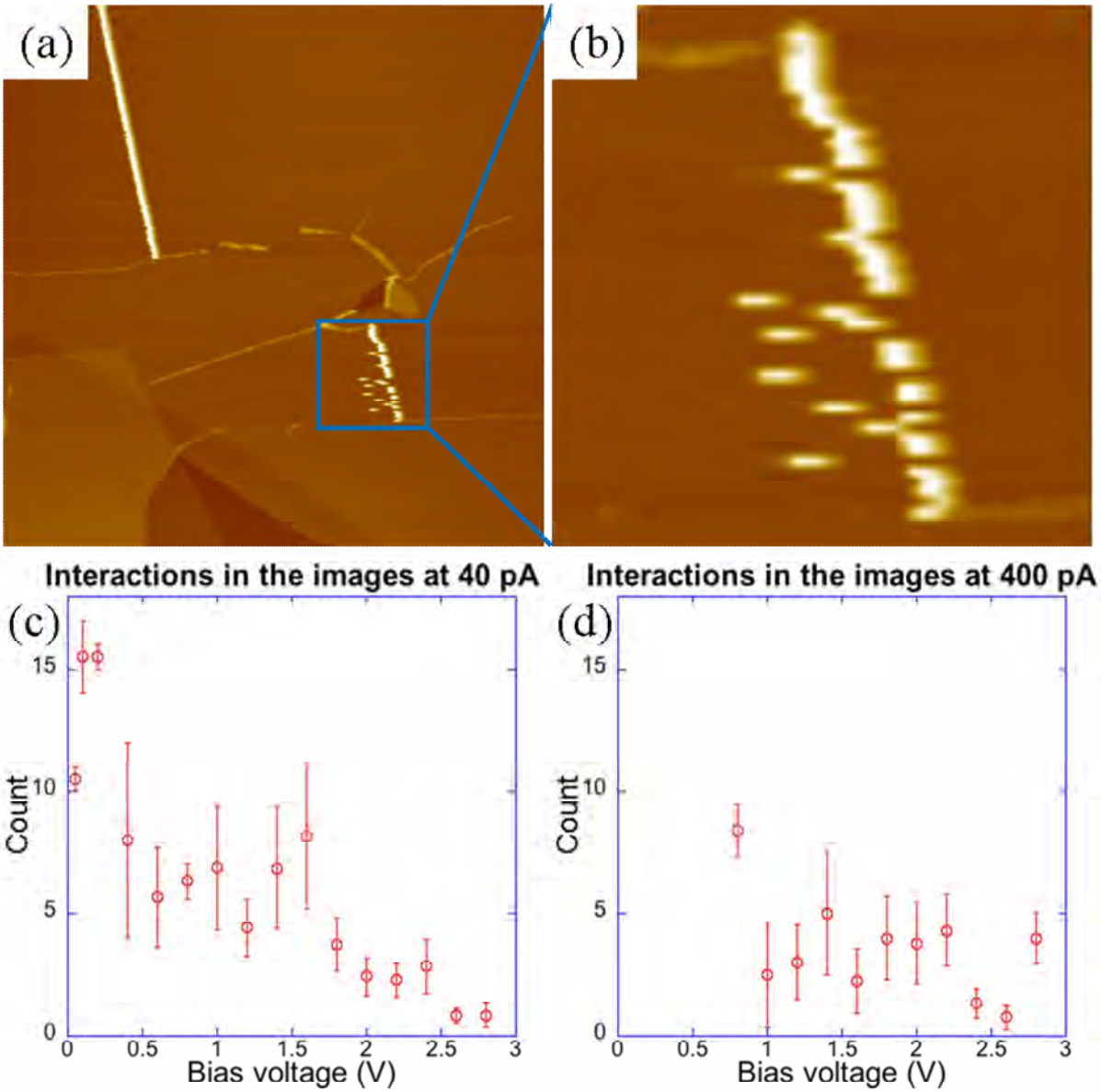

Figure 6.7 (a) A typical STM image acquired during the experiments (1 μm × 1 μm, z scale 10 nm). (b) Magnified STM image of (a) (200 nm × 200 nm, z scale 10 nm). (c) The averaged counts of the displacements happened during one scan versus the bias voltage under a tunnelling current of 40 pA. (d) The averaged counts of the displacements happened during one scan versus the bias voltage under a tunnelling current of 400 pA.

Among the unstable features in STM experiments on the bare HOPG surface in the dehydrated state, some interesting nice mucin structures could be noticed. In these cases as shown in Figs. 6.8 (a) to (d), one end of the thick segment of the mucin structure kept moving along the step edge, while the other end of the thin segment knotted to a broken piece of graphite kept extending. During this process, the thick segment reduced in length, while the

thin segment increased in length. To acquire quantitative information of this process, the volume and the length of the thin segment and the thick segment, the angle between the thin segment and the thick segment have been measured.

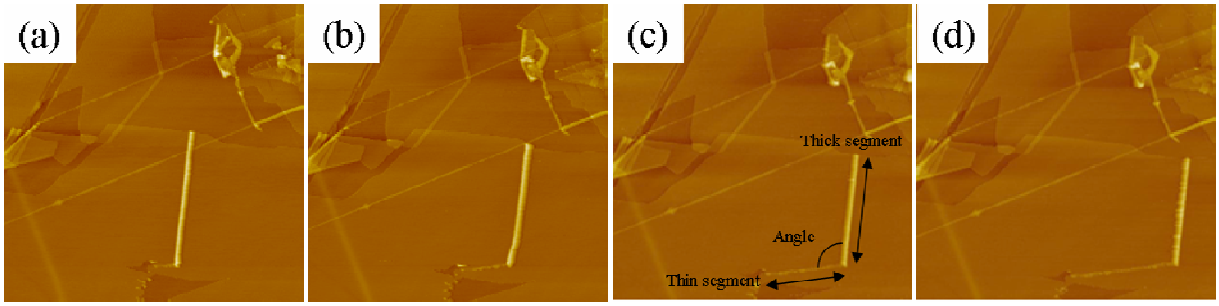

Figure 6.8 (a)-(d) Series of STM images that show a single mucin structure being dragged by the STM tip from left to right during the experiments (4 μg/ml, 750 nm × 750 nm, 800 mV, 200 pA).

Fig. 6.9 (a) gives the measurement of the volume of both segments. It shows that the volume of the thin segment increased during the process, while the thick one kept shrinking. Furthermore, the relation between the length of the thick segment and that of the thin segment is plotted in Fig. 6.9 (b). If we assume that the thick segment consisted of several thin segments, then it gives:

$$L_{Total} = L_{Thin} + n \times L_{Thick}, \tag{6.1}$$

where L_{Thin} stands for the length of the thin segment, L_{Thick} stands for the length of the thick segment and L_{Total} stands for the total length of the real molecule. From the equation of the fit curve of this figure,

$$n = 2.9 \pm 0.1 \tag{6.2}$$

suggests that the thick segment was made up of three thin segments.

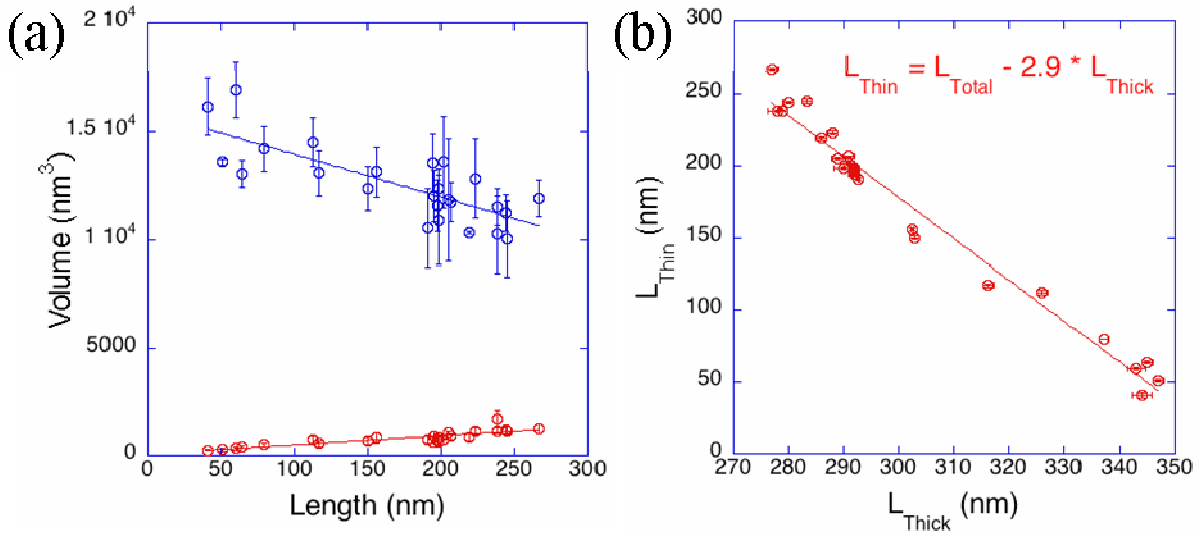

Figure 6.9 (a) The volume of the thin segment (red dots) and the volume of the thick segment (blue dots) versus the length of the thin segment. (b) The length of the thin segment (L_{Thin}) versus the length of the thick segment (L_{Thick}).

Finally, as shown in Fig. 6.10 (a), the angle between the thick segment and the thin segment remained roughly constant throughout the process, which was $105^\circ \pm 1^\circ$. Also, by measuring the length of the thin segment during the whole process, a step in the length increase of the thin segment can be found, which was ~45 nm, as shown in Fig. 6.10 (b). These two parametres should originate in the mucin molecule's structure.

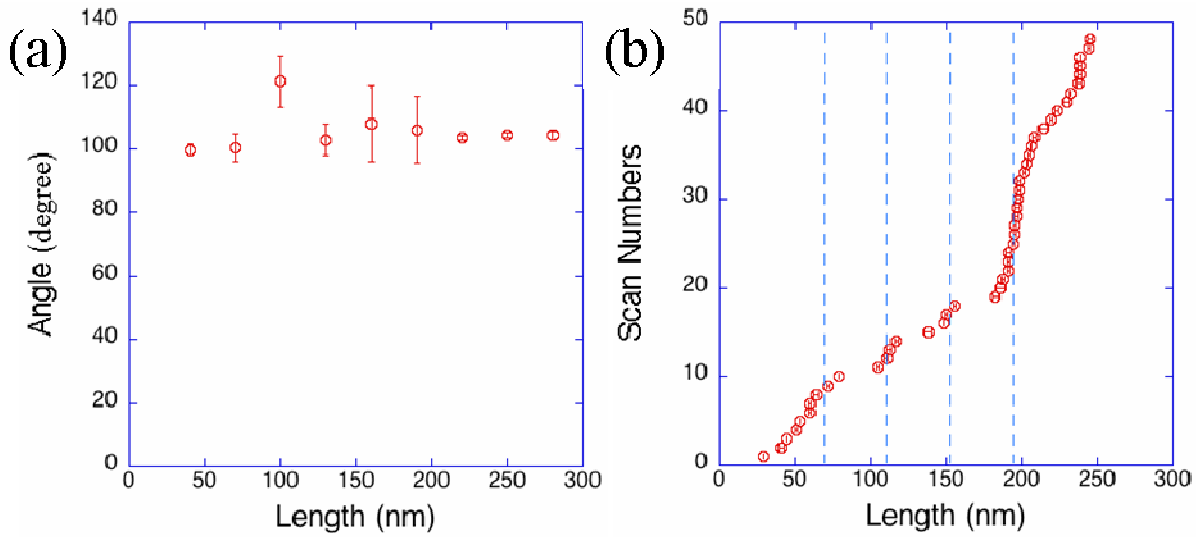

Figure 6.10 (a) The measured angle between the two segments versus the length of the thin segment. (b) Length distribution of the thin segment during the scanning.

6.2.4 Discussion

In the STM study of the mucin molecule on the bare HOPG surface in the dehydrated state, both unstable and stable linear features could be acquired, which were later confirmed to be the features from the mucin molecules in the experiments performed with tapping mode AFM. In some cases of the unstable structures on the bare HOPG surface in the dehydrated state, one molecule polymer which was folded together in the beginning kept releasing into the thin segment during the subsequent scans. A constant angle could be observed in this case together with a step in the length increase ~45 nm of the thin segment. As for this constant angle, it might be from the angle of the carbon-disulphide bond which is 104° [121]. As for the step in the length increase, the length of the individual PGM monomer and the exact length of each domain forming the PGM are still unknown. It has been stated that the length of the whole molecular chain might be ~50 nm, based on other measurements [115, 116]. Therefore this

~45 nm elongated fragment length might be from the mucin monomer. If both assumptions are true (the step in the length increase is the individual mucin monomer and the constant angle is from the angle of carbon-sulphur-sulphur linkage), then what happened in the STM dragging experiments was the mechanical manipulation induced by the STM tip. By scanning across the mucin polymer several times, the STM tip made the mucin polymer (which was partially folded into the thick segment) slide over the surface and released one part of mucin monomer each time from the folded part.

6.3 AFM study of mucin in the liquid state

6.3.1 AFM study of mucin adsorption on the bare HOPG surface

Although mechanical manipulation of the mucin molecule has been achieved in the dehydrated state with the STM, no observations of the potential S-S bond cleavage phenomenon were achieved in these experiments (not shown here). Thus, we took another route by using contact mode AFM in the liquid state. This is because the protein needs a natural environment to maintain its function and the dehydrated state may cause denaturing of the protein and change its properties.

Initially, contact mode AFM experiments in the liquid state with a normal tip were performed in order to try and achieve an ideal condition in which mucin molecules adsorbed on the bare HOPG were stable enough for subsequent manipulation experiments with a conductive AFM tip. Different conditions (including different forces, different concentrations, different

incubation times and different storage times) were tested.

Figs. 6.11 (a) and (b) are images selected from different force experiments, where a very small force (1.9 nN) was applied during the experiment. These two contact mode AFM images were taken in the same place under the same conditions, except for the scan angles. One was scanned horizontally and the other was scanned vertically. From these two images, the strong tip-molecule interactions could be inferred, since features were dragged horizontally or vertically accordingly. Further reducing the force down to 0.6 nN did not yield better and stable images, which indicates that the low mucin coverage condition is not suitable for practicing AFM imaging. Besides reducing the force during scanning, the other way to stabilize molecules on the surface is by using the molecule-molecule interaction [119]. Thus, experiments at different concentration were also attempted. Fig. 6.11 (c) shows one example under a higher concentration. However, this method did not provide stability either. Molecules in the centre square, where several scans were previously performed, were cleared away by the AFM tip and piled up at the edge of the square, revealing the HOPG surface underneath. This indicates that even high mucin concentration condition is not stable against AFM imaging. Another way to stabilize molecules on the surface is by using a longer incubation time, where molecules have longer time to stabilize onto the surface. Nevertheless, similar phenomena were observed for different incubation times and different storage times. All these indicate that mucin molecules adsorbed on the bare HOPG surface were not stable enough for contact mode AFM imaging and could be easily moved by the AFM tip. Contact AFM experiments done in the dehydrated state gave similar results.

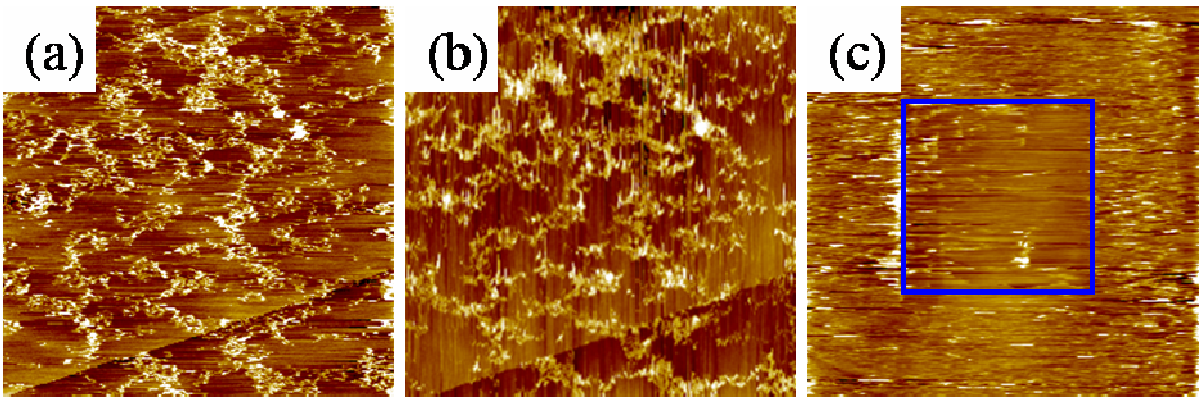

Figure 6.11 (a) and (b) Contact mode AFM image of 2 µg/ml mucin sample with buffer on the bare HOPG surface; (a) 4 µm × 4 µm, z scale 5 nm, 1.9 nN, scan angle 0°, (b) 4 µm × 4 µm, z scale 5 nm, 1.9 nN, scan angle 90°. (c) Contact mode AFM image of 20 µg/ml mucin sample with buffer on the bare HOPG surface, the central blue square outlined was the place where several scans had been carried out before; 10 µm × 10 µm, z scale 10 nm, 7.2 nN.

6.3.2 AFM study of mucin adsorption on the Au cluster decorated HOPG surface

As indicated in the above results, the bare HOPG surface was not suitable for contact mode AFM in the liquid state, so the bare HOPG surface needs to be adapted in order to enhance the molecule-surface interaction. From previous studies [119], the size-selected gold cluster-decorated HOPG surface is a candidate in this situation. In principle, it can provide the mucin molecule with stabilizing bonds to the support by forming S-Au bonds without providing too many bonding sites to break all disulphide bonds. Two types of size-selected Au_{55} cluster-decorated HOPG surface were prepared (one with 110 nm mean distance between the clusters and the other with 150 nm mean distance between the clusters).

Fig. 6.12 (a) shows the STM image of size-selected Au_{55} clusters on the HOPG surface with the mean distance between clusters of 110 nm, before the deposition of the mucin sample. Fig. 6.12 (b) shows the contact mode AFM image on the surface of (a), after the deposition of 1

μg/ml mucin sample. Fig. 6.12 (c) shows the contact mode AFM image of the same area as (b), after several scans under higher force. By the comparison between Figs. 6.12 (b) and (c), the mucin features on this surface was quite stable against contact mode AFM scanning, which was completely different from what was observed in the previous experiments with STM in the dehydrated state and contact mode AFM on the bare HOPG surface. In the presence of the cluster, many large globular features could be observed on the surface with a height up to ~11 nm and a diameter up to ~120 nm, which were quite stable even after repeated scans. However, no fibre-like features could be found on the surface. This probable arises from the excess mucin concentration of 1 μg/ml, where mucin molecules aggregated together to form these huge globular features. Moreover, by comparing Fig. 6.12 (a) and Fig. 6.12 (b), we found that the density of the huge globular features was much less than the density of gold clusters over the same area, which indicates the aggregation occurred across multiple clusters.

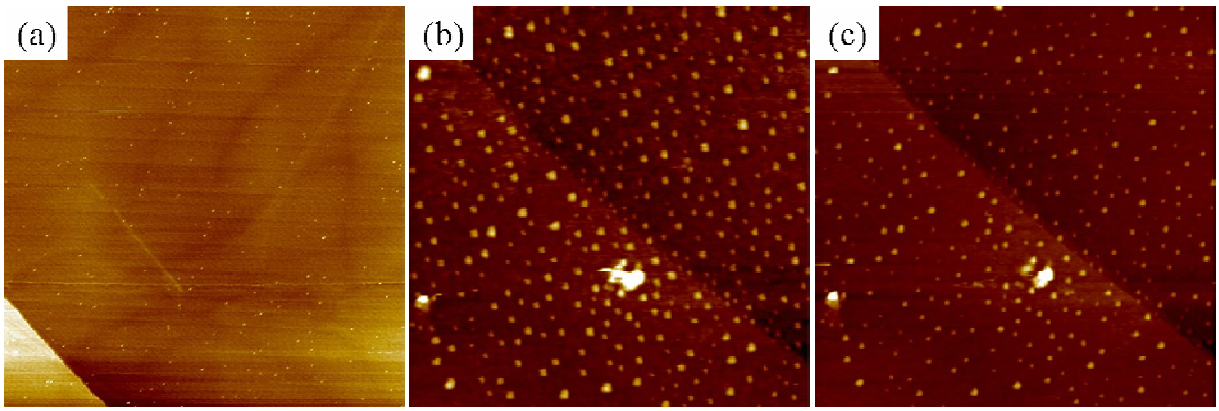

Figure 6.12 (a) STM image of the size-selected Au_{55} cluster-decorated HOPG surface with the mean distance 110 nm between the clusters (400 mV, 200 pA, 750 nm × 750 nm). (b) Contact mode AFM image of 1 μg/ml mucin sample with buffer on the surface of (a) (5 μm × 5 μm, z scale 20 nm, 4 nN). (c) Contact mode AFM image of (b) after several scans under higher force (5 μm × 5μm, z scale 20 nm, 8 nN).

Fig. 6.13 (a) shows the STM image of size-selected Au_{55} clusters on the HOPG surface with the mean distance between clusters of 150 nm, before the deposition of the mucin sample. By reducing the mucin concentration to 0.5 ng/ml, smaller globular features with a height up to ~7 nm and a diameter up to ~50 nm could be found on the surface with some fibre-like features between them, as shown in Fig. 6.13 (b). By comparing Fig. 6.13 (b) and Fig. 6.12 (b), the numbers of the globular features in Fig. 6.13 (b) were much more than that in Fig. 6.12 (b), which indicates that these smaller globular features should be the aggregation over single clusters instead of multiple clusters, due to the increased mean distance between the gold clusters together with the reduced mucin concentration. Figs. 6.12 (c) and (d) show high resolution images of the surface before and after repeated scans over the same fibre-like feature indicated by the blue ellipse. The height of this feature is ~1.6 nm, the mean length is ~300 nm and the width varies ~30 nm. Due to the fact that the AFM tip will normally enlarge the lateral dimension of features imaged [122, 123], and that the tip radius used in these experiments was ~10 nm, the real width of this fibre-like feature is probably just over ~20 nm. This indicates that the fibre-like feature were probably the single mucin polymer molecule attached across two or more clusters and successfully fixed on the surface.

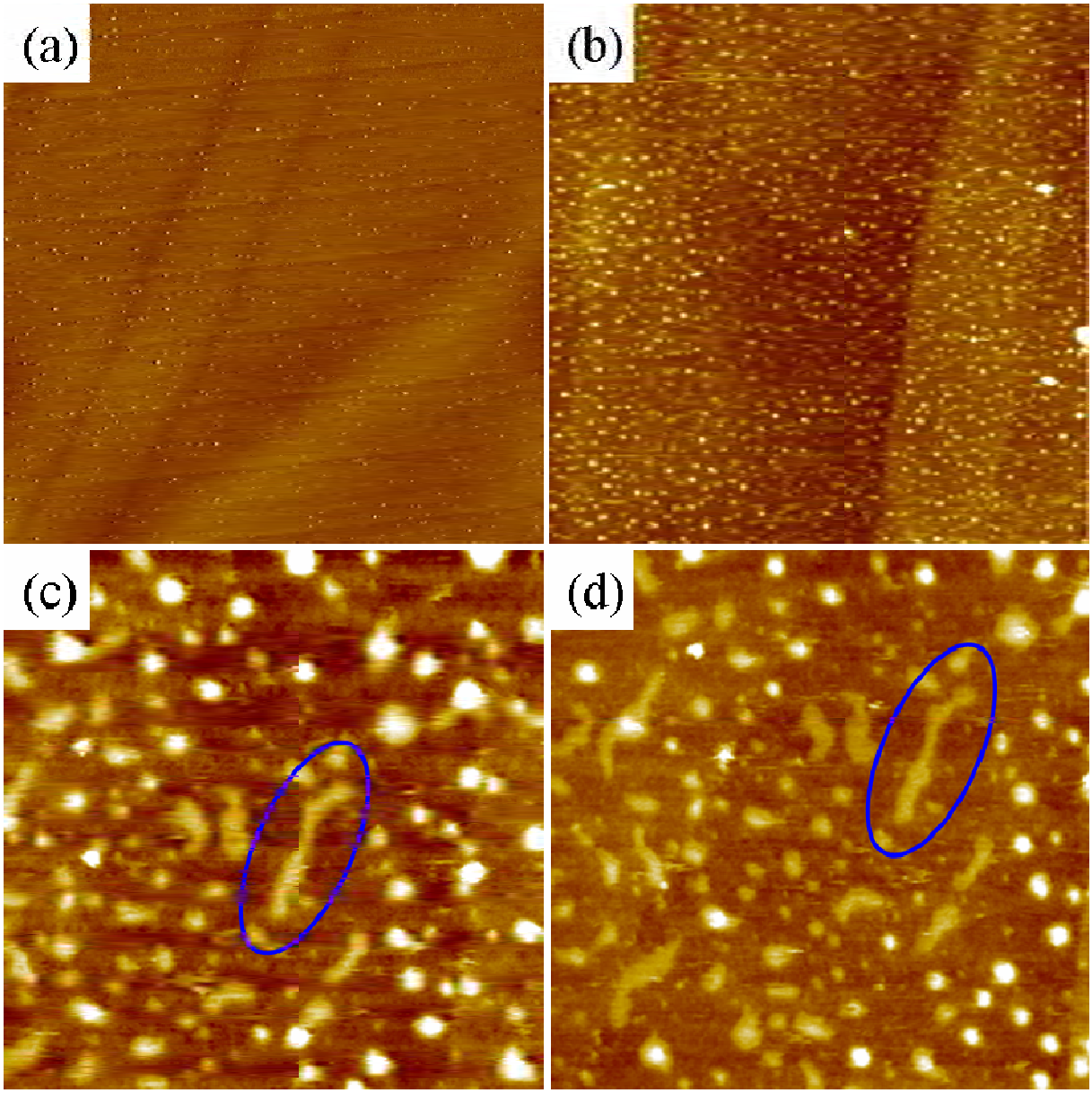

Figure 6.13 (a) STM image of the size-selected Au_{55} cluster-decorated HOPG surface with the mean distance 150 nm between the clusters (400 mV, 200 pA, 500 nm × 500 nm). (b) Contact mode AFM image of 0.5 ng/ml mucin sample with buffer on the surface of (a) (5 μm × 5 μm, z scale 10 nm, 0.7 nN). (c) High resolution contact mode AFM image of (b) (1 μm × 1 μm, z scale 5 nm, 0.5 nN) (d) Contact mode AFM image taken at the same place as (c) after 4 scans under 0.7 nN and 1.4 nN (1 μm × 1 μm, z scale 5 nm, 0.5 nN). The blue ellipses indicate the same fibre-like feature.

6.4 Conclusion

We found that in STM experiments in the dehydrated state and contact mode AFM experiments in both liquid and dehydrated states on the bare HOPG mucin molecules were not firmly bound to the surface and were easily swept away by the STM/AFM tip. However, the use of the size-selected Au_{55} cluster-decorated HOPG surface, whereby the gold-sulphur bonds can help to stabilize the molecule, enabled stable mucin features to be observed under repeated AFM imaging under the liquid state. At high mucin concentration, mucin molecules aggregated across multiple clusters, forming large, stable globular features on the surface, no fibre-like features could be observed. At low mucin concentration, small globular features were accompanied by fibre-like features on the surface. The fibre-like features were possibly single mucin polymers. The conclusion is that the gold-decorated HOPG surface is an ideal platform to stabilize the molecule and facilitate the future investigation of selective dissociation with a conductive AFM tip.

Chapter 7 Future plan

7.1 Summary

In this thesis, we presented an STM and STS investigation of the chlorobenzene molecule, together with an STM and STS investigation of the PCB molecule, and a combined STM and AFM investigation of the mucin molecule.

The investigation of the chlorobenzene molecule in the STS demonstrated the elimination of the rest atom state at -0.8 V, which provides the direct evidence of rest atom involvement in the bonding geometry of the chlorobenzene molecule on the Si(111)-7×7 surface. A chlorobenzene molecular state at -1.2 V was probed STS, which matches the chlorobenzene desorption threshold at negative bias voltage. No obvious difference was noted in the non-local desorption probability between the "uphill" and "downhill" process on the stepped surface, which may indicate that electrons transport through the bulk instead of through a channel lying just below the surface in the non-local desorption process. Two activation energies, 16.7 ± 4.8 meV and 162 ± 6 meV, in different temperature regions, may indicate different non-local desorption mechanisms. One may be facilitated by the surface phonon and the other by the vibration mode.

Atomic manipulations of the PCB molecule were achieved using STM, where three types of reactions could be triggered, including desorption, reconfiguration and seesaw. Through precise site injection of electrons into different part of the PCB molecule, the desorption

process was found to be favoured on the dark site injection below +2.5 V, while the reconfiguration process was found to be favoured on the bright site injection above +2.5 V. Two new generated states, between +1.0 V and +2.2 V on the dark site and starting at +2.5 V on the bright site, were found in the STS curve, matching quite well with reaction thresholds.

Molecular manipulations of the mucin molecule were achieved using STM on the bare HOPG surface, where a folded mucin polymer was thought to be unravelled one monomer a time by the STM tip. Attachment of stable mucin molecules to a gold-decorated HOPG surface was realized. Mucin molecules with two ends attached to two gold clusters, like a string, have been observed on this surface.

The work on the non-local chlorobenzene desorption in chapter 4 provides insight into understanding electron transport on the surface that will be helpful in fabrication of nanopattern and nano device in the future. The work of atomic manipulation of the PCB molecule in chapter 5 demonstrates a way to perform site- and energy-selective intramolecular manipulation. This will be helpful in understanding the reaction induced by the STM manipulation, and in developing better control of different reactions induced by STM manipulation over the same molecule. The work on the mucin molecule in chapter 6 has provided more information in determining the structure of this bio-molecule. The work has also shown an ideal platform (the gold decorated HOPG surface) for future bio-molecule manipulation experiments.

7.2 Future work

In relation to the results presented in chapter 4, there are still many aspects that remain unanswered. First, the suppression region appears near the injection site. We proposed that this may be due to the presence of an electric field beneath the tip, which hinders the molecule from desorption. A future experiment could be performed with electron injection at different bias voltage, in order to check how this suppression region changes. The hole injection could also be tested. Second, since we proposed that electrons may transport through the bulk to cause the non-local desorption, it would be interesting to investigate what may happen with hole injection. Also sub-surface electron transport could be further investigated using other surface, e.g., Ge/Si or Si/SiO_x, where electrons are confined to the surface layer and the non-local desorption of the chlorobenzene molecule could serve as a label. Third, more data points are needed to generate a more precise activation energy for the non-local desorption. Measurements at the temperature between 293 K and 230 K and between 77 K and 120 K could be performed. This may help to identify the origins of these two activation energies. Fourth, lower temperature experiments between 4 K and 77 K could be performed to check what effect this may have on the non-local desorption experiment.

For the results presented in chapter 5, key interest has been paid to two reaction outcomes: the desorption and the reconfiguration process. The seesaw process has not been systematically investigated here. The bi-stable states of the product molecule after the seesaw process might be interesting to investigate latter, since it might be able to act as a molecular switch. This switch can have “off” and “on” modes, corresponding to the status before and after the seesaw process. Also, when it is in the “on” mode, it has two bi-stable states which can be viewed as “1” and “0”. If these “1” and “0” states can be controlled, then the PCB molecule could serve as a basic unit in a nano device.

For the results presented in chapter 6, since we have already acquired such an ideal platform for molecular manipulation of bio-molecules, the investigation of the S-S bond dissociation through the electron injection could be carried out. This experiment could be first tried in the dry state, and then in the liquid state. If it is successful, it can further the atomic manipulation from the small inorganic and organic molecule up to the big bio-molecule.

Appendix

Published Papers

T. L. Pan, S. Sakulsermsuk, P. A. Sloan, and R. E. Palmer, Site- and Energy-Selective Intramolecular Manipulation of Polychlorinated Biphenyl (PCB) Molecules. *J. Am. Chem. Soc.*, **133**, 11834 (2011)

T. L. Pan, P. A. Sloan, and R. E. Palmer, Towards Manipulation of Single Proteins: Scanning Probe Microscopy in a Physiological Environment. Accepted in *G.I.T. Imaging & Microscopy*

Reference

1. Binning, G., Rohrer, H., Gerber, C. and Weibel, E., *Surface Studies by Scanning Tunneling Microscopy.* Phys. Rev. Lett. **49**, 57 (1982).
2. Eigler, D. M. and Schweizer, E. K., *Positioning single atoms with a scanning tunnelling microscope.* Nature **344**, 524 (1990).
3. Hosaka, S., Hosoki, S., Hasegawa, T., Koyanagi, H., Shintani, T. and Miyamoto, a. M., *Fabrication of nanostructures using scanning probe microscopes.* J. Vac. Sci. Technol. B **13**, 2813 (1995).
4. Komeda, T., Hasunuma, R., Mukaida, H. and Tokumoto, H., *Layer-by-layer atomic manipulation on Si(111)-7x7 surface: surface structures and staircase conductance variation with atom removal.* Surf. Sci. **386**, 149 (1997).
5. Huang, D. H. and Aono, M., *Scanning tunneling microscopy fabrication of an Si atom chain.* Surf. Sci. **386**, 166 (1997).
6. Mayne, A. J., Dujardin, G., Comtet, G. and Riedel, D., *Electronic Control of Single-Molecule Dynamics.* Chem. Rev. **106**, 4355 (2006).
7. Stroscio, J. A. and Eigler, D. M., *Atomic and Molecular Manipulation with the Scanning Tunneling Microscope.* Science **254**, 1319 (1991).
8. Binnig, G. and Rohrer, H., *Scanning Tunneling Microscopy.* Helv. Phys. Acta **55**, 726 (1982).
9. http://www.almaden.ibm.com/vis/stm/atomo.html.
10. Stroscio, J. A. and Kaiser, W. J., Scanning Tunnelling Microscopy (1993).
11. Wiesendanger, R. and Güntherodt, H.-J., Scanning Tunneling Microscopy III (1996).
12. Selloni, A., Carnevali, P., Tosatti, E. and Chen, C. D., *Voltage-dependent scanning-tunneling microscopy of a crystal surface: Graphite.* Phys. Rev. B **31**, 2602 (1985).
13. Tersoff, J. and Hamann, D. R., *Theory of the scanning tunneling microscope.* Phys. Rev. B **31**, 805 (1985).
14. Bonnell, D. A., Scanning Tunnelling Microscopy and Spectroscopy (1993).
15. Binnig, G., Quate, C. F. and Gerber, C., *Atomic Force Microscope.* Phys. Rev. Lett. **56**, 930 (1986).
16. http://www.nanoscience.com/education/AFM.html.
17. Stroscio, J. A., Feenstra, R. M. and Fein, A. P., *Electronic-Structure of the Si(111)2x1 Surface by Scanning-Tunneling Microscopy.* Phys. Rev. Lett. **57**, 2579 (1986).
18. Feenstra, R. M. and Martensson, P., *Fermi-Level Pinning at the Sb/Gaas(110) Surface Studied by Scanning Tunneling Spectroscopy.* Phys. Rev. Lett. **61**, 447 (1988).
19. Feenstra, R. M., Stroscio, J. A. and Fein, A. P., *Tunneling Spectroscopy of the Si(111)2x1 Surface.* Surf. Sci. **181**, 295 (1987).
20. http://www-03.ibm.com/ibm/history/exhibits/vintage/vintage_4506VV1003.html.
21. Whitman, L. J., Stroscio, J. A., Dragoset, R. A. and Celotta, R. J., *Manipulation of Adsorbed Atoms and Creation of New Structures on Room-Temperature Surfaces with a Scanning Tunneling Microscope.* Science **251**, 1206 (1991).
22. Stipe, B. C., Rezaei, M. A., Ho, W., Gao, S., Persson, M. and Lundqvist, B. I., *Single-Molecule Dissociation by Tunneling Electrons.* Phys. Rev. Lett. **78**, 4410 (1997).
23. Gao, S. W., *Quantum kinetic theory of vibrational heating and bond breaking by hot electrons.* Phys. Rev. B **55**, 1876 (1997).
24. Gao, S. W., Busch, D. G. and Ho, W., *Femtosecond dynamics of electron-vibrational heating and desorption.* Surf. Sci. **344**, L1252 (1995).

25. Salam, G. P., Persson, M. and Palmer, R. E., *Possibility of Coherent Multiple Excitation in Atom-Transfer with a Scanning Tunneling Microscope.* Phys. Rev. B **49**, 10655 (1994).
26. Walkup, R. E., Newns, D. M. and Avouris, P., *Role of Multiple Inelastic Transitions in Atom-Transfer with the Scanning Tunneling Microscope.* Phys. Rev. B **48**, 1858 (1993).
27. Gao, S. W., Persson, M. and Lundqvist, B. I., *Theory of atom transfer with a scanning tunneling microscope.* Phys. Rev. B **55**, 4825 (1997).
28. Bartels, L., Meyer, G. and Rieder, K. H., *Basic Steps of Lateral Manipulation of Single Atoms and Diatomic Clusters with a Scanning Tunneling Microscope Tip.* Phys. Rev. Lett. **79**, 697 (1997).
29. Hla, S. W., Braun, K. F. and Rieder, K. H., *Single-atom manipulation mechanisms during a quantum corral construction.* Phys. Rev. B **67**, 4 (2003).
30. Keeling, D. L., Humphry, M. J., Fawcett, R. H. J., Beton, P. H., Hobbs, C. and Kantorovich, L., *Bond breaking coupled with translation in rolling of covalently bound molecules.* Phys. Rev. Lett. **94**, 4 (2005).
31. Grill, L., Rieder, K. H., Moresco, F., Rapenne, G., Stojkovic, S., Bouju, X. and Joachim, C., *Rolling a single molecular wheel at the atomic scale.* Nat. Nanotechnol. **2**, 95 (2007).
32. Yu, M., Xu, W., Benjalal, Y., Barattin, R., Laegsgaard, E., Stensgaard, I., Hliwa, M., Bouju, X., Gourdon, A., Joachim, C., Linderoth, T. R., and Besenbacher, F., *STM Manipulation of Molecular Moulds on Metal Surfaces.* Nano Res. **2**, 254 (2009).
33. Katano, S., Kim, Y., Kagata, Y. and Kawai, M., *Single-Molecule Vibrational Spectroscopy and Inelastic-Tunneling-Electron-Induced Diffusion of Formate Adsorbed on Ni(110).* J. Phys. Chem. C **114**, 3003 (2010).
34. Stipe, B. C., Rezaei, M. A. and Ho, W., *Coupling of vibrational excitation to the rotational motion of a single adsorbed molecule.* Phys. Rev. Lett. **81**, 1263 (1998).
35. Katano, S., Kim, Y., Kagata, Y. and Kawai, M., *Vibration-Assisted Rotation and Deprotonation of a Single Formic Acid Molecule Adsorbed on Ni(110) Studied by Scanning Tunneling Microscopy.* J. Phys. Chem. C **113**, 19277 (2009).
36. Lastapis, M., Martin, M., Riedel, D., Hellner, L., Comtet, G. and Dujardin, G., *Picometer-scale electronic control of molecular dynamics inside a single molecule.* Science **308**, 1000 (2005).
37. Martin, M., Lastapis, M., Riedel, D., Dujardin, G., Mamatkulov, M., Stauffer, L. and Sonnet, P., *Mastering the Molecular Dynamics of a Bistable Molecule by Single Atom Manipulation.* Phys. Rev. Lett. **97**, 216103 (2006).
38. Mayne, A. J., Lastapis, M., Baffou, G., Soukiassian, L., Comtet, G., Hellner, L. and Dujardin, G., *Chemisorbed bistable molecule: Biphenyl on Si(100)-2×1.* Phys. Rev. B **69**, 045409 (2004).
39. Riedel, D., Bocquet, M.-L., Lesnard, H., Lastapis, M., Lorente, N., Sonnet, P. and Dujardin, G., *Selective Scanning Tunnelling Microscope Electron-Induced Reactions of Single Biphenyl Molecules on a Si(100) Surface.* J. Am. Chem. Soc. **131**, 7344 (2009).
40. Sloan, P. A., Sakulsermsuk, S. and Palmer, R. E., *Nonlocal Desorption of Chlorobenzene Molecules from the Si(111)-(7x7) Surface by Charge Injection from the Tip of a Scanning Tunneling Microscope: Remote Control of Atomic Manipulation.* Phys. Rev. Lett. **105**, 048301 (2010).
41. Sloan, P. A., Hedouin, M. F. G., Palmer, R. E. and Persson, M., *Mechanisms of Molecular Manipulation with the Scanning Tunneling Microscope at Room Temperature: Chlorobenzene/Si(111)-(7x7).* Phys. Rev. Lett. **91**, 118301 (2003).
42. Sloan, P. A. and Palmer, R. E., *Manipulation of polyatomic molecules with the scanning tunnelling microscope at room temperature: chlorobenzene adsorption and desorption from Si(111)-(7x7).* J. Phys.: Condens. Matter **18**, S1873 (2006).

43. Bellec, A., Riedel, D., Dujardin, G., Boudrioua, O., Chaput, L., Stauffer, L. and Sonnet, P., *Nonlocal Activation of a Bistable Atom through a Surface State Charge-Transfer Process on Si(100)-(2x1):H.* Phys. Rev. Lett. **105**, 048302 (2010).
44. Maksymovych, P., Dougherty, D. B., Zhu, X. Y. and Yates, J. T., Jr., *Nonlocal Dissociative Chemistry of Adsorbed Molecules Induced by Localized Electron Injection into Metal Surfaces.* Phys. Rev. Lett. **99**, 016101 (2007).
45. Maksymovych, P., Sorescu, D. C., Jordan, K. D. and Yates, J. T., *Collective Reactivity of Molecular Chains Self-Assembled on a Surface.* Science **322**, 1664 (2008).
46. Nouchi, R., Masunari, K., Ohta, T., Kubozono, Y. and Iwasa, Y., *Ring of C_{60} Polymers Formed by Electron or Hole Injection from a Scanning Tunneling Microscope Tip.* Phys. Rev. Lett. **97**, 196101 (2006).
47. Nakamura, Y., Mera, Y. and Maeda, K., *Diffusion of chlorine atoms on Si(111)-(7×7) surface enhanced by electron injection from scanning tunneling microscope tips.* Surf. Sci. **487**, 127 (2001).
48. Bartels, L., Meyer, G. and Rieder, K. H., *Controlled vertical manipulation of single CO molecules with the scanning tunneling microscope: A route to chemical contrast.* Appl. Phys. Lett. **71**, 213 (1997).
49. Bartels, L., Meyer, G., Rieder, K. H., Velic, D., Knoesel, E., Hotzel, A., Wolf, M. and Ertl, G., *Dynamics of electron-induced manipulation of individual CO molecules on Cu(III).* Phys. Rev. Lett. **80**, 2004 (1998).
50. Dujardin, G., Mayne, A., Robert, O., Rose, F., Joachim, C. and Tang, H., *Vertical manipulation of individual atoms by a direct STM tip-surface contact on Ge(111).* Phys. Rev. Lett. **80**, 3085 (1998).
51. Rezaei, M. A., Stipe, B. C. and Ho, W., *Atomically resolved adsorption and scanning tunneling microscope induced desorption on a semiconductor: NO on Si(111)-(7 x 7).* J. Chem. Phys. **110**, 4891 (1999).
52. Leoni, T., Guillermet, O., Walch, H., Langlais, V., Scheuermann, A., Bonvoisin, J. and Gauthier, S., *Controlling the Charge State of a Single Redox Molecular Switch.* Phys. Rev. Lett. **106** (2011).
53. Henzl, J., Bredow, T. and Morgenstern, K., *Irreversible isomerization of the azobenzene derivate Methyl Orange on Au(111).* Chem. Phys. Lett. **435**, 278 (2007).
54. Safiei, A., Henzl, J. and Morgenstern, K., *Isomerization of an Azobenzene Derivative on a Thin Insulating Layer by Inelastically Tunneling Electrons.* Phys. Rev. Lett. **104**, 216102 (2010).
55. Henzl, J., Mehlhorn, M. and Morgenstern, K., *Amino-nitro-azobenzene dimers as a prototype for a molecular-level machine.* Nanotechnology **18**, 495502 (2007).
56. Henzl, J., Bredow, T. and Morgenstern, K., *Irreversible isomerization of the azobenzene derivate Methyl Orange on Au(111).* Chem. Phys. Lett. **435**, 278 (2007).
57. Alemani, M., Peters, M. V., Hecht, S., Rieder, K.-H., Moresco, F. and Grill, L., *Electric Field-Induced Isomerization of Azobenzene by STM.* J. Am. Chem. Soc. **128**, 14446 (2006).
58. Henzl, J. and Morgenstern, K., *An electron induced two-dimensional switch made of azobenzene derivatives anchored in supramolecular assemblies.* Phys. Chem. Chem. Phys. **12**, 6035 (2010).
59. Henzl, J., Mehlhorn, M., Gawronski, H., Rieder, K. H. and Morgenstern, K., *Reversible cis-trans isomerization of a single azobenzene molecule.* Angew. Chem. Int. Ed. **45**, 603 (2006).
60. Morgenstern, K., *Isomerization Reactions on Single Adsorbed Molecules.* Acc. Chem. Res. **42**, 213 (2009).
61. Sloan, P. A. and Palmer, R. E., *Two-electron dissociation of single molecules by atomic manipulation at room temperature.* Nature **434**, 367 (2005).
62. Sakulsermsuk, S., Sloan, P. A. and Palmer, R. E., *A New Mechanism of Atomic Manipulation: Bond-Selective Molecular Dissociation via Thermally Activated Electron Attachment.* Acs Nano **4**, 7344

(2010).

63. Baadji, N., Kuck, S., Brede, J., Hoffmann, G., Wiesendanger, R. and Sanvito, S., *Controlled sequential dehydrogenation of single molecules by scanning tunneling microscopy.* Phys. Rev. B **82**, 115447 (2010).
64. Ho, W., *Control and Characterization of a Multistep Unimolecular Reaction.* Phys. Rev. Lett. **84**, 1530 (2000).
65. Maksymovych, P., Sorescu, D. C. and Yates, J. T., *Methanethiolate adsorption site on Au(111): A combined STM/DFT study at the single-molecule level.* J. Phys. Chem. B **110**, 21161 (2006).
66. Parschau, M., Rieder, K. H., Hug, H. J. and Ernst, K. H., *Single-Molecule Chemistry and Analysis: Mode-Specific Dehydrogenation of Adsorbed Propene by Inelastic Electron Tunneling.* J. Am. Chem. Soc. **133**, 5689 (2011).
67. Dujardin, G., Walkup, R. E. and Avouris, P. H., *Dissociation of Individual Molecules with Electrons from the Tip of a Scanning Tunneling Microscope.* Science **255**, 1232 (1992).
68. Rezaei, M. A., Stipe, B. C. and Ho, W., *Imaging the atomically resolved dissociation of D_2S on Si(100) from 80 to 300 K.* J. Chem. Phys. **110**, 3548 (1999).
69. Hla, S. W., Bartels, L., Meyer, G. and Rieder, K. H., *Inducing all steps of a chemical reaction with the scanning tunneling microscope tip: Towards single molecule engineering.* Phys. Rev. Lett. **85**, 2777 (2000).
70. Repp, J., Meyer, G., Paavilainen, S., Olsson, F. E. and Persson, M., *Imaging Bond Formation Between a Gold Atom and Pentacene on an Insulating Surface.* Science **312**, 1196 (2006).
71. Lee, H. J. and Ho, W., *Single-Bond Formation and Characterization with a Scanning Tunneling Microscope.* Science **286**, 1719 (1999).
72. Cheng, Z., Chu, E. S., Sun, D., Kim, D., Zhu, Y., Luo, M., Pawin, G., Wong, K. L., Kwon, K.-Y., Carp, R., Marsella, M., and Bartels, L., *Tunability in Polyatomic Molecule Diffusion through Tunneling versus Pacing.* J. Am. Chem. Soc. **132**, 13578 (2010).
73. Crommie, M. F., Lutz, C. P. and Eigler, D. M., *Confinement of Electrons to Quantum Corrals on a Metal-Surface.* Science **262**, 218 (1993).
74. Manoharan, H. C., Lutz, C. P. and Eigler, D. M., *Quantum mirages formed by coherent projection of electronic structure.* Nature **403**, 512 (2000).
75. Tanaka, H. and Kawai, T., *Partial sequencing of a single DNA molecule with a scanning tunnelling microscope.* Nat. Nanotechnol. **4**, 518 (2009).
76. Oura, K., Lifshits, V. G., Saranin, A. A., Zotov, A. V. and Katayama, M., Surf. Sci. (2003).
77. *Tip etching kit user manual.* Omicron intruments for surface science (1998).
78. Lucier, A. S., Mortensen, H., Sun, Y. and Grutter, P., *Determination of the atomic structure of scanning probe microscopy tungsten tips by field ion microscopy.* Phys. Rev. B **72** (2005).
79. Dr. Sumet Sakulsermsuk's thesis.
80. Lidgi-Guigui, N., Leung, C. and Palmer, R. E., *Weak precursor state binding of protein molecules to size-selected gold nanoclusters on surfaces.* Surf. Sci. **602**, 1006 (2008).
81. Mårtensson, P. and Feenstra, R. M., *Geometric and electronic structure of antimony on the GaAs(110) surface studied by scanning tunneling microscopy.* Phys. Rev. B **39**, 7744 (1989).
82. Palmer, R. E., Sloan, P. A. and Xirouchaki, C., *Decoration of surfaces with size-selected clusters and molecular manipulation at room temperature: precision and uncertainty in organising atoms.* Phil. Trans. R. Soc. A **32**, 1195 (2004).
83. Sloan, P. A. and Palmer, R. E., *Tip-State Control of Rates and Branching Ratios in Atomic Manipulation.* Nano Lett. **5**, 835 (2005).

84. Sloan, P. A. and Palmer, R. E., *Manipulation of polyatomic molecules with the scanning tunnelling microscope at room temperature: chlorobenzene adsorption and desorption from Si(111)-(7x7).* J. Phys-Condens. Mat., 18, No. 33, S1873 - S1885 (2006).
85. Sakulsermsuk, S., Sloan, P. A., Theis, W. and Palmer, R. E., *Calibrating thermal and scanning tunnelling microscope induced desorption and diffusion for the chemisorbed chlorobenzene/Si(111)-7×7 system.* J. Phys.: Condens. Matter **22**, 084002 (2010).
86. Chen, X. H., Kong, Q., Polanyi, J. C., Rogers, D. and So, S., *The adsorption of C6H5Cl on Si(111)7×7 studied by STM.* Surf. Sci. **340**, 224 (1995).
87. Lu, X., Polanyi, J. C. and Yang, J., *A Reversible Molecular Switch Based on Pattern-Change in Chlorobenzene and Toluene on a Si(111)-(7 × 7) Surface.* Nano Lett. **6**, 809 (2006).
88. Lu, P. H., Polanyi, J. C. and Rogers, D., *Electron-induced "localized atomic reaction" (LAR): Chlorobenzene adsorbed on Si(111) 7 x 7.* J. Chem. Phys. **111**, 9905 (1999).
89. Cao, Y., Deng, J. F. and Xu, G. Q., *Stereo-selective binding of chlorobenzene on Si(111)-7x7.* J. Chem. Phys. **112**, 4759 (2000).
90. Takayanagi, K., Tanishiro, Y., Takahashi, S. and Takahashi, M., *Structure analysis of Si(111)-7 × 7 reconstructed surface by transmission electron diffraction.* Surf. Sci. **164**, 367 (1985).
91. Lin, J. L., Petrovykh, D. Y., Viernow, J., Men, F. K., Seo, D. J. and Himpsel, F. J., *Formation of regular step arrays on Si(111)7x7.* J. Appl. Phys. **84**, 255 (1998).
92. Chaika, A. N. and Myagkov, A. N., *Seeing the atomic orbitals in STM images of a Si(111)-(7x7) surface.* J. Phys: Conf. Ser. **100**, 012020 (2008).
93. Cao, Y., Wei, X. M., Chin, W. S., Lai, Y. H., Deng, J. F., Bernasek, S. L. and Xu, G. Q., *Formation of Di-ó Bond in Benzene Chemisorption on Si(111)-7x7.* J. Phys. Chem. B **103**, 5698 (1999).
94. Wolkow, R. and Avouris, P., *Atom-resolved surface chemistry using scanning tunneling microscopy.* Phys. Rev. Lett. **60**, 1049 (1988).
95. Hamers, R. J., Tromp, R. M. and Demuth, J. E., *Surface Electronic Structure of Si (111)-(7x7) Resolved in Real Space.* Phys. Rev. Lett. **56**, 1972 (1986).
96. Mysliveček, J., Stróżecka, A., Steffl, J., Sobotík, P., Ošt'ádal, I. and Voigtländer, B., *Structure of the adatom electron band of the Si(111)-7x7 surface.* Phys. Rev. B **73**, 161302 (2006).
97. Hamers, R. J., Tromp, R. M. and Demuth, J. E., *Electronic and geometric structure of Si(111)-(7 x7) and Si(001) surfaces.* Surf. Sci. **181**, 346 (1987).
98. Palevski, A., Heiblum, M., Umbach, C. P., Knoedler, C. M., Broers, A. N. and Koch, R. H., *Lateral tunneling, ballistic transport, and spectroscopy in a two-dimensional electron gas.* Phys. Rev. Lett. **62**, 1776 (1989).
99. Kim, J., Yeh, M.-L., Khan, F. S. and Wilkins, J. W., *Surface phonons of the Si(111)-7x7 reconstructed surface.* Phys. Rev. B **52**, 14709 (1995).
100. Miao, X., Chu, S., Xu, X. and Jin, X., *Structure elucidation of polychlorinated biphenyls by X-ray analysis.* Chin. Sci. Bull. **42**, 1803 (1997).
101. Needham, L. L., *Historical perspective on Yu-Cheng incident.* Organohalogen Compd. **14**, 231 (1993).
102. McFarland, V. A. and Clarke, J. U., *Environmental occurrence, abundance, and potential toxicity of polychlorinated biphenyl congeners: considerations for a congener-specific analysis.* Environ Health Perspect. **81**, 225 (1989).
103. Palmer, R. E., Sloan, P. A. and Xirouchaki, C., *Decoration of Surfaces with Size-Selected Clusters and Molecular Manipulation at Room Temperature: Precision and Uncertainty in Organizing Atoms.* Philosophical Transactions: Mathematical, Physical and Engineering Sciences **362**, 1195 (2004).
104. SIGMA-ALDRICH, Material Safety Data Sheet **1907** (2006).

105. Brayshaw, D. J., Berry, M. and McMaster, T. J., *Reducing a polymer to its subunits as an aid to molecular mapping.* Nanotechnology **15**, 1391 (2004).

106. Bansil, R., Stanley, E. and Lamont, J. T., *Mucin Biophysics.* Annu. Rev. Physiol. **57**, 635 (1995).

107. Cao, X. X., Bansil, R., Bhaskar, K. R., Turner, B. S., LaMont, J. T., Niu, N. and Afdhal, N. H., *pH-dependent conformational change of gastric mucin leads to sol-gel transition.* Biophys. J . **76**, 1250 (1999).

108. Hong, Z. N., Chasan, B., Bansil, R., Turner, B. S., Bhaskar, K. R. and Afdhal, N. H., *Atomic force microscopy reveals aggregation of gastric mucin at low pH.* Biomacromolecules. **6**, 3458 (2005).

109. Dekker, J., Rossen, J. W. A., Buller, H. A. and Einerhand, A. W. C., *The MUC family: an obituary.* Trends Biochem. Sci **27**, 126 (2002).

110. McMaster, T. J., Berry, M., Corfield, A. P. and Miles, M. J., *Atomic force microscopy of the submolecular architecture of hydrated ocular mucins.* Biophys. J . **77**, 533 (1999).

111. Round, A. N., Berry, M., McMaster, T. J., Corfield, A. P. and Miles, M. J., *Glycopolymer charge density determines conformation in human ocular mucin gene products: an atomic force microscope study.* J. Struct. Biol. **145**, 246 (2004).

112. Brayshaw, D. J., Berry, M. and McMaster, T. J., *Optimisation of sample preparation methods for air imaging of ocular mucins by AFM.* Ultramicroscopy. **97**, 289 (2003).

113. Deacon, M. P., McGurk, S., Roberts, C. J., Williams, P. M., Tendler, S. J. B., Davies, M. C., Davis, S. S. and Harding, S. E., *Atomic force microscopy of gastric mucin and chitosan mucoadhesive systems.* Biochem. J **348**, 557 (2000).

114. Sheehan, J. K., Oates, K. and Carlstedt, I., *Electron-Microscopy of Cervical, Gastric and Bronchial Mucus Glycoproteins.* Biochem. J **239**, 147 (1986).

115. Di Cola, E., Yakubov, G. E. and Waigh, T. A., *Double-Globular Structure of Porcine Stomach Mucin: A Small-Angle X-ray Scattering Study.* Biomacromolecules. **9**, 3216 (2008).

116. Yakubov, G. E., Papagiannopoulos, A., Rat, E., Easton, R. L. and Waigh, T. A., *Molecular structure and rheological properties of short-side-chain heavily glycosylated porcine stomach mucin.* Biomacromolecules. **8**, 3467 (2007).

117. Bansil, R. and Turner, B. S., *Mucin structure, aggregation, physiological functions and biomedical applications.* Curr. Opin. Colloid. Interf. Sci. **11**, 164 (2006).

118. Leung, C., Xirouchaki, C., Berovic, N. and Palmer, R. E., *Immobilization of Protein Molecules by Size-Selected Metal Clusters on Surfaces.* Adv. Mater. **16**, 223 (2004).

119. Palmer, R. E. and Leung, C., *Immobilisation of proteins by atomic clusters on surfaces.* Trends Biotechnol. **25**, 48 (2007).

120. Palmer, R. E., Pratontep, S. and Boyen, H. G., *Nanostructured surfaces from size-selected clusters.* Nat. Mater. **2**, 443 (2003).

121. Creighton, T. E., *Disulphide bonds and protein stability.* BioEssays **8**, 57 (1988).

122. Xu, S. H., Bevis, B. and Arnsdorf, M. F., *The assembly of amyloidogenic yeast Sup35 as assessed by scanning (atomic) force microscopy: An analogy to linear colloidal aggregation?* Biophys. J . **81**, 446 (2001).

123. Xu, S. and Arnsdorf, M. F., *Calibration of the scanning (atomic) force microscope with gold particles.* J Microsc. **173**, 199 (1994).